

Department of Physics

Spontaneous Fibril Formation in Eumelanin Synthesised from 3,4-
dihydroxyphenylalanine

Ross McQueenie

PhD Thesis

2011

Copyright

The copyright of this thesis belongs to the author under the terms of the United Kingdom Copyrights Act as qualified by the University of Strathclyde Regulation 3.51. Due acknowledgement must always be made of the use of any material contained in, or derived from this thesis.

Dedicated to Mum, Dad and Joanne for all of your support

Conference Contributions

- R. McQueenie, J. Karolin and D.J.S. Birch, Fibril Formation in Synthetic Melanin as Examined Via Microscopy and Fluorescence. Oral presentation: PiMOP Conference, Prague, Czech Republic. March 2010.
- R. McQueenie, J. Karolin and D.J.S. Birch, Spontaneous formation of fibrils in melanin synthesised from 3,4-dihydroxyphenylalanine. Oral presentation: iUPAC Chemistry Conference, Glasgow, Scotland. August 2009.
- R. McQueenie, J. Karolin and D.J.S. Birch, Spontaneous formation of fibrils in melanin synthesised from 3,4-dihydroxyphenylalanine. Poster presentation: iUPAC Chemistry Conference, Glasgow, Scotland. August 2009.
- R. McQueenie, J. Karolin and D.J.S. Birch, Fluorescence Response of DOPA, Studies of a Melanin Precursor. Poster presentation: Scottish Biophotonics Conference, St Andrews, Scotland. May 2008.

Acknowledgements

I would like to thank firstly both of my supervisors, Professor David Birch and Dr Jan Karolin for your support, patience, knowledge and guidance.

Also, I thank the support and friendship of all in the physics department at Strathclyde, in particular my co-workers and technicians, not only for your interest and enthusiasm, but also your ideas and input.

To Joanne: this thesis really wouldn't have been possible without your words of intelligence, knowledge and support during writing, with more than a few jokes thrown in to keep me smiling. The years of doing my PhD were made far more enjoyable with your company.

Thank you to the Engineering and Physical Sciences Research Council (EPSRC) for allowing me the opportunity of my research studentship.

Lastly, and most importantly, I would like to thank all of my family and friends, without whom life would be far less enjoyable.

Abstract

This thesis concerns synthetic melanin formation using 3,4-dihydroxyphenylalanine (DOPA), with respect to its possible fibril formation.

This study aims to bridge the gap between the understanding of L-DOPA as a precursor molecule and its formation into melanin. Thus, an overview of L-DOPA is presented in three distinct stages: its fluorescence properties as a precursor, the formation of melanin from L-DOPA, and the dependence of melanin's eventual structure based on environmental properties. Throughout this study, the aim is to directly correlate fluorescence properties with the morphology of melanin and its precursors.

In particular, there is an examination of the absorption, fluorescence and lifetime properties of L-DOPA correlated with well-studied naturally fluorescent amino acids – namely tryptophan, tyrosine and phenylalanine – thus allowing examination of the effect of its molecular structural characteristics on fluorescent properties.

Next, the role of environmental conditions on the formation of melanin from L-DOPA is examined, and in particular study two systems: one at pH 10 with the addition of ammonia; the other during heating to 37°C .

Lastly, research is reported on novel fibril structures observed during synthetic eumelanin formation. To allow direct comparisons of structure and photophysical properties, formations were measured using multiphoton fluorescence lifetime imaging, atomic force microscopy and electron microscopy, thus finally proposing an explanation for melanin fibril synthesis.

These studies reveal the continuing importance of the study of L-DOPA and melanin's chemical and structural properties in the battle against both Parkinson's disease and malignant melanomas.

Contents

1. Introduction	3
2. Background Theory, Instrumentation and Techniques.....	6
2.1 Fluorescence and Phosphorescence	6
2.2 Absorption.....	8
2.3 Absorption Instrumentation	10
2.4 Fluorescence Instrumentation	11
2.5 Quantum Yield.....	13
2.6 Time-Domain Fluorescence Lifetime	13
2.8 Reconvolution Analysis	17
2.9 Least-Squares Fitting	18
2.10 Maximum Entropy Lifetime Fitting.....	19
2.11 Fluorescence Anisotropy	21
2.12 Atomic Force Microscopy	22
2.13 Multiphoton Microscopy	26
2.14 Fluorescence Lifetime Imaging Microscopy	29
2.15 Fourier Transform Infrared Spectroscopy	32
2.16 Scanning Electron Microscopy	33
3. L-DOPA.....	35
3.1 Introduction.....	35
3.2 L-DOPA Experimental	37
3.3 L-DOPA Results	38
3.3.1 Absorbance, Fluorescence and Fluorescence Lifetime.....	38
3.3.2 Molar Extinction Coefficient	41
3.4 L-DOPA Summary	43
4. Eumelanin Formation From L-DOPA	44
4.1 Introduction.....	44
4.2 pH 10 Formation.....	46
4.2.1 pH 10 Formation Experimental	46
4.2.2 pH 10 Formation Results	48
4.2.2.1 pH 10 Absorbance and Emission Spectra.....	48
4.2.2.2 pH 10 Eumelanin Excitation Spectra Results	54
4.2.2.3 pH 10 Eumelanin Fluorescence Lifetime Results.....	56
4.2.2.4 pH 10 Maximum Entropy Results	64
4.2.2.5 pH 10 Copper Catalysed Eumelanin Results	67
4.3 High Temperature Neutral pH Formation of Eumelanin.....	72
4.3.1 High Temperature Neutral pH Formation Experimental	73
4.3.2 High Temperature Eumelanin Melanogenesis Results.....	73
4.3.2.1 High Temperature Absorbance, Fluorescence and Lifetime	73
4.4 Eumelanin Formation from L-DOPA Summary.....	79
5 Fibril Formation from Melanin.....	81
5.1 Introduction.....	81
5.2. Slide Treatment.....	83
5.3 pH 10 Eumelanin Formation.....	84
5.3.1 pH 10 Eumelanin Formation Experimental	84
5.3.2 pH 10 Fibril Formation Results	87

5.3.2.1 Bright Field Microscopy of pH 10 Fibril Formation	87
5.3.2.2 Multiphoton Microscopy of pH 10 Fibril Formation.....	89
5.3.2.3 FLIM Imaging of pH 10 Fibril Formation.....	91
5.3.2.4 Atomic Force Microscopy of pH 10 Fibril Formation.....	95
5.3.2.5 Fibril Scanning Electron Microscopy of pH 10 Fibril Formation	97
5.4 Fibril Formation at High Temperature.....	100
5.4.2 Fibril Formation at High Temperature Experimental	100
5.4.3 Fibril Formation at High Temperature Results.....	100
5.4.3.1 Bright Field Microscopy of High Temperature Fibril Formation.....	100
5.4.3.2 Multiphoton Microscopy of High Temperature Fibril Formation	102
5.4.3.3 FLIM Imaging of High Temperature Fibril Formation	103
5.4.3.4 Atomic Force Microscopy of High Temperature Fibril Formation...	107
5.4.3.5 Scanning Electron Microscopy of High Temperature Fibril Formation	111
5.5 Eumelanin Fibril Formation Summary	116
6. Dual Synthesis Pathways – a Model for Fibril Formation.....	118
6.1 Introduction.....	118
6.2 Dual Synthesis Pathway Experimentation.....	118
6.3 Dual Synthesis Pathway Results.....	119
6.4 Dual Synthesis Pathway Conclusions.....	122
7. Conclusions and Future Research.....	123
7.1 Conclusions.....	123
7.2 Future Research	125
References.....	127

1. Introduction

The use of fluorescence as a probe in molecular systems has found many applications due to its high sensitivity, accuracy and ease of use. Fluorescence is applied in many scientific disciplines: from its use in detecting chemicals used in food sciences¹⁻³, to its detection and even treatment of disease in medical sciences⁴⁻⁶. In skin cancer research, recent developments of both fluorescence lifetimes coupled with imaging techniques have been used to identify the sites of skin cancers⁷.

In both biology and medicine, the study of amino acids to help understand their role in the function of the human body is crucial. Of the amino acids only three are fluorescent, namely phenylalanine, tyrosine and tryptophan. Each of these amino acids produces fluorescence after excitation by ultraviolet (U.V.) light, specifically of wavelengths around 265 nm^{8,9}, 280 nm¹⁰ and 295 nm¹¹ respectively. Due to the fluorescent properties of the amino acids, fluorescence techniques are often used to study both their monomer forms and in their native forms in proteins and peptides. In doing so, valuable information may be taken in medically relevant processes in, for example, protein folding¹², complex formation¹³, or aggregation into fibrils¹⁴.

In particular, the tyrosine-derived amino acid L-3,4-dihydroxyphenylalanine (L-DOPA) has been studied due to its dual roles both naturally in the human body and during administration as treatment of disease. However, despite over 60 years of research, more information is needed to fully understand its processes in the human body.

Besides investigation into L-DOPA in its own right, its properties as a precursor molecule in melanin formation have also been investigated. However, despite a distinct and well-studied pathway of molecular precursors between L-DOPA and melanin, many questions still remained unanswered. For example, in spite of continuing research, the morphological structure of eumelanin is still highly debated.

One recent study into the structure of eumelanin designated it a clustered aggregate¹⁵, with another light scattering study designating it as fractal¹⁶.

Due to this lack of knowledge of melanin, advancements in the understanding of both its photophysical properties and its structure are advantageous. In this thesis, the role of L-DOPA as a melanin precursor is studied along with an experimental and theoretical hypothesis detailing the possibility for the melanogenesis process to form long, thin strand-aggregates or “fibrils”. Prior to beginning this work, the Photophysics Group had observed fibrils from L-DOPA that had been left for a period of a year or so. Thus, the main thrust of this work was to accelerate their formation and characterise the spectroscopy of the fibrils.

Typically fibrils are observed in protein or peptide systems such as alpha synuclein, associated with Parkinson’s disease, or beta amyloid, which is associated with Alzheimer’s disease. The propensity for the melanogenesis process to produce a fibril-like aggregate similar to the above has profound consequences in both its natural role in as a U.V. protector of skin and for L-DOPA’s role as a treatment for Parkinson’s disease. Indeed, previous studies have already highlighted the propensity for melanin formation in the brain called neuromelanin¹⁷, the loss of which in the brain may play a role in Parkinson’s disease¹⁸. The implication of melanin formation in the brain, coupled with previous studies strongly linking neural fibril formation with Alzheimer’s^{19,20}, Parkinson’s^{21,22} and Huntington’s^{23,24} diseases means that research into this field may well open hitherto unexplored avenues and new therapies.

Here we detail the investigation into eumelanin fibril formation via two broad types of scientific investigation, namely its photophysical characteristics by the use of fluorescence spectroscopy and its structural characteristics by the use of microscopy, with links between both showing the effect of structure on fluorescence response. Bridging both processes, fluorescence lifetime imaging (FLIM) of fibrils was also carried out, allowing us to directly correlate fluorescence and microscopy. Fibrils were produced under two different environmental conditions: one in high pH conditions and another in high temperature conditions, at 37°C at neutral pH. The photophysical characteristics of the fibrils were examined by steady-state and time

dependant fluorescence techniques and their structures studied by different forms of microscopy between millimeter and nanometer scales. Lastly, a model is proposed for the spontaneous formation of fibrils in the body, which may have important bearing on the use of L-DOPA in high concentrations as a treatment for Parkinson's disease.

Thus, after background information is provided on theory and techniques covered in this thesis, the following chapters (§3, §4) discuss the characteristics of L-DOPA and the formation of melanin, whilst the final chapters (§5, §6) detail the results of spontaneous fibril formation and propose a theory behind their formations. Lastly, some conclusions and future work are proposed in the final chapter (§7), offering a summation of the work carried out, followed by ideas for its expansion and continuation.

2. Background Theory, Instrumentation and Techniques

2.1 Fluorescence and Phosphorescence

Luminescence is the process by which light is emitted from an electronically excited state of a molecule. This emission of light may be further categorised by two distinct emission processes – fluorescence and phosphorescence.

In fluorescence, a molecule which has absorbed a photon with sufficient energy for transfer into a singlet excited state (according to equation 2.1) decays radiatively and thus emits a photon of light. This may be thought of as the promotion of an electron from the highest occupied molecular orbital (HOMO) state to the lowest unoccupied molecular orbital (LUMO), and thus with a finite “band gap” energy exists between the ground and singlet excited state, wherein the possibility of transition between these states is dependant on the wavelength of the incident photon. The excited state deactivation is quantum mechanically viable as the excited electron is spin-paired with an electron of opposite spin in the electronic ground state, and there is no change in the net spin.

Phosphorescence occurs when an electronically excited electron undergoes a transition from an excited triplet state. In this triplet state, decay to the electronic ground state is forbidden by quantum-mechanically derived selection rules due to same-spin electron pairing. Though these processes are termed as “forbidden”, this in reality describes a processes whose function is merely infrequent or has a small probability of occurrence. This explains the relatively long timescales of phosphorescence as compared to fluorescence.

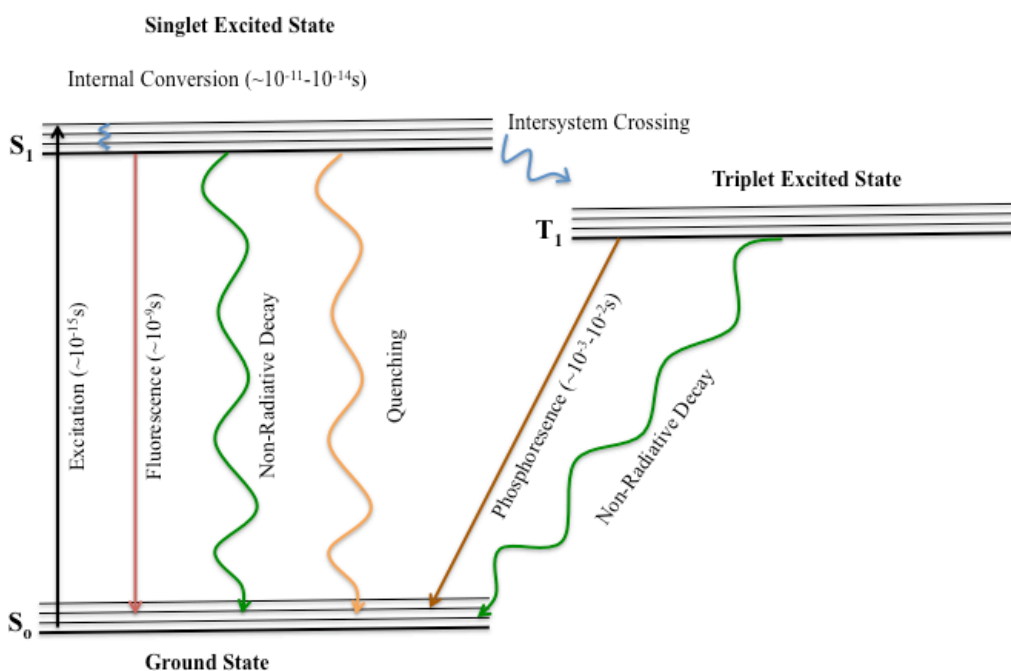


Figure 2.1 A Jablonski diagram indicating electronic and vibrational transitions.

Figure 2.1 shows a Jablonski diagram, which is often used to illustrate electronic states and their transitions. Increasing energy levels are shown at the top of the diagram *i.e.* excited singlet state S_1 and excited triplet state T_1 , whereas the lowest energy state, the ground state (S_0), is represented at the bottom of the diagram. Vibrational energy levels of molecules are also represented above each electronic energy level as fluorophores may exist in any of these discrete levels. The energy required to transfer an electron from the S_0 ground state into the S_1 excited singlet state, described by equation 2.1 is sufficiently large that excited state population may only occur by light interactions as opposed to thermal. However, thermal processes still affect the lower energy vibrational transitions occurring in molecules.

After absorption of light occurs to transfer an electron into an energetically excited state, it will often exist in one of its several vibrational states before quickly relaxing to the lowest vibrational level of the S_1 state. This process of internal conversion

usually occurs between 10^{-11} and 10^{-14} s, meaning that it will be completed before any fluorescence emission, which itself occurs around 10^{-9} , a fact that allows fluorescence to be used for molecular measurements. The internal conversion of electrons into the lowest vibrational level means that fluorescence processes occur at a lower energy than absorption, therefore a higher wavelength by Equation 2.1. This effect was first described by Sir George Gabriel Stokes in 1852²⁵ and was thus titled the “Stokes shift”. Other deactivation processes from the S_1 state may occur to transit the electron to the electronic ground state without luminescence such as non-radiative intramolecular decay and fluorescence quenching.

Transitions may also occur from the singlet excited state S_1 into an excited triplet state T_1 , known as intersystem crossing. Phosphorescence occurs at much longer times (10^{-4} and 10^{-2} s) and at a much lower rate as transitions between T_1 and S_0 are quantum mechanically forbidden.

2.2 Absorption

Excitation in a molecule from the ground state into an electronically excited state occurs when an electron absorbs one photon of light whose energy is described by:

$$E = h\nu = h\frac{c}{\lambda} \quad [2.1]$$

Where E is the photon energy (kJ mol^{-1}), h is Planck’s constant ($6.63 \times 10^{-34} \text{ Js}^{-1}$), ν is the frequency of incident light (Hz), c is the speed of light (ms^{-1}) and λ is the wavelength of incident light (m).

The energy of the incident light must be equal to the difference in energy between the electronic states to enable excitation of light into the given excited state.

The absorption of incident light by a fluorophore is directly measurable by the Beer-Lambert law:

$$I = I_0 \exp(-\epsilon cl) \quad [2.2]$$

also given as:

$$A = -\ln \frac{I}{I_0} = \epsilon' cl \quad [2.3]$$

and thus absorbance may be defined as:

$$A = \epsilon cl \quad [2.4]$$

and ϵ is related to ϵ' by:

$$\epsilon = 2.303\epsilon' \quad [2.5]$$

Where A is the measured absorbance, I is the transmitted light intensity, I_0 is the incident light intensity, ϵ is the wavelength-dependent absorption coefficient (or molar extinction coefficient) ($M^{-1} \text{ cm}^{-1}$), c is the fluorophore molar concentration (mol L^{-1}), and l is the path length (cm).

The molar extinction coefficient may be used separately to determine how strongly a fluorophore absorbs for a given wavelength. This value may be more useful than the absorption of a fluorophore due to the molar extinction coefficient value being independent of path length and concentration.

2.3 Absorption Instrumentation

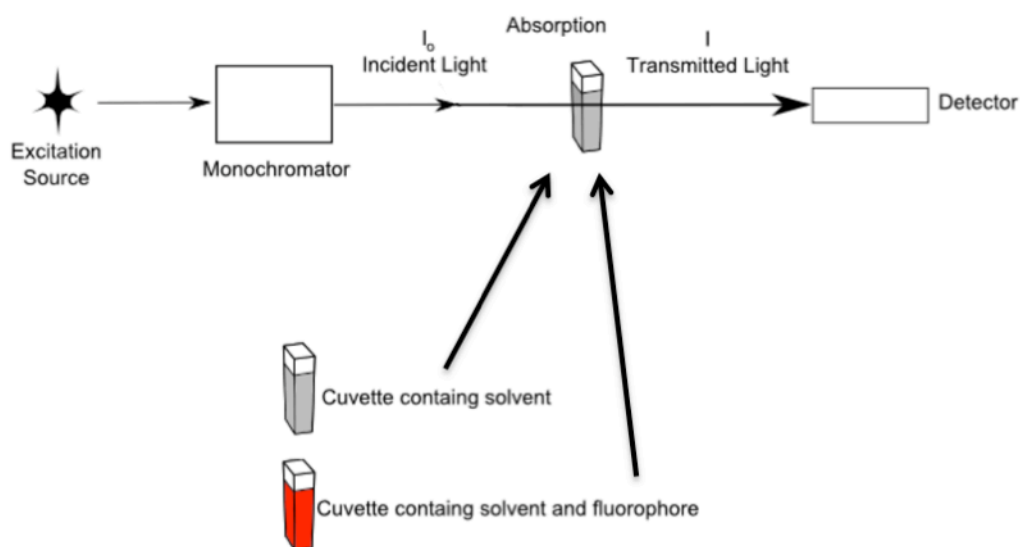


Figure 2.2 Schematic of absorption in a cuvette as measured using an absorption spectrophotometer.

Absorbance is measured using an absorption spectrophotometer, shown in Figure 2.2. Incident light from an excitation source is directed through a monochromator where it becomes wavelength-selected. This light is firstly incident on the cuvette containing only the solvent used to dilute the fluorophore. This means that the absorption spectrophotometer is able to take background reading of any absorbance due to both the cuvette and the solvent. Afterwards, the fluorophore is added to the cuvette and a final absorbance spectrum is produced giving the fluorophores absorption minus the absorbance effects of solvent and cuvette. The measurement of absorbance may also be carried out simultaneously by using a mirror-chopper in the path of the incident light at some stage after wavelength selection by the monochromator to direct light into two detector channels: one housing the cuvette containing solvent, and the other housing a second cuvette containing both the solvent and the fluorophore. However, absorption spectroscopy is best carried out by a single photomultiplier detector lying in the path of the transmitted to avoid effects of differing absorbance spectra between cuvettes.

The excitation source used in absorbance measurements typically comprises both a tungsten lamp for visible regions and a deuterium lamp for visible-U.V. regions. The

detector typically comprises a photodiode or charge-coupled device (CCD) to detect incident light.

The transmittance of this light may be defined as:

$$T = \frac{I}{I_0} \quad [2.6]$$

Where I and I_0 are as defined in equations 2.2 and 2.3.

2.4 Fluorescence Instrumentation

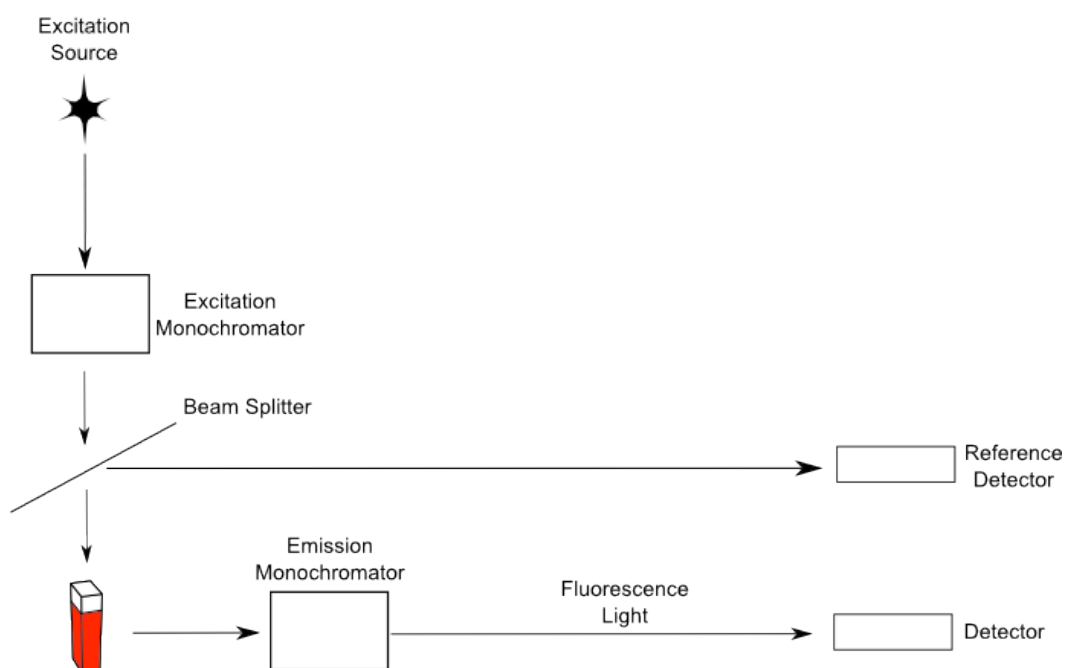


Figure 2.3 Schematic of fluorescence from fluorophores in a cuvette as measured using a fluorescence spectrophotometer.

Fluorescence emission from a fluorophore is measured as shown above in Figure 2.3. Light produced by an excitation source is incident on the fluorophore in a cuvette after travelling through an excitation monochromator. This allows a wavelength of light corresponding to the excitation wavelength of the fluorophore to be selected from the broad-band of wavelengths produced by the excitation source. Xenon-arc lamps are conventionally used as the excitation source in traditional fluorescence spectrophotometers. However, more recently, light-emitting diode (LED) excitation sources have become popular in fluorescence emission measurements due to their reliability and relatively high power²⁶. However, they are not as spectrally-broad as conventional discharge lamps.

The slit width of the monochromator determines the flux of excitation light reaching the cuvette, with a small slit width usually chosen to avoid effects of high irradiance on the sample such as high levels of scattered light in the detector, and also used to control resolution. For this reason, the fluorescence response of a sample is also measured at 90° to the excitation source, thus avoiding any excitation light transmitted through the sample from reaching the detector. Similarly to the excitation monochromator, an emission monochromator is used and usually maintained at a narrow slit width again to avoid high amounts of scattered light and to detect finer structures within the spectrum. However, both monochromators may be used at larger slit widths for measurements involving samples whose fluorescence intensity is small or whose emission wavelength is at a sufficiently large distance away from its excitation wavelength and therefore producing higher throughput from the monochromator. Besides this, the slit widths in each monochromator may also be used to vary the wavelength resolution of an experiment: the resolution is inversely proportional to the slit width in the monochromator, and therefore narrowing the slits will give a higher resolution between wavelengths. This may be of some use in higher quantum yield samples, where a trade in fluorescence intensity for a higher resolution may be more desirable. As with the fluorescence absorption spectrometer, measurement of light is usually via a photomultiplier detector.

When measuring excitation spectra, variations in the lamp profile over a range of wavelengths may lead to incorrect excitation spectra intensities. Therefore, a beamsplitter is often employed after the excitation monochromator to direct a fraction of the light through a reference detector, used to take account of this variation.

2.5 Quantum Yield

In fluorescence, quantum yield is the ratio of number of photons emitted to number of photons absorbed, or

$$\Phi = \frac{k_r}{k_r + k_{nr}} \quad [2.7]$$

Where Φ is the quantum yield, k_r is the rate of radiative decay (s^{-1}), and k_{nr} is the rate of non-radiative decay (s^{-1}).

This value is given as either a fraction approaching unity (unity $\equiv 1$) or as a percentage. For example, dyes such as Rhodamine or fluorescein have high quantum yields, with Rhodamine 101 having a quantum yield of 1 or 100%²⁷ meaning all photons absorbed will be emitted. On the other hand, the organic amino acid tryptophan has a quantum yield of 0.12 or 12%²⁸. Usually, fluorescent dyes have high quantum yields and thus have an intense fluorescence emission.

2.6 Time-Domain Fluorescence Lifetime

The fluorescence lifetime of a molecule is defined by the time that it spends in the excited state after absorption of a photon before decaying back to the ground state. This lifetime is usually in the order of a few nanoseconds but may be several tens of

nanoseconds to milliseconds for long lifetime fluorophores such as doped quantum dots²⁹.

Fluorescence lifetimes may be used as a probe in examination of a molecule's reaction to its local environment such as pH³⁰ and viscosity³¹. Furthermore, it may be used to determine static or dynamic quenching³² and resonance energy transfer³³.

The average lifetime may be related to the rate of decay of a molecule by the equation

$$\tau_M = \frac{1}{k_r + k_{nr}} = \frac{1}{k_M} \quad [2.8]$$

Where τ_M the average fluorescence lifetime (s) and k_M is the total decay rate (s^{-1}).

To measure fluorescence lifetimes, the fluorophore is excited by a pulsed light source, typically a laser or pulsed LED. The width of this pulse must be kept as short as possible in relation to the lifetime of the sample to allow an accurate lifetime to be taken. For example, one typical pulse width of a 280 nm IBH LED is around 600ps³⁴, a short pulse compared to the several nanoseconds that the average fluorophore will spend in the excited state.

This excitation pulse results in a fluorescence decay containing information on the lifetime of the fluorophore, which can be measured as the time the intensity falls to $\frac{1}{e}$ after delta pulse excitation.

Using a Jablonski diagram, a monoexponential lifetime can be described in terms of depopulation of the S_1 state by the equation

$$\frac{d[M^*]}{dt} = -k_m[M^*] = -\frac{[M^*]}{\tau_m} \quad [2.9]$$

And therefore

$$[M^*](t) = [M^*]_0 e^{-k_M t} = [M^*]_0 e^{-\frac{t}{\tau_M}} \quad [2.10]$$

Where $[M^*](t)$ is the excited state concentration at time t , $[M^*]_0$ is the excited state concentration at time $t = 0$, k_M is the total decay rate and τ_M is the molecular fluorescence lifetime.

The fluorescence lifetime, however, is typically given as a number of exponentials produced after excitation by incident light:

$$I(t) = \sum_i \alpha_i \exp\left(-\frac{t}{\tau_i}\right) \quad [2.11]$$

2.7 Time-Correlated Single Photon Counting

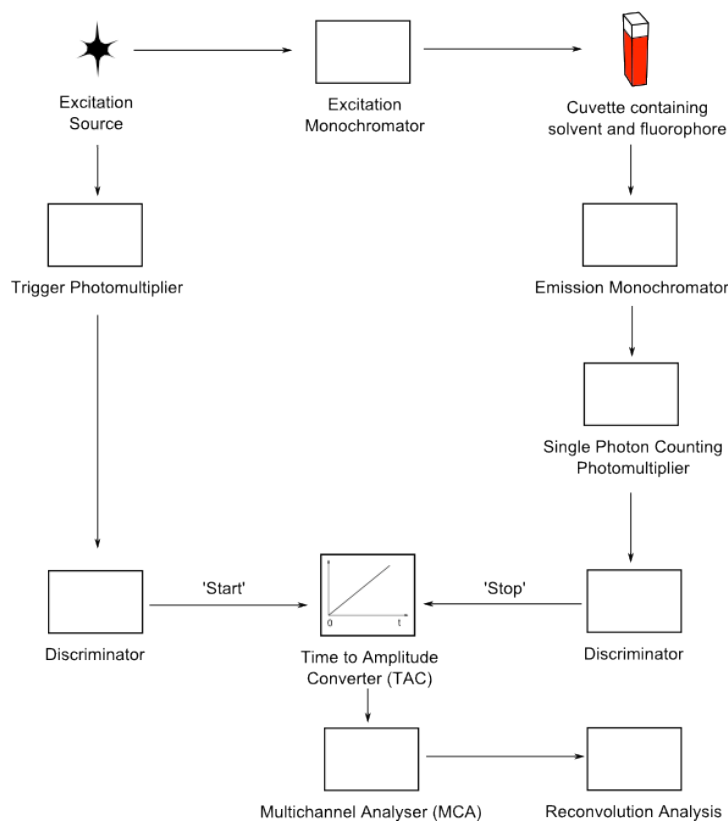


Figure 2.4 Schematic of Time-Correlated Single Photon Counting (TCSPC) instrumentation.

The measurement of fluorescence lifetimes is carried out on a time-correlated single photon counting (TCSPC) lifetime system as shown above in Figure 2.4.

In order to carry out TCSPC, a pulsed excitation source must be used. Recent developments have allowed LEDs to be used in this role, but laser sources and flash lamps have also traditionally been used³⁵. The sample excitation pulse travels through an excitation monochromator to allow for wavelength selection, after which the light travels into the cuvette containing the fluorophore in solvent. As with steady-state fluorescence emission measurements, monochromators are slit width selective to allow an optimised amount of light to reach the sample, and fluorescence is collected at right angles to the sample. Fluorescence emission light travels from the sample through an emission monochromator and into a single photon counting photomultiplier. Simultaneously to the generation of the excitation pulse, a trigger pulse is produced and travels from the excitation source through a trigger photomultiplier. Both pulses pass through discriminators, used to avoid unwanted effects of photomultipliers such as afterpulsing, timing jitters and pulse height distributions. The trigger pulse will reach the time-to-amplitude (TAC) converter as a 'start' signal, causing a capacitor to begin charging. Some time after this the fluorescence pulse will reach the capacitor as a 'stop' signal, causing the capacitor to discharge and a voltage to be output to the multichannel analyser (MCA). The MCA then distributes pulses into time channels dependant on their voltages. Each fluorescence pulse which reaches the TAC and subsequently the MCA causes the counts to rise in a particular time channel, thus creating a histogram showing a convoluted fluorescence decay and excitation pulse.

Afterwards, reconvolution analysis is carried out to correct for non δ -function excitation pulses, thus resulting in a fluorescence lifetime.

2.8 Reconvolution Analysis

When using the TCSPC instrument to measure lifetime, the experimental decay response produced does not initially reveal fluorescence lifetimes. Rather, the experimental decay is a convolution of both the fluorescence response of the fluorophore and the instrumental response. The excitation pulse produced from sources used for fluorescence lifetime acquisition is not an infinitely narrow δ -pulse, instead they produce a finitely broadened pulse, also partially due to effects of timing in components of the TCSPC instrument. Due to pulse broadening, reconvolution analysis must be used in order to establish the fluorescence lifetime of a fluorophore measured by such a system. Thus, using reconvolution analysis, we are able to measure the fluorescence lifetime by taking into consideration both the instrument response and a non-infinitely-narrow excitation pulse³⁶.

This convoluted decay is shown by the equation

$$F(t) = P(t) \otimes I(t) \quad [2.12]$$

Where $F(t)$ is the fluorescence decay, $P(t)$ is the instrument response profile and $I(t)$ is the impulse response function *i.e.* the response observed for a δ pulse excitation and δ function instrument response.

However $P(t)$, the instrument response profile, is itself a convolution given by equation

$$P(t) = D(t) \otimes E(t) \quad [2.13]$$

Where $P(t)$ is the instrument response profile, $D(t)$ is the detection system response and $E(t)$ is the excitation pulse response.

Using the convolution integral, equation 2.12 may be rewritten as

$$F(t) = \int_0^t P(t')i(t-t')dt \quad [2.14]$$

This equation states that $F(t)$, the experimentally measured decay, at time t is given by the sum of δ function pulses that occur until time t . Thus, the produced fluorescence signal may be defined as a product of the instrument response and an impulse response function taken at a time t after the instrument response.

2.9 Least-Squares Fitting

Many forms of fitting TCSPC data fitting are used to determine fluorescence lifetimes, ranging from maximum entropy methods used to fit complex structures³⁷ to Laplace transform³⁸, though this method is largely outdated. However, the most widely used method is least-squares fitting.

Least-squares fitting takes a model used to fit fluorescence data, in this case $F(t)$ as shown in equation 2.12, and tests the validity of this model by using a “goodness of fit” parameter, or χ^2 . The equation of goodness of fit is given by

$$\chi^2 = \sum \left[\frac{Y(i) - F_y(i)}{\sigma(i)} \right]^2 = \sum [W(i)]^2 \quad [2.15]$$

Where $Y(i)$ is the value of the measured fluorescence decay, $F_y(i)$ is the value of the fitting function, $\sigma(i)$ is the standard deviation and $W(i)$ are the weighted residuals.

This may be rewritten as

$$\chi^2 = \left[\frac{\text{Actual Deviation}}{\text{Expected Deviation}} \right]^2 \quad [2.16]$$

The model is determined to fit if the χ^2 parameter has value <1.2 , with 1 being a good fit and 1.2 being an acceptable fit. A fit value of higher than 1.2 may mean that there are errors in the data or simply that the fluorophore decay may be too complex to fit to the given function.

The weighted residuals produced by equation 2.16 are a display of the deviation of the fitting parameters with respect to a given time channel, *i.e.* showing which time channels in x in the fluorescence decay curve do not adhere to the model. An example of weighted residuals are shown below (Figure 2.5) for a fluorophore assumed to have a bi-exponential decay⁹.

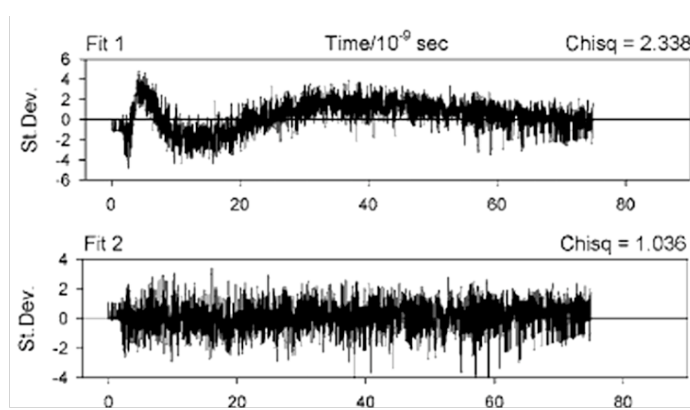


Figure 2.5 Weighted residuals taken for a biexponential-lifetime fluorophore. Residuals are given as monoexponential (top), displaying an unacceptable chi-squared value (2.338) and biexponential (bottom) displaying an acceptable chi-squared value (1.036)⁹.

2.10 Maximum Entropy Lifetime Fitting

Traditionally a least squares fitting method is used to fit fluorescence data, with the fluorescence decay consisting of a number of exponential components defined by:

$$I(t) = \sum_i \alpha_i \exp\left(\frac{-t}{\tau_i}\right) \quad [2.11]$$

For the example of a decay containing i components, where α_i is the relative amplitude of lifetime component i and τ_i is the mean lifetime of component i .

However, this function does not always properly define the fluorescence decay, especially in heterogeneous systems (*e.g.* complex proteins).

A better method to display lifetime components in these complex systems is by using lifetime distributions. However, a solely least-squares fitting method as used in the exponential fitting of lifetimes given in Figure 2.5 above is not useful for these lifetime distributions as it uses a predefined shape function⁴⁰. We may, though, use both the least squares method in conjunction with an entropy function to allow us to display lifetime distributions for these complex fluorophores.

Maximum entropy method (MEM) attempts to reconstruct data using no prior knowledge of the system. The method of using maximum entropy functions to fit data has been established in studies comprising both time-domain⁴¹ and frequency-domain⁴² fluorescence for over 20 years, though its use is infrequent. Maximum entropy is carried out by using the formula:

$$S(\alpha) = \int [\alpha(\tau) - m(\tau) - \alpha(\tau) \log \frac{\alpha(\tau)}{m(\tau)}] d\tau \quad [2.17]$$

where α is the relative amplitude of the lifetime component, τ is the mean lifetime of the sample and $m(\tau)$ is a uniform fitting component.

This equation attempts to measure the deviation of $\alpha(\tau)$ from the function $m(\tau)$. However, since no prior knowledge of the system is known, $m(\tau)$ is taken to be uniform and featureless.

The maximum entropy method will attempt to output a distribution based on the criteria that the entropy values are maximised whilst the chi-squared values are minimised. Thus, the output is a two-parameter fitting procedure which applies more stringent rules to fitting complex decay mechanisms.

2.11 Fluorescence Anisotropy

Fluorescence anisotropy is a measure of the polarised emission of a fluorophore after undergoing polarised excitation. In a solution, the transition moments of fluorophores distributed throughout the sample are randomly oriented. Under irradiation with polarised light, fluorophores whose absorption transition moments are oriented in the same axis as polarisation of incident excitation light are excited preferentially, whilst those with absorption transition moments oriented in other directions are not. In solution, molecules will freely rotate due to Brownian motion. Whilst undergoing this rotation, the direction of the absorption transition moments will change, and hence their anisotropy becomes depolarised. This means that the fluorescence anisotropy may be used as a measure of the rotational times of fluorophores excited with polarised light. This is often used to reveal further information of both the fluorophore and the solvent such as hydrodynamic radii⁴³, viscosity⁴⁴ and temperature⁴⁵.

The fluorescence anisotropy is defined by the equation

$$r(t) = \frac{I_{vv}(t) - GI_{vh}(t)}{I_{vv}(t) + 2GI_{vh}(t)} \quad [2.18]$$

where G is the G-factor (a ratio which takes into account the directional sensitivity of the detector), I_{vv} is the vertically polarised emission intensity and I_{vh} is horizontally polarised emission intensity. Incident excitation light is assumed to be vertically polarised.

When excited by a pulsed source such as LEDs, the fluorescence anisotropy decay of a fluorophore may be expressed by the equation

$$r(t) = \sum_i r_i(0) \exp\left(-\frac{t}{\phi_i}\right) \quad [2.19]$$

where $r_i(0)$ is the anisotropy at $t=0$, and ϕ_i is the rotational correlation time of the fluorophore. Similar to fluorescence lifetimes, there may be i number of rotational correlation times depending on local properties of fluorophore.

2.12 Atomic Force Microscopy

Atomic Force Microscopy (AFM) is a method of producing high-resolution images of a microscopic area using the forces acting on a nano-scale metallic tip brought into close proximity with a sample deposited on a substrate. The metallic tip is attached to a cantilever that is moved micrometer distances, using a precise piezoelectric motor, towards the sample until it feels a force due to small-distance interactions with molecules deposited onto a substrate (such as mica or glass). At large distances, the tip feels no force from the sample. At close distances to the surface of the sample, the tip will be repulsed from the surface. This distance-force effect is shown in Figure 2.5. Forces that cause this may be due to, for example, simple contact forces or van der Waals forces.

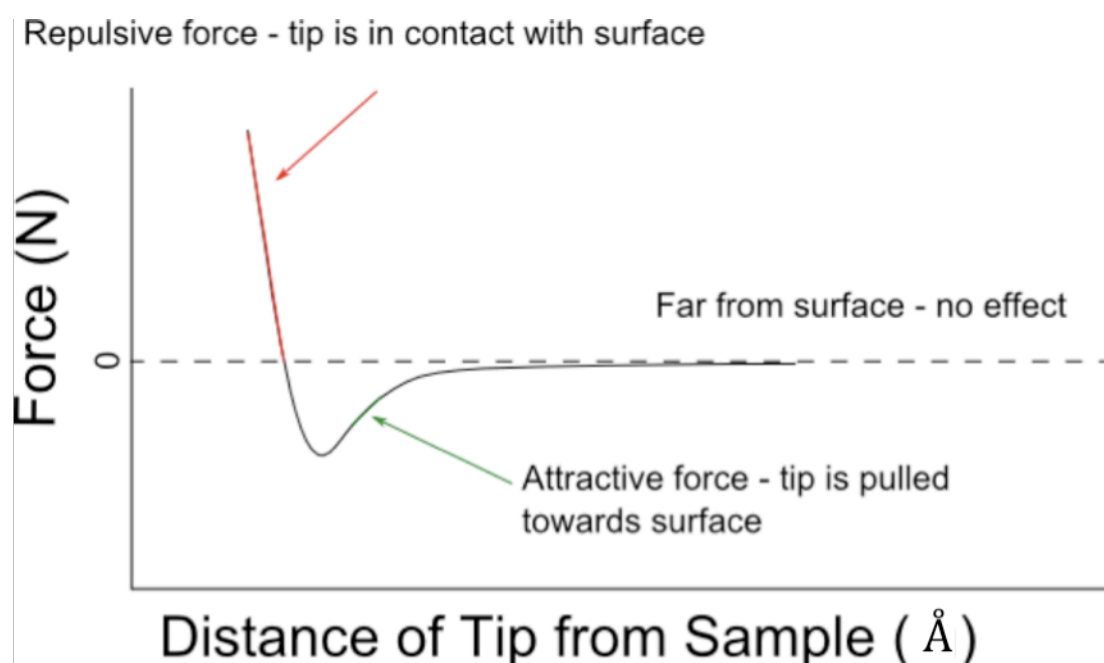


Figure 2.5 Force experienced by the AFM cantilever tip as a function of distance from the sample.

This force-distance effect between tip and sample may be described by the Lennard-Jones equation arising from molecular interactions producing a potential where:

$$v(r) \sim \left(\frac{1}{r^{12}} - \frac{1}{r^6} \right) \quad [2.20]$$

Where $v(r)$ is the potential and r is the distance between the interacting molecules.

Thus the force is described by:

$$F(r) = -\frac{dv(r)}{dr} \quad [2.21]$$

Generally, AFM is carried out in one of two modes – contact mode or tapping mode. In contact mode, the AFM tip makes permanent contact with the surface and scans by dragging the tip over a predefined area. The forces acting on the tip, given by Hooke's law, are fed back to the computer, allowing an image to be produced. However this type of scanning is usually destructive to the surface and does not provide a clear image of the surface as it may cause the sample to be moved on top of the substrate. Tapping mode is useful in this regard as contact with the surface is only brief, allowing scanning of less rigid samples.

In tapping mode, the cantilever tip is oscillated at a given resonance frequency, *e.g.* 265kHz, where it only comes into occasional contact with the surface, as shown in Figure 2.6. A laser is incident on the top of the cantilever and deflected through paired photomultipliers, shown in Figure 2.7.

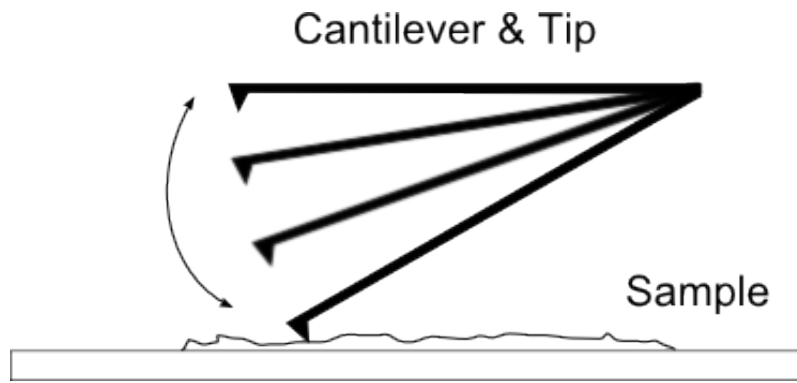


Figure 2.6 Interaction between cantilever & tip and sample surface when operated in AC (tapping) mode.

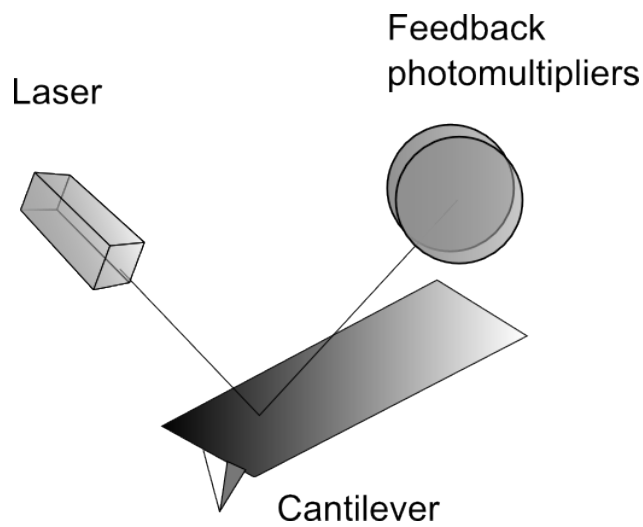


Figure 2.7 Feedback photomultiplier system used by AFM microscopes to measure surface contact.

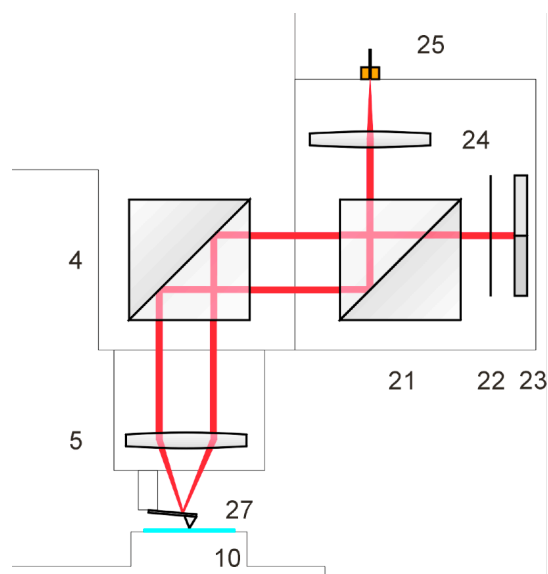


Figure 2.8 Beam path for Vitec AlphaSNOM AFM showing: **4** dichroic mirror; **5** objective lens system; **10** sample; **21** cube beamsplitter; **22** edge filter; **23** segmented photodiode; **24** achromatic lens system; **25** fiberoptic input; **27** AFM cantilever. Figure is adapted from Witec AlphaSNOM manual⁴⁶.

The laser signal directed through the feedback photomultiplier is used to calculate when contact has been made with the surface using the feedback voltage from the z stage. The voltage is routed through the z-piezoelectric to allow the system to monitor whether the tip is touching the surface of the sample, as a dampening effect will occur once in contact. Hence this feedback mechanism is able to maintain a constant tapping distance from the surface irrespective of the surface topography. This is advantageous when compared to contact mode as no molecules are dragged and the tip is rarely damaged during the course of a measurement. A diagram of the beam path which the light takes through the AFM is shown in Figure 2.8.

Atomic force microscopy is often used as a high-resolution microscopy in systems in place of higher resolution techniques such as SEM due to there being no need for vacuum and its ability to scan non-conducting organic substances that cannot conduct and are therefore difficult to measure without some modification due to their build-up of charge. Furthermore, the resolution of AFM is limited only by the narrowness of the contact tip, and therefore has the possibility to measure the interaction between single atoms⁴⁷.

2.13 Multiphoton Microscopy

In fluorescence, typically a molecule will reach the excited state by absorption of a photon whose energy is equivalent to the energy gap between those states as given in Equation 2.1:

$$E_2 - E_1 = h\nu = \frac{hc}{\lambda} \quad [2.1]$$

where $E_2 - E_1$ is the energy difference between excited state and ground state, h is Planck's constant ($=6.626068 \times 10^{-34}$ Js), ν is the frequency of absorbed light (Hz), c is the speed of light (m/s) and λ is the wavelength of the absorbed light (m).

However, molecules may be able to reach these higher energy states by absorption of two, three or more photons. This occurs by the electron first reaching a virtual electronic state where it only lasts for a short period of time, at which time it is possible to absorb further photons and thus be excited into higher energy states. This process is shown below in Figure 2.9. This means that for a multiphoton absorption process to occur we must have laser excitation of a suitably high flux that the electron may absorb another photon in a short enough time-period that would now allow it to decay to the ground state. This process is called stepwise two-photon absorption. Similarly, a process may occur wherein the electron absorbs both photons in a simultaneous event, named simultaneous two-photon absorption. Hence, a laser with high peak power is essential for multiphoton absorption and microscopy.

The excitation into the S_1 state via an intermediary virtual energy level should not be confused with up-conversion of molecules, for example lanthanides⁴⁸, into higher level real excited states.

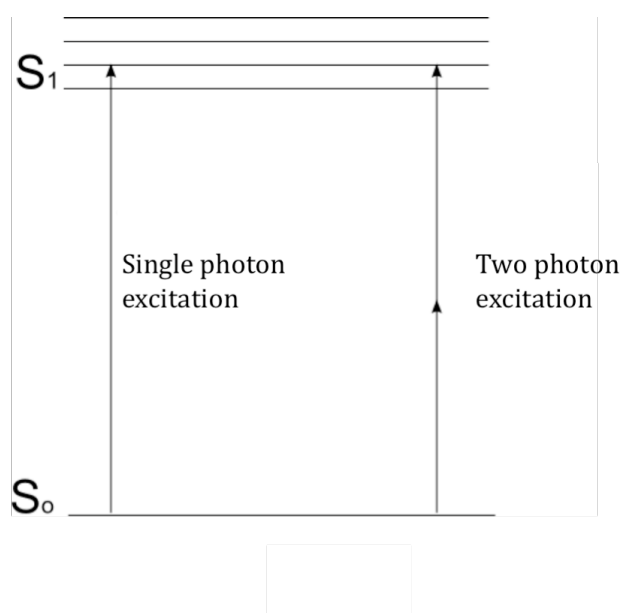


Figure 2.9 Single and two photon absorption in a fluorophore as displayed on a Jablonski diagram.

The number of photons absorbed in this process is given by the equation:

$$NA_2 = \sigma_2 I^2 \quad [2.22]$$

where NA_2 is the number of photons absorbed per second in two photon excitation (photons/s), σ_2 is the two photon cross section ($\text{cm}^4\text{s}/\text{photon}$) and I is the intensity of incident light ($\text{photons}/\text{cm}^2\text{s}$).

Due to multiphotonic processes occurring between two or more photons of light and a molecule, the selection rules for multiphotonic processes are different and therefore a fluorophore with a low single photon cross-section may have a high multiphoton-cross section when absorbing two photons of lower energies.

Multiphoton processes differ greatly from single photon processes, many of which are advantageous in probing samples. Multiphoton excitation will result in some penetration depth of a sample due to the typically higher wavelengths used for excitation. The difference between single photon and multiphoton penetration depths is shown in Figure 2.10.

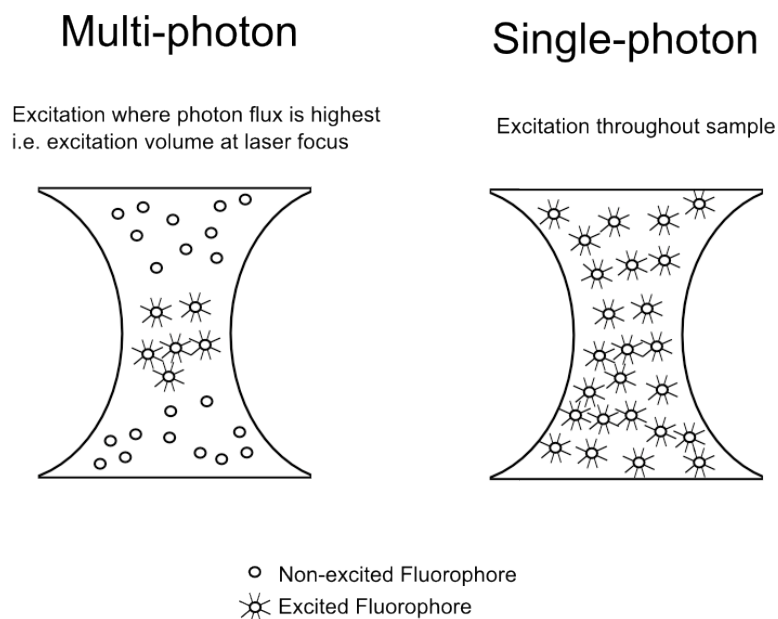


Figure 2.10 Excitation volumes during single and two photon excitation of a sample.

In single photon excitation, sample irradiation occurs through the depth of the sample. This means at high energies the entire sample in the beam path has the potential to be damaged. Conversely, with multiphoton excitation only a small excitation volume occurs at the focus of the beam. This means that any part of the sample outside of this depth is preserved, and any damage to the sample will largely be contained within this volume. This is especially advantageous during examination of living tissues or in-vivo systems where samples may be fragile.

Due to the high penetration-depth offered by using multiphotonic systems to excite fluorophores with two or more photons of lower energy, multiphoton measurement has become popular in life sciences for in-vivo monitoring in areas of the body which were, until its conception, difficult or impossible to measure. For example, measurements may now be made in-vivo on a live mouse to monitor the movement of leukocytes through vascular tissue⁴⁹, or for the measurement of amyloid plaques in a skull-thinned mouse brain⁵⁰.

based laser systems⁵². Furthermore, many early studies⁵³ were carried out in phase-domain fluorescence due to the lack of high pulse-rate scanning laser systems which have only been developed around the last decade, and the ease of detection using array detectors. These studies used novel phase-domain lifetime systems to produce fluorescence lifetime images of, for example, europium complexes⁵⁴ and ethidium-bromide stained leaf stroma⁵⁵.

FLIM operates on similar principles to multiphoton fluorescence microscopy. However, a dedicated lifetime card must be used to carry out lifetime analysis. As well as intensity and position, which is available from standard multiphoton microscopy, the lifetime each pixel of the image must be taken and therefore start-stop signals must also be generated. This means that there are three separate parameters recorded: x position, y position, and time. The x and y positions are measured via the scanning interface, with the decay time being measured similarly to a standard TCSPC measurement (as described in §2.7). This setup used for these recordings is shown below in Figure 2.12.

FLIM is of particular use in life and biological sciences, where background autofluorescence is present at visible wavelengths due to species such as collagen⁵⁶ and elastin⁵⁷, meaning lifetimes may be used to differentiate this background from the emission of a fluorophore tag who may have a similar fluorescence emission wavelength to an autofluorescent product.

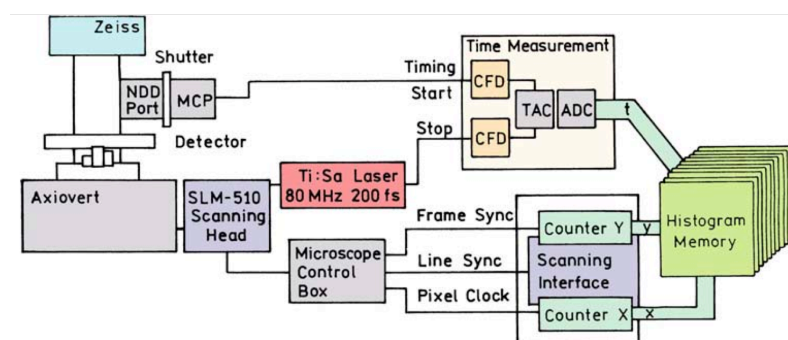
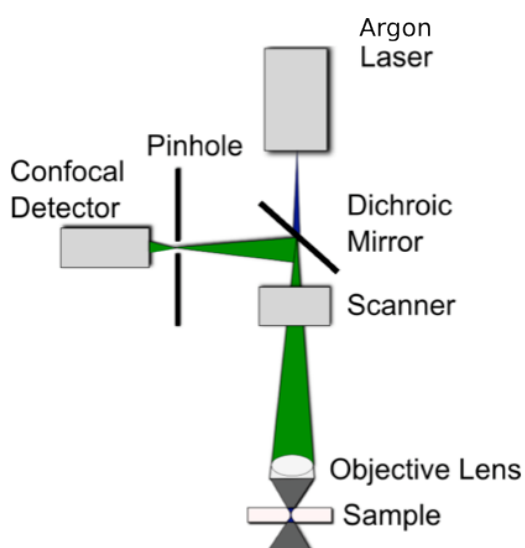


Figure 2.12 Schematic of fluorescence lifetime imaging (FLIM) microscope indicating both time components, as in a TCSPC system, and (x,y) spatial components, as given by Duncan et al⁵⁸.

The set up for single confocal (a) and multiphoton (b) excitation is shown in Figure 2.13. Excitation laser light is incident on the LSM scanning head, used to selectively scan an x,y-area of the sample. Emission light is reflected from a dichroic mirror into the confocal detector via a pinhole. The pinhole is crucial in confocal detection to reject out of focus light whereas in multiphoton excitation out of focus light is rejected during sample excitation. Hence, the non-descanned detector (NDD) for multiphoton excitation is used without a pinhole, as shown in (b).

(a)



(b)

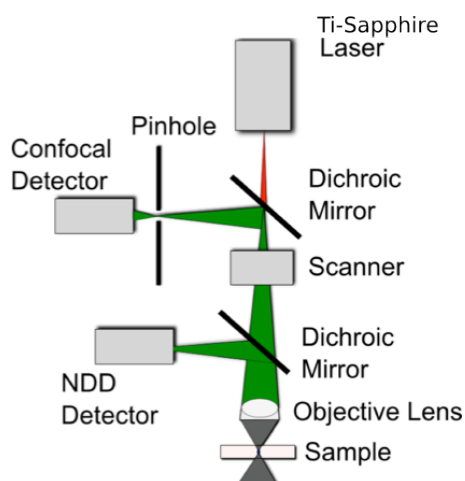


Figure 2.13 Microscopy system used in both single (a) and multiphoton (b) excitation of samples.

2.15 Fourier Transform Infrared Spectroscopy

Fourier transform infrared (FTIR) spectroscopy uses principles similar to absorption spectroscopy (§2.2), though instead of visible and near-U.V. light in the region of ~800 nm to 190 nm, FTIR spectroscopy irradiates samples with lower energy, near infrared (NIR) radiation over wavelengths ~2.5 – 1 μm to measure vibrational modes of the sample.

FTIR relies on the principle that each molecule has a unique vibrational spectrum, again analogous to visible light absorption where each molecule has a unique absorption spectrum. The vibrational peaks in an FTIR spectrum match the resonant vibrations of the bonds in the molecule which are due to varying types of bond motion e.g. symmetrical stretching, asymmetrical stretching or scissoring. When the incident light is at the same frequency as these resonance bond vibrations, a peak in the FTIR spectrum is observed. For example, the infrared spectrum of water has a peak at 1650 cm^{-1} due to OH bending⁵⁹.

In a Fourier transform, a function is applied to a system allowing its domain to be varied between two distinct parameters, typically from a time-dependant function to a frequency-dependant function. It is represented by the equation:

$$f(\nu) = \int_{-\infty}^{\infty} f(t) \exp(-2\pi i t \nu) dt \quad [2.23]$$

Where ν is frequency (Hz) and t is time (s).

Conventionally, infrared spectra were measured using a monochromator, as is the case with visible spectra. However, more recently, an interferometer is used wherein the incident infrared light is incident on a beamsplitter, splitting the beam between one fixed and one moving mirror before passing through the sample. This allows an interference pattern to be taken before it is Fourier-transformed (using a Fourier-transform equation as in 2.23) to produce the final wavenumber-dependant spectra.

Hence, all frequencies are measured immediately, rather than sequentially as in typical visible spectroscopy, leading to an improvement in both speed of measurement and signal-noise ratio.

2.16 Scanning Electron Microscopy

Scanning electron microscopy (SEM) uses a beam of focused electrons to measure high resolution and magnification images of sample molecules deposited onto a substrate. SEM has advantages over conventional light microscopy, one of which being that resolution is not diffraction limited to around 200 nm as with visible light microscopy.

To produce these images, electrons are generated in an electron gun near the top of the microscope under vacuum. The vacuum is used to ensure that electrons are not scattered and to prevent damage or erosion to the electron gun. The electrons are typically produced by field emission from a narrow tungsten tip of diameter < 100nm.

After generation at the electron gun, electrons are accelerated through condenser lenses and apertures used to focus the electrons on the sample. The on-sample spot size is around 1-2 nm and electrons upon contact have energies of around 0.5 kV. During scanning, the beam of electrons passes over the sample in a raster-scanning

pattern using scanning coils that deflect the beam. Concurrent with this raster-scan, the position of the beam is fed back to the computer to generate a position to match the signal from the detector.

Many types of detection are used to measure SEM images such as back-scattering⁶⁰, x-ray analysis⁶¹, secondary electron imaging⁶² and energy-dispersive x-ray analysis⁶³.

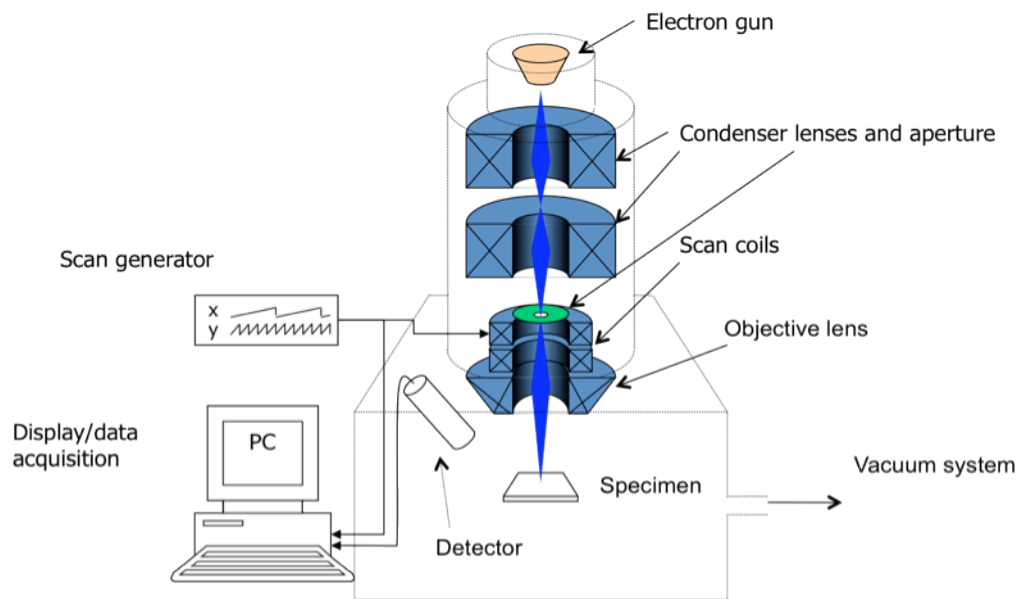


Figure 2.14 A typical scanning electron microscope.

The schematic of a typical scanning electron microscope is shown above in Figure 2.14, mapping the path of electrons from the electron gun to the detector.

3. L-DOPA

3.1 Introduction

L-DOPA is a natural amino acid derivative produced in the body by the tyrosinase enzyme-catalysed reaction of tyrosine, its precursor amino acid. Its chemical structure is included in Figure 3.1

Primarily, the purpose of L-DOPA in the body is the synthesis of melanin. The formation occurs via several intermediate synthetic stages, each with a different molecular structure and subsequently different photophysical properties *i.e.* absorption, fluorescence emission and lifetimes. This synthetic path formation of melanin is also true of in-vitro formation. The formation of eumelanin from L-DOPA is shown below in Figure 3.1. The molecules are shown in their zwitterionic state. It should be further noted that deprotonation of phenolic groups of L-DOPA occurs at around pH 8.9⁶⁴, meaning pH values used in some part of this study (~pH 10) must take the deprotonation state of these groups into account.

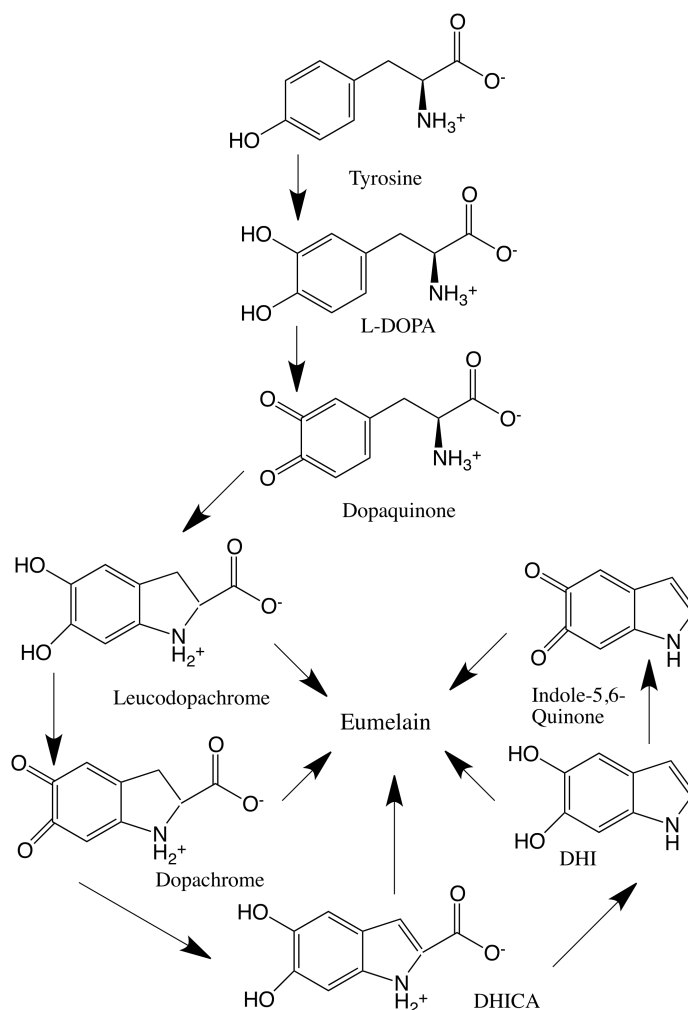


Figure 3.1 Synthesis of eumelanin and its precursors from tyrosine showing their zwitterionic structures. Diagram is adapted from Fitzpatrick et al⁶⁵.

Besides its production by melanocytes, L-DOPA is administered in pill form as a treatment for Parkinson's disease, a chronic degenerative disorder of the brain causing motor skill deterioration over a period of time, characterised by small tremors and muscle stiffness in sufferers. These symptoms are due to insufficient levels of dopamine in the brain. However, giving patients direct doses of dopamine is not a viable treatment as it is not able to cross the blood-brain barrier and therefore cannot reach the motor cortex, so instead L-DOPA is given. With the enzyme dopa-decarboxylase present in the body, L-DOPA – which may itself cross the blood-brain barrier due to a high blood-brain permeability⁶⁶ – is catalysed to dopamine, and further to epinephrine and norepinephrine in the brain. Early studies in 1969 by Barbeau were instrumental in its use as a treatment of Parkinson's disease⁶⁷.

3.2 L-DOPA Experimental

L-DOPA (>99%), tyrosine (>99%) and phenylalanine (>99%), all powdered form, were obtained from Sigma-Aldrich Co. (Dorset, UK). Water used to dissolve amino acids was U.V. filtered to ensure it was at highest purity. Checks for background contaminants were carried out with excitation by a 280nm IBH pulsed LEDs and were found to have very little to no contaminating background species. Absorption and molar extinction coefficient measurements were carried out using a Perkin Elmer Lambda 2 spectrometer and fluorescence measurements were carried out using a Perkin Elmer LS-50 fluorescence spectrometer (Cambridgeshire, UK). All experiments were carried out in 6Q 4×1×1 quartz cuvettes obtained from Starna Scientific Ltd. (Essex, UK) which are usable between wavelengths of 170nm and 2700nm. Fluorescence Lifetime measurements were carried out using an IBH 5000U fluorescence lifetime system obtained from Horiba Jobin Yvon IBH Ltd. (Glasgow, UK). 265nm and 280nm IBH Pulsed LEDs (Glasgow, UK) were used for the excitation of phenylalanine, L-DOPA and tyrosine, and were operated at 1MHz repetition with pulse widths of 1.2ns and 600ps respectively. Emission monochromators were set at 280nm, 300nm and 320nm respectively. Excitation and emission monochromator slits were opened to a 6nm bandpass. Each amino acid was diluted to a concentration of 40 μ m for absorption, fluorescence and lifetime acquisitions.

Fluorophores used in this section were dissolved in pure dionized water. Their pH was measured with pH 0-14 test paper (Sigma Aldrich, UK) to be approximately pH 7. Despite the inaccuracy of this method and the likely high margin of error, pH paper was used to maintain consistency with pH 10 results presented later. All values taken during this method should be taken to be approximate values, though their pH is within ± 1 of the stated values.

3.3 L-DOPA Results

3.3.1 Absorbance, Fluorescence and Fluorescence Lifetime

Absorbance spectra of L-DOPA, tyrosine and phenylalanine were measured at pH 7 in aqueous solution. L-DOPA shows high fluorescence intensity in the U.V., with a peak excitation wavelength around 280nm. Figure 3.2 shows that L-DOPA's absorbance spectrum is similar to both phenylalanine and tyrosine, whose molecular structure resembles L-DOPA (as shown in Figure 3.2 Insert). From the increasing red shift moving from phenylalanine – which has no –OH groups on the phenyl ring and absorbance spectra around 265nm – to L-DOPA – which has two –OH groups on the phenyl ring and absorbance spectra around 280nm – it may be assumed that lower energy excitation spectra are due solely to an increase in hydroxyl groups in the molecular structure.

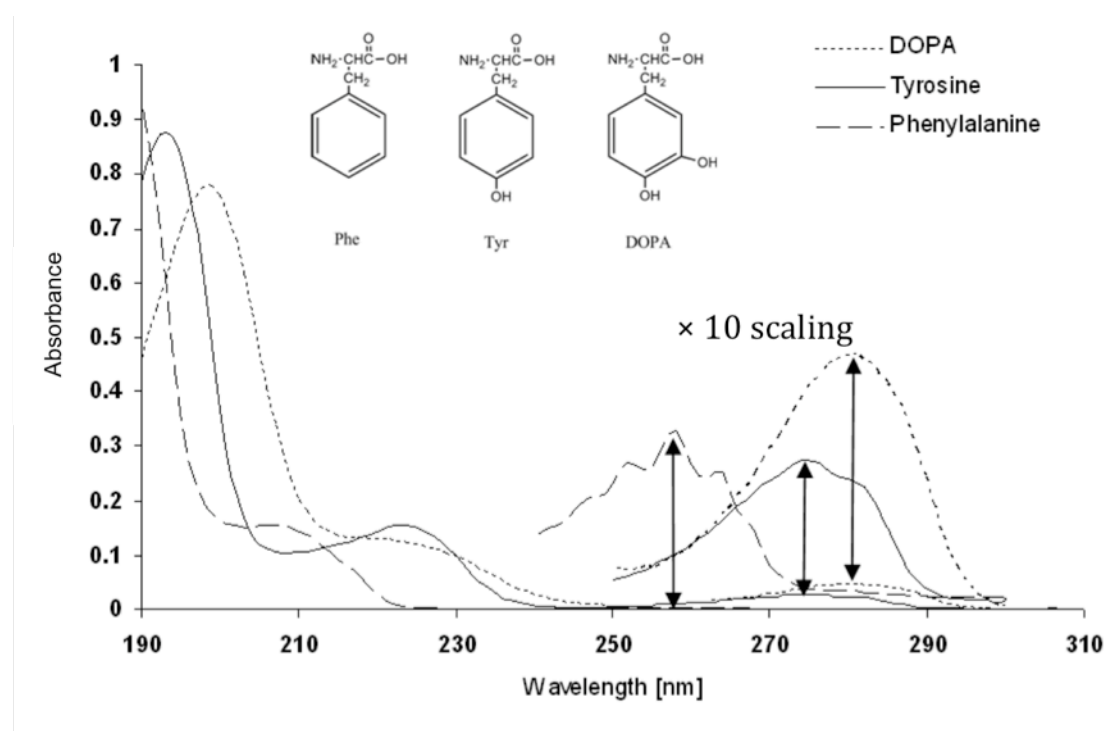


Figure 3.2 Absorbance spectrum of two naturally occurring fluorescent amino acids (tyrosine, phenylalanine) and tyrosine's amino acid derivative, L-DOPA.

Similarly, we see an increasing red-shift in the fluorescence spectra for increasing –OH groups, as shown below in Figure 3.3. Phenylalanine has a fluorescence emission peak at around 280nm, whereas L-DOPA containing the most –OH groups on the phenyl ring has a fluorescence emission peak at around 320nm. Each amino acid was excited at its peak absorption wavelength: phenylalanine $\lambda_{ex}=265\text{nm}$, tyrosine $\lambda_{ex}=275\text{nm}$, L-DOPA $\lambda_{ex}=280\text{nm}$.

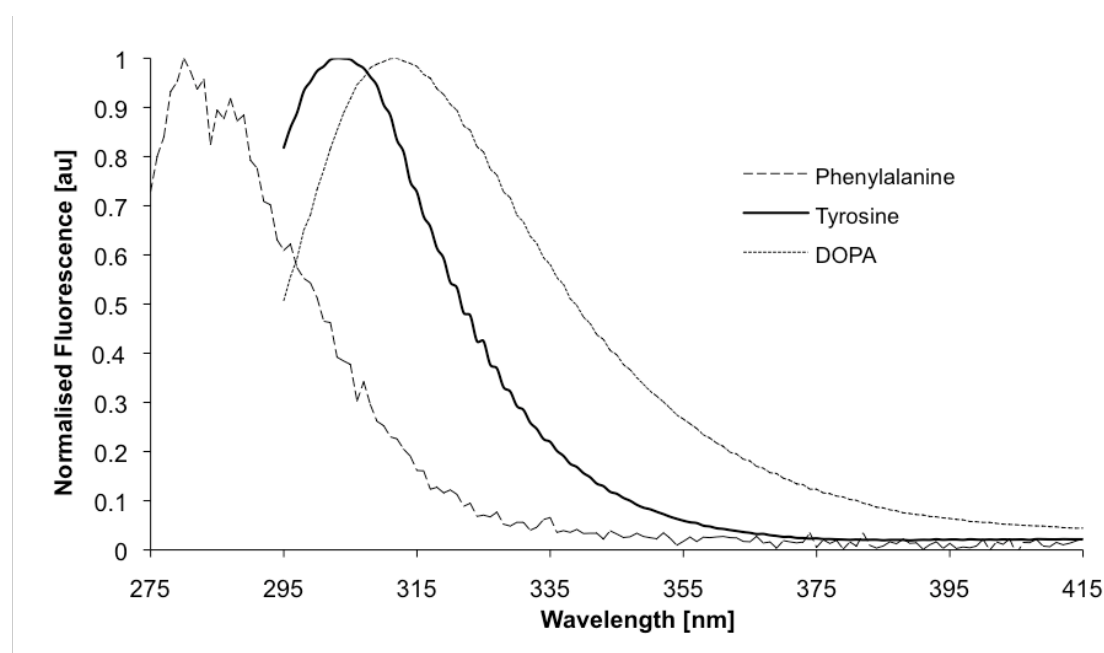


Figure 3.3 Fluorescence spectra of two naturally occurring fluorescent amino acids (tyrosine, phenylalanine) and tyrosine's amino acid derivative, L-DOPA. Normalised fluorescence units (au) signify arbitrary units.

From Table 3.1, the fluorescence lifetime values for each fluorophore are observed to be quenched under the presence of increasing –OH groups on the phenyl ring. The decrease in lifetime is due to excited state deprotonation of the hydroxyl groups causing a fluorescence quenching. The effect of the deprotonation becomes larger with increasing hydroxyl groups, and subsequently the fluorescence lifetime of the group with the largest number of hydroxyl groups on the fluorescent benzene ring (L-DOPA) is quenched most dramatically. Therefore, we see a decrease in fluorescence lifetimes for increasing hydroxyl groups present in the molecule.

From the fluorescence decays given, phenylalanine displays a two-exponential decay under pH 7 conditions as highlighted in §3.2. In solution, phenylalanine may be present in two or more conformations dependant on the position of the side chain of the molecule in relation to the phenyl group. The presence of rotamers of L-DOPA in solution, then, may also be a possibility, but was not observed in this instance.

Amino Acid	Excitation Wavelength (nm)	τ_1 (ns)	α_1 (%)	τ_2 (ns)	α_2 (%)	χ^2
Phenylalanine	265	5.87	92.2	3.9	7.8	1.06
Tyrosine	275	3.40	100	--	--	1.16
L-DOPA	280	1.02	100	--	--	1.10

Table 3.2 Fluorescence lifetime values of two naturally occurring fluorescent amino acids (tyrosine, phenylalanine) and tyrosine's amino acid derivative, L-DOPA. Phenylalanine appears as a rotamer at pH 7, thus has a two exponential decay.

Similar effects of additional hydroxyl group additions to phenyl rings of porphyrin show an analogous effect of red-shifted fluorescence and shortening of lifetimes⁶⁸, and in coumarin compounds where addition of -OH groups caused a red-shift of both absorbance and fluorescence⁶⁹. In the latter case, this was attributed to increased π -electron mobility on the benzene ring. It should also be noted that the authors state this mobility as an explanation for an increased fluorescence intensity, which may explain the large change in observed fluorescence intensity between phenylalanine and tyrosine. This is also directly observable in the greater quantum yields of both tyrosine and L-DOPA compared with phenylalanine.

Amino Acid	Quantum Yield at pH 7
Phenylalanine	0.024 ⁷⁰
Tyrosine	0.14 ⁷¹
L-DOPA	0.06 ⁷²

Table 3.3 Quantum Yields at pH 7 of aqueous phenylalanine, tyrosine and L-DOPA.

3.3.2 Molar Extinction Coefficient

L-DOPA's molar extinction coefficient was calculated at pH7 and compared to previously stated values for phenylalanine⁷³ and tyrosine⁷⁴. The molar extinction coefficient of L-DOPA was calculated experimentally to be $2566 \pm 128 \text{ M}^{-1}\text{cm}^{-1}$, in good agreement with previous research showing L-DOPA to produce a molar extinction coefficient of $2552 \pm 150 \text{ M}^{-1}\text{cm}^{-1}$ ⁷⁵. The change in absorbance with respect to volume of L-DOPA added is shown below in Figure 3.4. Using the Beer-Lambert law, Equation 2.4, the molar extinction coefficient was derived from the gradient of the linear fit (Figure 3.5).

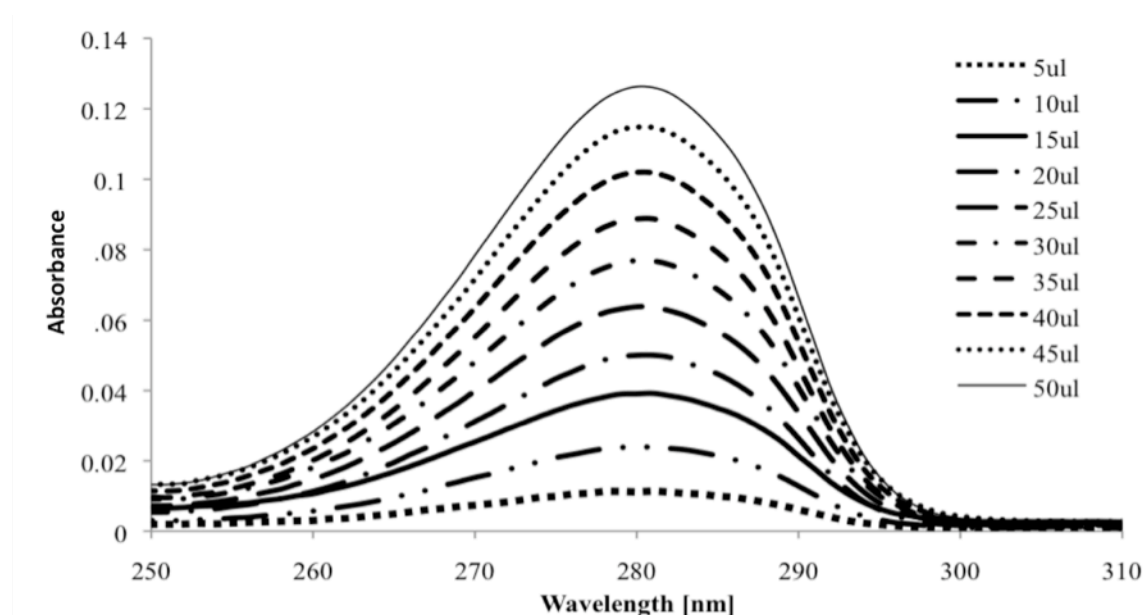


Figure 3.4 Changing absorbance values with respect to volumes of L-DOPA added to a sample. These spectra are used to calculate L-DOPA's molar extinction coefficient (ϵ)

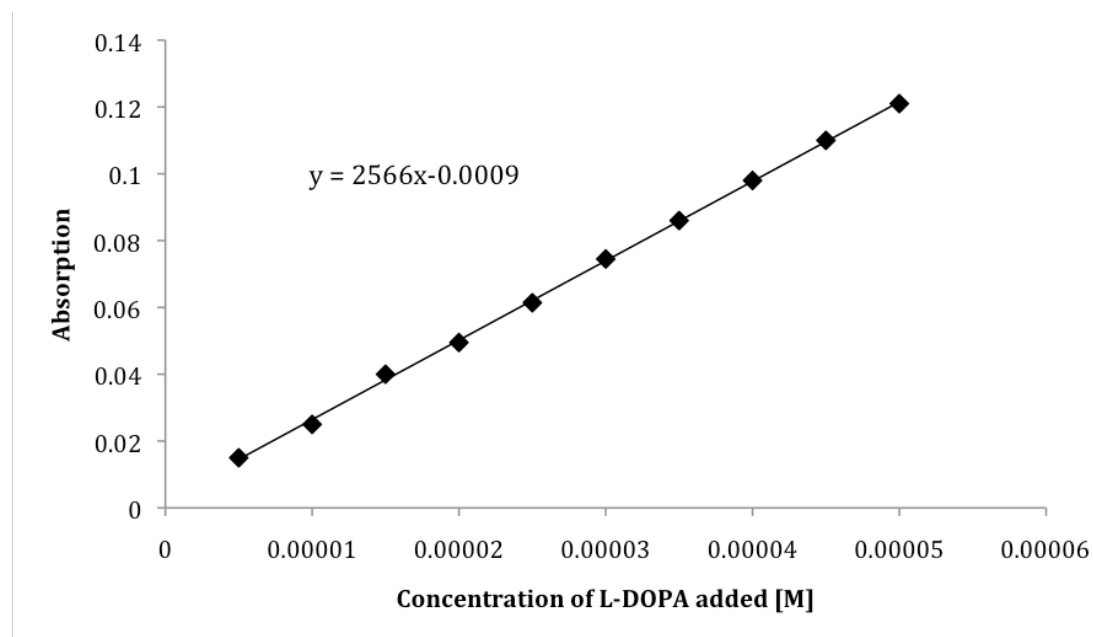


Figure 3.5 *L-DOPA's absorbance spectrum at 280nm by function of sample concentration. The linear fit of these values at 280 nm are used to calculate L-DOPA's molar extinction coefficient (ϵ).*

As with absorbance, fluorescence and fluorescence lifetimes, the molar extinction coefficient of each amino acid appears to be determined by the $-OH$ population of the fluorescent benzene ring. We see below in Table 3.4 that for an increasing number of $-OH$ groups, the molar extinction coefficient increases.

Amino Acid	Molar Extinction Coefficient ($M^{-1}cm^{-1}$)
Phenylalanine	195
Tyrosine	1405
L-DOPA	2566

Table 3.4 *Typical molar extinction coefficient values of two naturally occurring fluorescent amino acids (tyrosine, phenylalanine) and tyrosine's amino acid derivative, L-DOPA.*

3.4 L-DOPA Summary

Experiments carried out on L-DOPA to examine photophysical characteristics in comparison to other amino acids present in the body shows that, as is expected from their molecular structure, phenylalanine, tyrosine and L-DOPA have similar fluorescence responses, with changes in photophysics due to modifications of the phenyl group in the structures, the functional group responsible for their fluorescence. We observed that for additional –OH groups, both the absorbance spectra and the fluorescence emission spectra red-shifted. Conversely, the fluorescence lifetimes for each additional –OH group decreased.

Also, the molar extinction coefficient was recorded as a measure of each fluorophore's intrinsic inclination to absorb light. Again we observed a trend for increasing –OH groups on the fluorescent site, with molar extinction coefficients increasing and therefore each consequent amino acid having a higher propensity for photon absorbance.

Despite these results, more study is needed on L-DOPA to determine its role in the human body. For example, some studies suggest that L-DOPA and its derivatives has a potential toxicity in the human body^{76,77}

The continued study of L-DOPA is particularly of merit when considering its importance in producing both eumelanin and pheomelanin for the U.V. protection of the human body, and further as an effective treatment for Parkinson's disease. In fact, the latter's discovery as an effective agent in neuron signalling is so crucial that the Nobel Prize in 2000 for physiology or medicine was presented jointly to Professors Avid Carlsson, Paul Greengard and Erik Kandel for their discovery of its use in signal transduction in the nervous system.

4. Eumelanin Formation From L-DOPA

4.1 Introduction

The synthesis of melanin from L-DOPA encompasses two distinct synthetic routes, and thus produces two different forms of melanin that are dependant on synthetic stages and the presence of specific molecular species available during their formation. From its initial stage, L-DOPA is able to produce eumelanin, either enzymatically in the presence of tyrosinase, or at a slower rate in the presence of oxygen; or pheomelanin in the presence of the amino acid cysteine, biosynthesised and present in the human body. These melanins differ not only by colour – eumelanin is black and pheomelanin is brown – but also differ dramatically by structure, with eumelanin being primarily composed of 5,6-dihydroxyindole-2-carboxylic acid (DHICA) and dihydroxyindole (DHI) repeating units and pheomelanin composed of benzothiazane units.

Since the synthetic formation of melanins from L-DOPA were discovered and subsequently reported in various papers by Raper⁷⁸ and later Mason⁷⁹, the formation of eumelanin from L-DOPA has been widely characterised through various environmental conditions: increased pH⁸⁰, with the enzyme tyrosinase to catalyse the formation⁸¹, and with an increase in temperature⁸² just three of many variables in producing eumelanin from L-DOPA or tyrosine (as in Figure 3.1).

Despite this, some information is still missing about eumelanin's formation. Whilst a large number of intermediary groups in eumelanin's synthesis have had molecular characterisation, their photophysics and the role they play in eumelanin formation remains elusive.

Furthermore, basic characteristics of eumelanin still remain elusive, such as the mechanism for its role in skin protection and even its structure. Indeed, since Ito et al first characterised abundance of DHICA with respect to its non-carboxylated form

DHI in both synthetic and natural eumelanins in the mid 1980s⁸³, relatively little further information on its structure has been derived. The classical view states that eumelanin is likely an aggregation of predominantly these molecules, and this aggregation occurs via either of the 2, 3, 4 or 7 positions of the indole ring, as detailed below in Figure 4.1⁸⁴. However, this description of eumelanin fails to account for the presence of DHICA molecules in eumelanin, which are carboxylated in the 2 position.

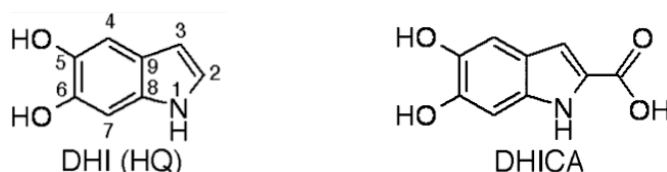


Figure 4.1 5,6-Dihydroxyindole and 5,6-Dihydroxyindole-2-carboxylic acid, key constituents in the formation of natural and synthetic eumelanins.

In this section we analyse two methods of non-enzymatic, synthetic eumelanin formation from L-DOPA that take around 48 hours in order to establish whether structural information can be obtained by observing photophysical properties.

We first observe the use of pH in the formation of melanin. Three different pH values – pH of approximately 2, 7 and 10 – and their effect on the formation of eumelanin from L-DOPA are examined. Included in this are the excitation spectra of eumelanin produced at pH 10 and the use of small volumes of copper as a catalyst for eumelanin formation.

Previous literature has shown that the formation of eumelanin from L-DOPA – the melanogenesis process – is catalysed both in-vivo and in-vitro by the presence of the enzyme tyrosinase; for example, its abundance effects colour in the formation of human hair⁸⁵. This may be used in the in-vitro melanogenesis process as described in §3, as the enzyme uses O₂ to provide oxidation of L-DOPA, thus allowing it to form dopaquinone as shown in §3 Figure 3.1.

Tyrosinase enzymes contain a proportion of copper⁸⁶, leading to the question of whether isolated copper itself may play a role in the enzymatic catalysis of eumelanin from L-DOPA.

Lastly, we observe the photophysical responses of a system where the pH was neutral at pH 7 but synthesis was catalysed by an increase in temperature to 37°C.

Graphs of absorbance changes over time are fitted to the Equation 4.1

$$A = B(1 - \exp(-kt)) \quad [4.1]$$

where B is a maxima of absorption and k measures the rate of reaction.

The half-life of rate of formation may then be calculated using the equation:

$$\tau = \frac{0.69}{k} \quad [4.2]$$

4.2 pH 10 Formation

4.2.1 pH 10 Formation Experimental

Eumelanin was produced from L-DOPA via the synthesis pathway shown in Figure 3.1. This was carried out by air bubbling of L-DOPA to increase the oxygen content of the solution, but with no enzyme present. Typically, some other environmental affect will be used alongside oxygen saturation to help increase the rate of eumelanin formation. Examined in this report, we use two methods: ammonia to increase pH to approximately 10, and an increase in temperature to approximately body temperature (37°C).

The first method involved the addition of ammonia to increase the pH. Powdered L-DOPA was dissolved in deionised water to a concentration of 1 mM. After the initial dilution, 1 mM ammonia was added to the sample to increase its pH to approximately 10. The pH was taken using pH 0-14 test paper (Sigma Aldrich, UK) and was measured to be approximately 10. The solution was stirred on a hotplate stirrer for 5

minutes after the addition of ammonia. The aqueous L-DOPA solution was then bubbled with air at a pump rate of 1.5 L/min. Activity in the sample was observed at around 0.5 hours after initial heating and air bubbling by a colour change from clear to light brown. After 48 hours, the sample became inky-black and lacked any transparency, an indication of eumelanin formation⁸⁷.

To further illustrate the dependence of eumelanin formation on both oxygen saturation and pH, both a neutral and a low pH sample were measured with only oxygen saturation. Samples were produced to 1 mM concentrations as before. After fully dissolving, one sample was kept at approximately pH 7, whilst 8 mM hydrochloric acid (Sigma Aldrich) was added to the second sample to reduce its pH to around 2. Both samples were bubbled with oxygen at a flow rate of 1.5 L/min. After 48 hours, the pH 7 sample had become slightly brown in colour, whilst the pH 2 sample had remained completely translucent.

To measure absorbance and fluorescence spectra of all above, samples were removed from the 1 mM stock solution and diluted to concentrations of 40 μ M to avoid saturation. All samples were measured using Starna 6Q 4 \times 1 \times 1 cuvettes (Starna Ltd).

When examining the role of copper in the production of eumelanin from L-DOPA, conditions were kept as similar to normal pH 10 formation as possible to form an accurate comparison. L-DOPA was dissolved in deionised water to a concentration of 1 mM from powdered form. From this, small volumes of 1 mM concentration solution were removed at time regions similar to that of pH 10 formations and diluted further in deionised water to a cuvette concentration of 40 μ M to avoid high-concentration effects such as self-absorption in the steady-state and time-resolved measurements.

Copper sulphate powder (Sigma Aldrich) was dissolved in deionised water to a concentration of 1 mM. After fully dissolving, a small volume was added to the L-DOPA such that its concentration was in a ratio of 1:10 with L-DOPA *i.e.* a concentration ratio of 0.1mM:1mM copper sulphate:L-DOPA and a concentration of 4 μ M:40 μ M in cuvette.

Afterwards, measurements were taken according to procedures carried out for pH 10 eumelanin formation in the absence copper, as above.

L-DOPA was purchased in its purest form from Sigma Aldrich.

4.2.2 pH 10 Formation Results

4.2.2.1 pH 10 Absorbance and Emission Spectra

Eumelanin synthesis from L-DOPA was recorded between 0 hours and 48 hours after initial induction of melanogenesis, as described above in §4.1. Typically, eumelanin is expected to form in a period of days after initial pH increase and oxygen saturation⁸⁰. This production of eumelanin is confirmed by both a brown/black colour visible in the cuvette⁸⁸ and an exponential absorbance spectrum with increasing absorbance towards U.V. wavelengths⁸⁹. This process is shown below in Figure 4.2 (—), where a broad absorbance spectrum is observed between 600nm and 230nm. This absorbance is not entirely unexpected from a biological view: as eumelanin works to control U.V. irradiation damage, it must be expected to absorb more light in the U.V. wavelengths than in the visible.

For shorter timescales (here shown between 0 hours and 24 hours), the absorbance spectrum is observed to peak in the U.V. regions at approximately 280nm. Thus, at $t = 0$ hours, we see that L-DOPA is still present in the sample. However, as time increases and preliminary L-DOPA molecules begin to move through the synthetic pathway, changes in the absorbance spectrum are observed for formation of different molecules (dopaquinone, dopachrome etc.), though some amount of L-DOPA is still observed in the sample at $t = 48$ hours and is given by a shoulder in the Eumelanin absorbance spectrum at around 280 nm. Initial absorbance is shown to increase to slightly longer wavelengths (around 290 nm), before again blue-shifting to slightly shorter wavelengths (around 270 nm) as eumelanin synthesises from L-DOPA.

Past literature⁹⁰ also highlights that the absorption process is coupled with a “safe” emission process in *Sepia officinalis* melanin: rather than absorbed light being dissipated in a radiative process which may cause harm to the body, eumelanin is reported to dissipate U.V. light in a safer non-radiative process, specifically through vibrational motions and thus heat dispersion⁹¹. Typically, a high U.V. wavelength absorption of a molecule will produce U.V. fluorescence with a small Stokes shift. This was not the case with eumelanin – excitation at 280nm produced no discernable fluorescence over a large wavelength region, consistent with literature which suggests that eumelanin’s quantum yield is around 9×10^{-4} at 280 nm excitation.⁹²

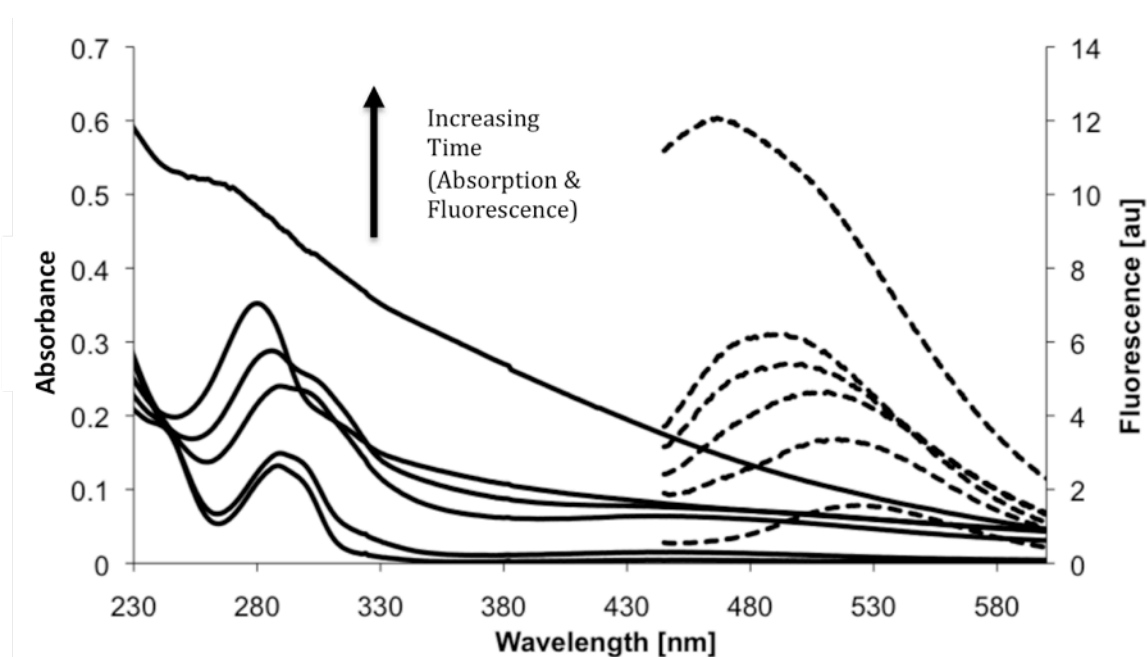


Figure 4.2 Absorbance (—) and fluorescence (---) spectra of 40 μ M pH 10 eumelanin formation from L-DOPA. Fluorescence spectra was excited at a wavelength of 375 nm. The spectra were recorded after 0.5, 1, 4, 6, 25, and 48 hours. Fluorescence units (au) signify arbitrary units.

On the other hand, melanin is known to have a high single-photon cross-section at longer visible wavelengths⁹³. By way of contrast, excitation at 375 nm was observed

to produce significant fluorescence emission with an initial peak at approximately 530nm (---). This is likely due to DHICA molecules, as recent studies suggest their excitation at this wavelength⁹⁴. However, generally an aggregation of a molecule into a larger form will result in a red-shift of the fluorescence spectra. This was not experimentally observed and conversely a blue-shift was observed from fluorescence emission data. This is likely due to the fact that rather than a homogeneous polymer, melanin is thought to be comprised of a highly heterogeneous combination of its different precursor molecule (including DHICA and DHI molecules⁹⁵), and thus excitation at 375 nm is observed to excited one or more of it's constituent molecules. The exact molecular structure of the molecule excited after 48 hours is unknown – as is the general structure of melanin – but we may assume from its fluorescence spectra that the molecular size of at least one of melanin's constituents is of a similar size to L-DOPA. It is observed from the fluorescence emission data that the full-width half-maximum (FWHM) of the fluorescence emission rises dramatically over time, indicating that there is high probability of multiple species being excited at this wavelength.

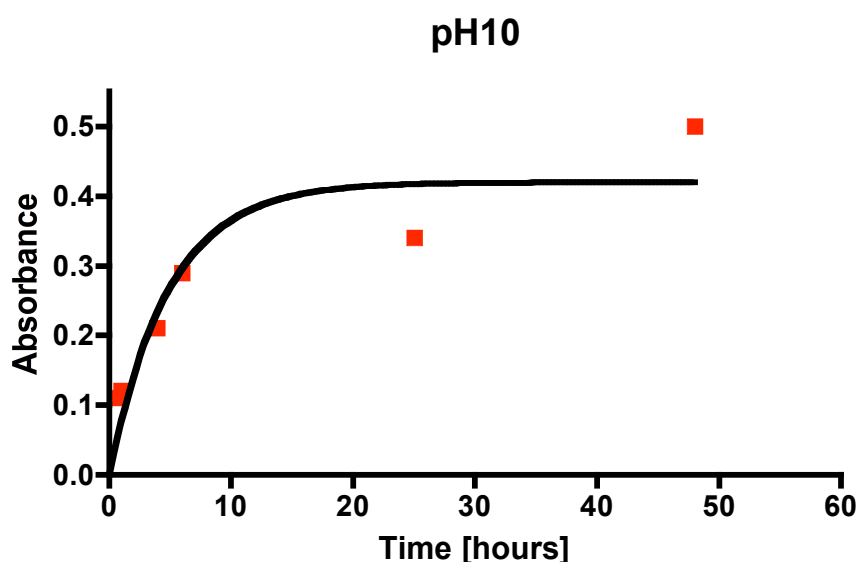


Figure 4.3 Change in absorbance at 280 nm over time in pH 10 eumelanin synthesis from L-DOPA.

The reaction kinetics of eumelanin formation in a high pH environment may also be studied by following the changes in the absorbance spectra at 280 nm with respect to time. This is shown above in Figure 4.3. Over a timescale of 0.5 hours until full eumelanin formation after 48 hours, the absorbance value is observed to rise approximately 0.4au, increasing to 0.5au from 0.1au. The half life τ for pH 10 melanogenesis as calculated from equation 4.2 produced a value of 3.39 ± 0.29 hours.

Converse to the formation of eumelanin from a high pH L-DOPA mixture, we have observed the absorbance and fluorescence of L-DOPA at pH 2 with the addition of hydrochloric acid, shown in Figure 4.4. The absorbance is observed to increase slightly over time, though the time scale of this figure is much longer than in Figure 4.2, with only a slight increase in the absorbance at 280nm occurring after approximately 240 hours compared to pH 10 L-DOPA's absorbance changes after 1-2 hours. This indicates that in low pH L-DOPA, the kinetics of eumelanin synthesis is dramatically slower and the formation of intermediary synthesis products, if indeed any formation is able to, occurs over a much longer timescale than at high pH values.

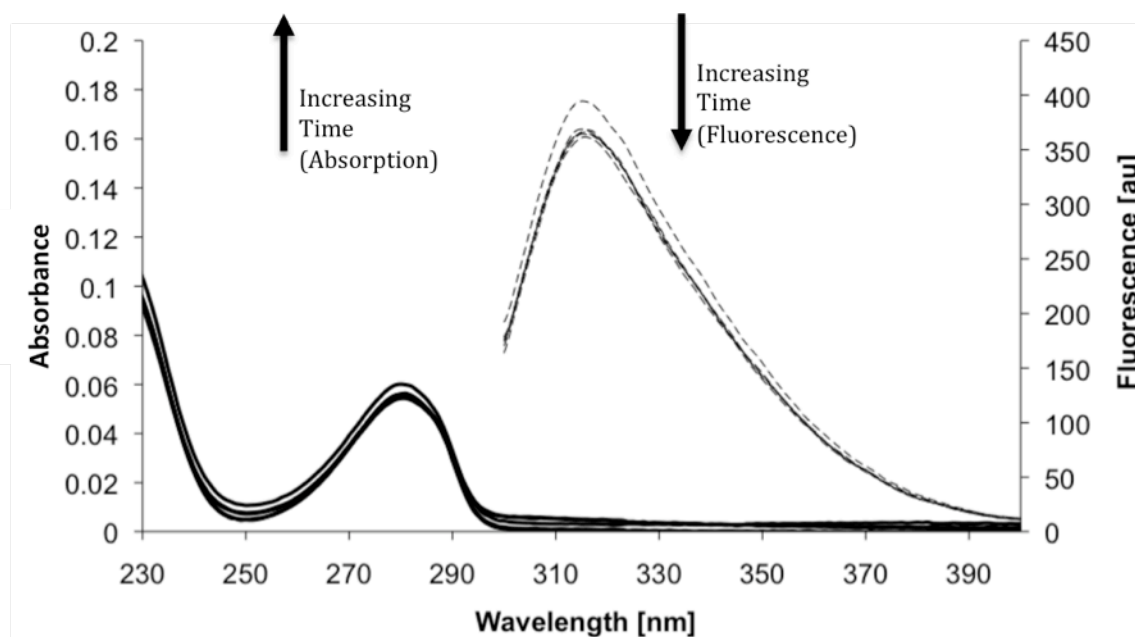


Figure 4.4 Absorbance (—) and fluorescence (---) spectra of 40 μ M pH 2 eumelanin formation from L-DOPA. Fluorescence spectra was excited at a wavelength of 280

nm. The spectra were recorded after 0.5, 1, 3, 5, 24, and 48 hours. Fluorescence units (au) signify arbitrary units.

The kinetics of synthesis of eumelanin from L-DOPA occurs at a significantly slower rate than in pH 10 eumelanin synthesis. This is shown below in Figure 4.5, illustrating the change in absorbance over time at 280 nm wavelengths. We see that the L-DOPA absorbs approximately 0.054au after a time of 0.5 hours, only increasing in absorbance to approximately 0.055au after 48 hours, indicating that the absorbance of L-DOPA after 48 hours remains approximately the same as after 0.5 hours.

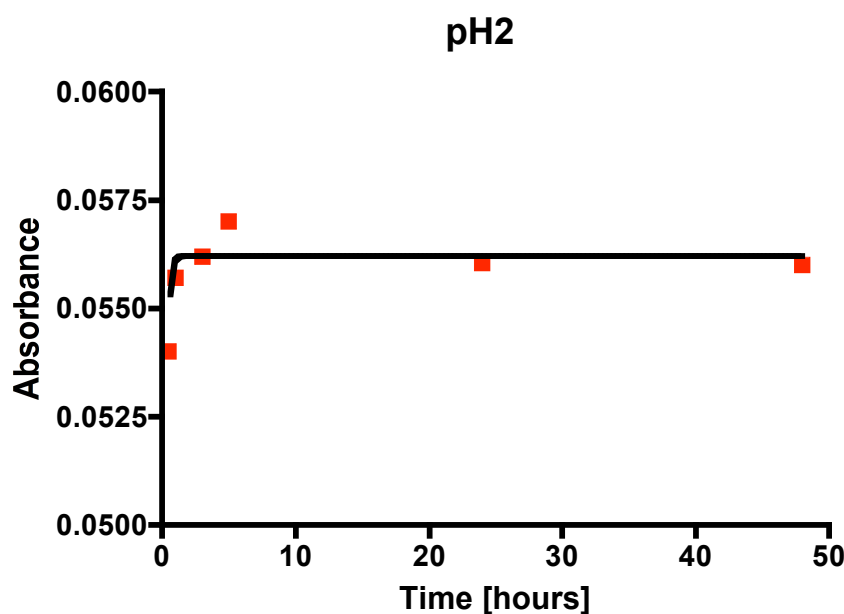


Figure 4.5 Change in absorbance at 280 nm over time in pH 2 eumelanin synthesis from L-DOPA.

As no significant amounts of eumelanin are produced during low pH synthesis, 375 nm wavelength excitation provided no discernable fluorescence and hence an excitation wavelength of 280 nm – the wavelength at which L-DOPA is generally excited – is shown to produce fluorescence peaking at around 315 nm. This is consistent with L-DOPA's emission wavelengths as given in §3.3.1. Conversely,

during pH 10 eumelanin production, 280 nm excitation was observed to decrease in fluorescence intensity over time whilst 375 nm excitation increased in fluorescence intensity over time. The half life τ of pH 2 formation was 0.107 ± 0.007 hours, indicating a significantly slower rate of formation than in pH 10 systems.

Lastly, we studied a neutral pH 7 system, also bubbled with air, to investigate the rate of formation compared to a pH 10 system and its ability to form melanin within a short timescale or follows the trend of the pH 2 system and was unable to form melanin within days. The absorbance and fluorescence response of an air-bubbled pH 7 sample is shown below in Figure 4.6.

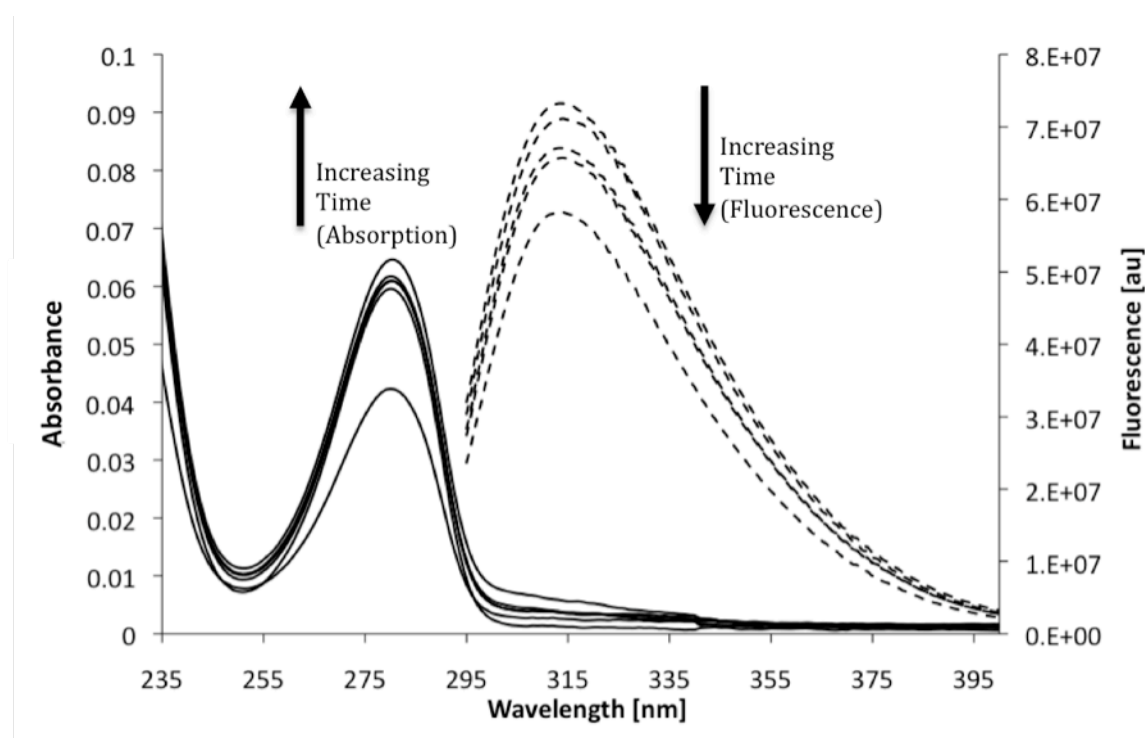


Figure 4.6 Absorbance (—) and fluorescence (---) spectra of $40 \mu\text{M}$ pH 7 eumelanin formation from L-DOPA. Fluorescence spectra was excited at a wavelength of 280 nm. The spectra were recorded after 0.5, 1, 4, 6, 25, and 48 hours. Fluorescence units (au) signify arbitrary units.

Similarly to pH 2 data, pH 7 air-bubbled L-DOPA is unable to form eumelanin within approximately 216 hours. Despite this, absorbance changes are more apparent than in the low pH system, with the absorbance at 280 nm rising more dramatically from around 0.04 au at time $t = 0$ to around 0.064 au around 48 hours. This increase in peak absorbance at 280 nm with respect to time is shown below in Figure 4.7.

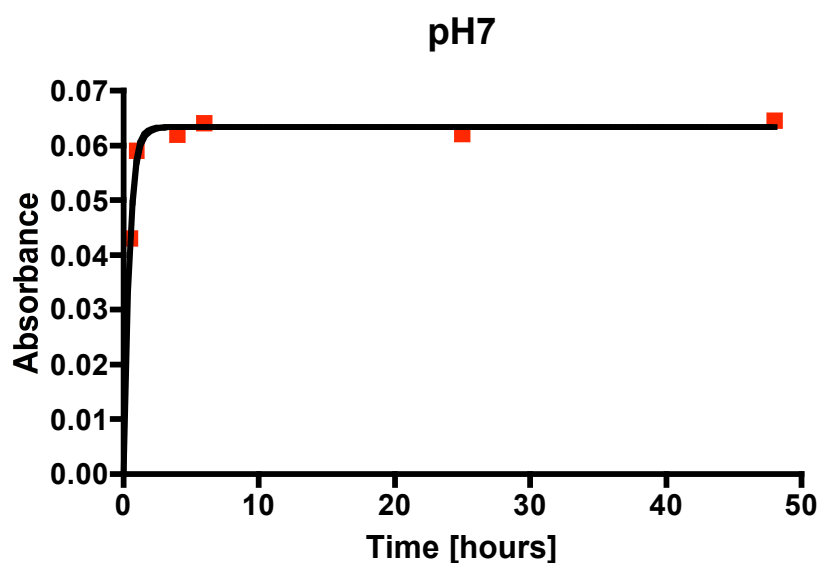


Figure 4.7 Absorption changes over time at 280 nm over time in pH 7 eumelanin synthesis from L-DOPA.

The half life τ of pH 7 formation was 0.293 ± 0.018 hours. This change in absorbance over time indicates that, despite being unable to form eumelanin within 216 hours, pH 7 L-DOPA is at a more advanced stage of eumelanin synthesis than in pH 2 L-DOPA.

4.2.2.2 pH 10 Eumelanin Excitation Spectra Results

The heterogeneity of eumelanin can be further studied by monitoring its excitation spectra after 48 hours. As shown below in Figure 4.8, for emission wavelengths 460nm to 600nm we observe that each has a unique excitation spectrum and thus assume that fluorescence at each emission wavelength may come from one or more different fluorophores.

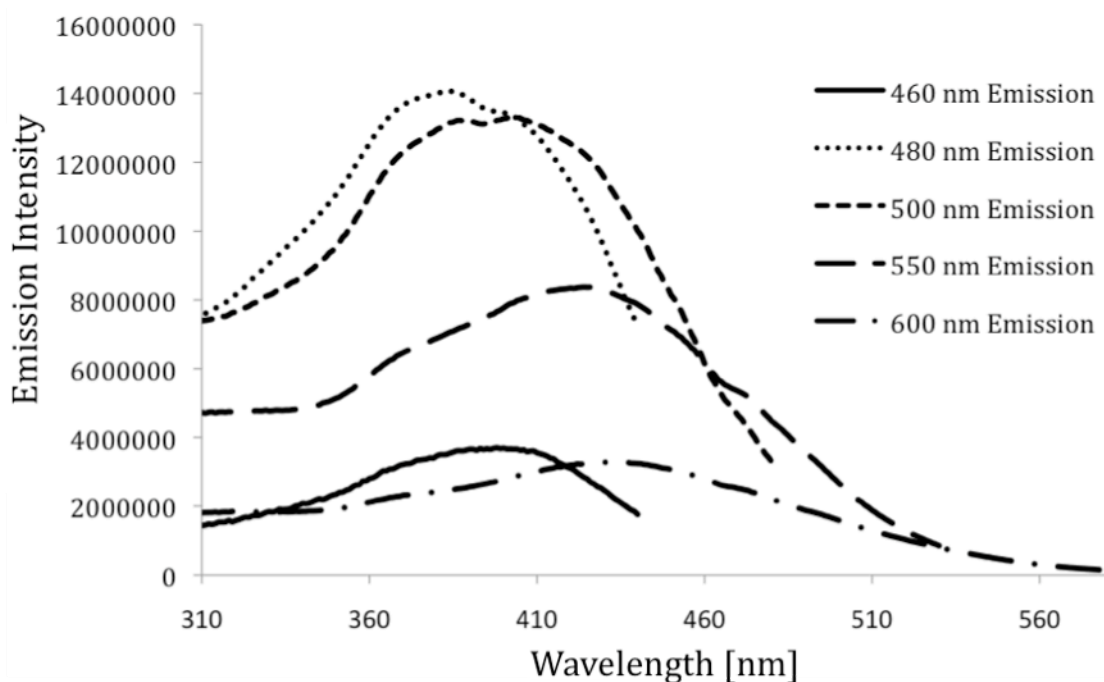


Figure 4.8 Combined excitation spectra of 40 μM pH 10 eumelanin after 48 hours showing emission wavelengths from 460 nm to 600 nm. Excitation at 375 nm may excite several discrete intermediaries of eumelanin. Excitation units (au) signify arbitrary units.

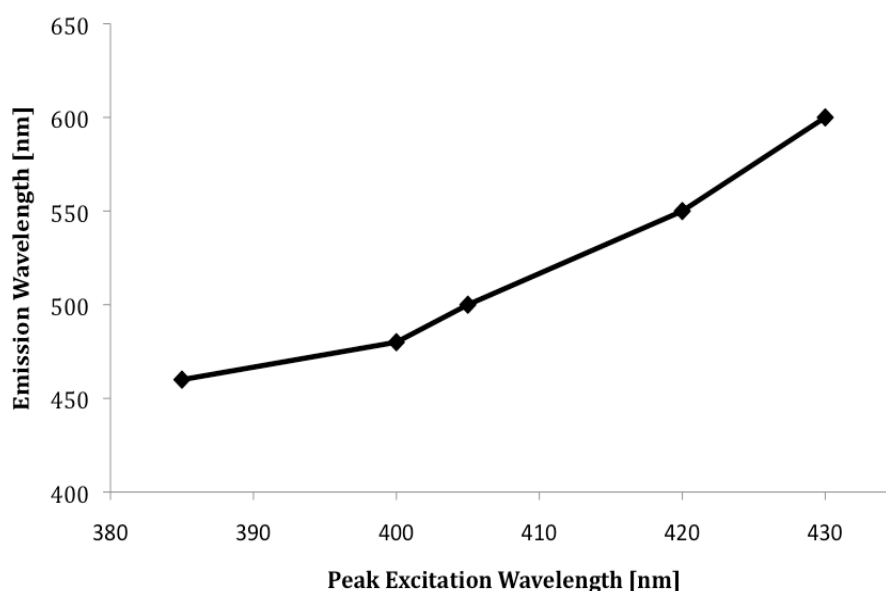


Figure 4.9 Changing emission wavelengths as a function of peak excitation in pH 10 eumelanin after 48 hours. Difference in emission wavelength for each excitation highlights the heterogeneity of eumelanin.

Figure 4.9 shows the change in peak excitation wavelength for each given emission spectra. From this, we see that there is a different fluorescence emission wavelength for each excitation wavelength, providing evidence for the presence of multiple species within the sample.

4.2.2.3 pH 10 Eumelanin Fluorescence Lifetime Results

Despite its low fluorescence quantum yield, single photon fluorescence of melanin is still possible, as shown in §4.2.2.1. Therefore, we may assume that a time-resolved fluorescence lifetime acquisition at similar excitation and emission wavelengths is possible.

Table 4.1 shows the fluorescence lifetimes of eumelanin formation from L-DOPA between 0 hours and 336 hours. The fluorescence lifetime of eumelanin formation after 0.5 hours was observed to be three-exponential, suggesting that L-DOPA had begun to move through synthetic molecular changes, as typically L-DOPA displays a mono-exponential decay (§3.3.1). A three-exponential decay model for eumelanin is well established⁹⁶.

Fluorescence decays fitted to two and three exponential components after 0.5h and 336h are shown below in Figure 4.10, highlighting a bad fit to two exponential components ($\chi^2 > 1.2$) and a good fit to three exponential components ($\chi^2 < 1.2$)

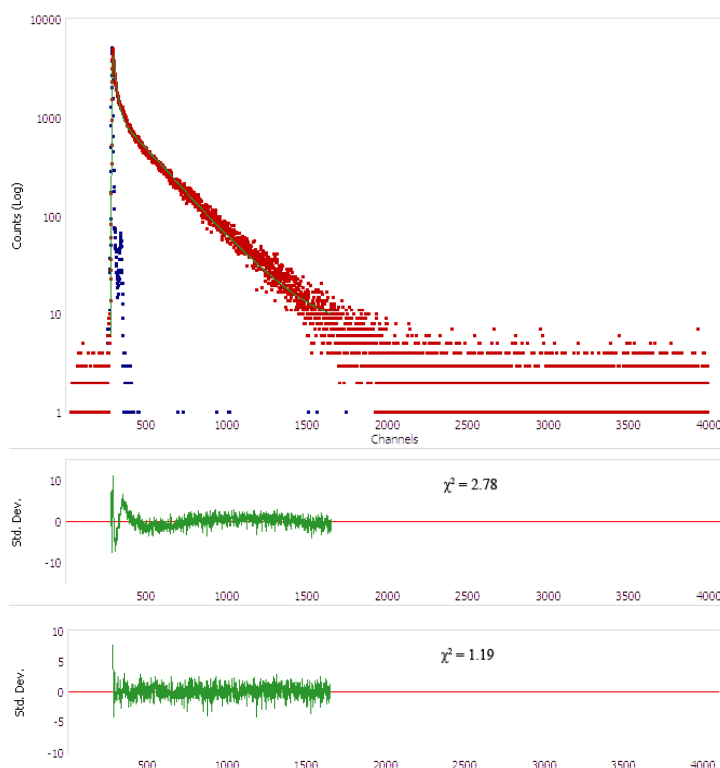
The lifetime component τ_1 (Figure 4.11a) is seen to decrease slightly in time whilst it's relative amplitude remains consistent at around 40% during hours 1-336, rising from 21% after 0.5 hours. Similarly, the lifetime of component τ_2 (Figure 4.11b) decreases though there is a more dramatic shortening of this component, falling from 8ns to around 4.8ns, followed by a recovery to around 7ns. This is also the case for

the third exponential component τ_3 (Figure 4.11c), which shows a drop from 0.22ns to 0.13ns at 48 hours, afterwards recovering to 0.19ns.

Time (hours)	τ_1 (ns)	α_1 (%)	τ_2 (ns)	α_2 (%)	τ_3 (ns)	α_3 (%)	χ^2
0.5	1.49 ± 0.10	22	7.94 ± 0.09	67	0.22 ± 0.01	11	1.19
1	1.41 ± 0.07	38	7.06 ± 0.16	40	0.14 ± 0.01	22	1.19
4	1.39 ± 0.08	40	5.93 ± 0.20	29	0.17 ± 0.01	31	1.11
6	1.31 ± 0.10	38	4.79 ± 0.17	30	0.18 ± 0.01	32	1.17
25	1.22 ± 0.10	33	4.81 ± 0.11	45	0.13 ± 0.01	22	1.19
48	1.73 ± 0.10	38	6.63 ± 0.16	42	0.19 ± 0.01	20	1.19
336	1.78 ± 0.10	39	6.8 ± 0.16	46	0.19 ± 0.01	15	1.18

Table 4.1 Fluorescence lifetime values for 40 μ M pH 10 eumelanin recorded between 0 and 336 hours. Lifetime decays are fit to a three-exponential model, with the χ^2 value indicating a good fitting regime (< 1.2) for all values.

(a)



(b)

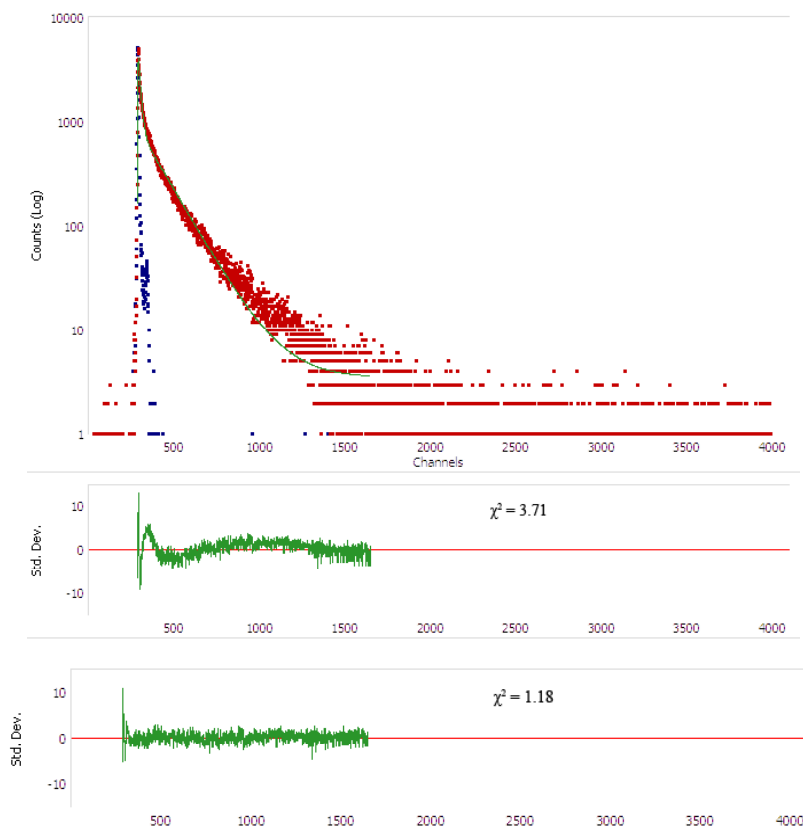


Figure 4.10 Fits of two and three exponential decay models of pH 10 eumelanin after (a) 0.5h and (b) 336 h

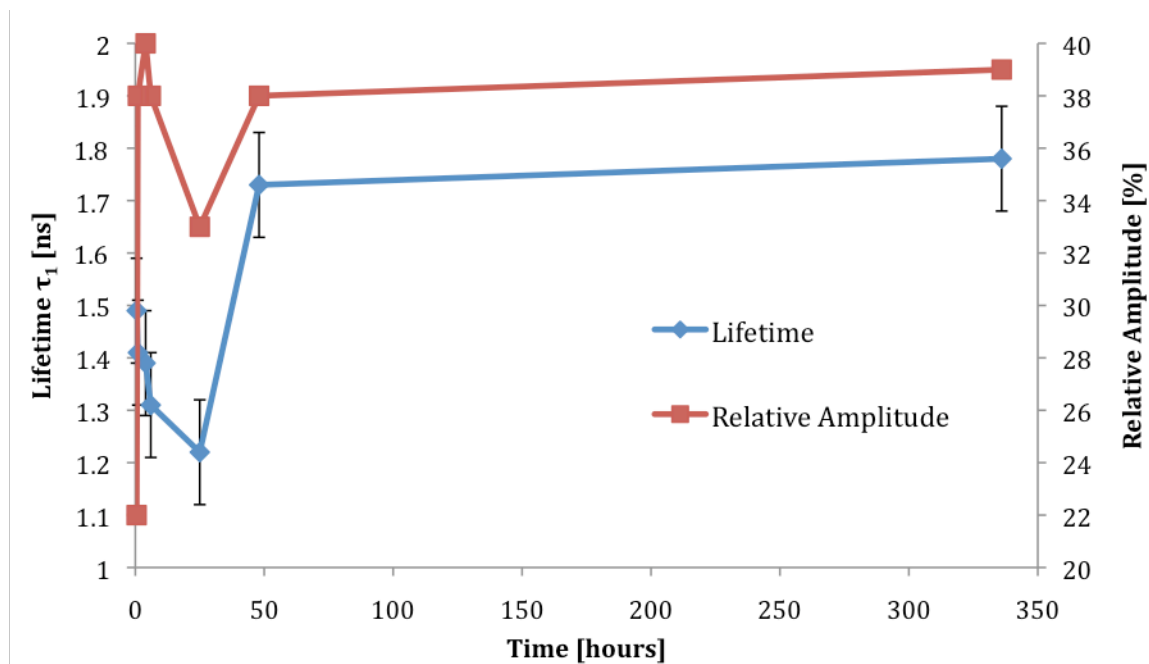


Figure 4.11a Fluorescence lifetime component τ_1 with corresponding relative amplitude component α_1 for 40 μM pH 10 eumelanin recorded between 0.5 and 336 hours.

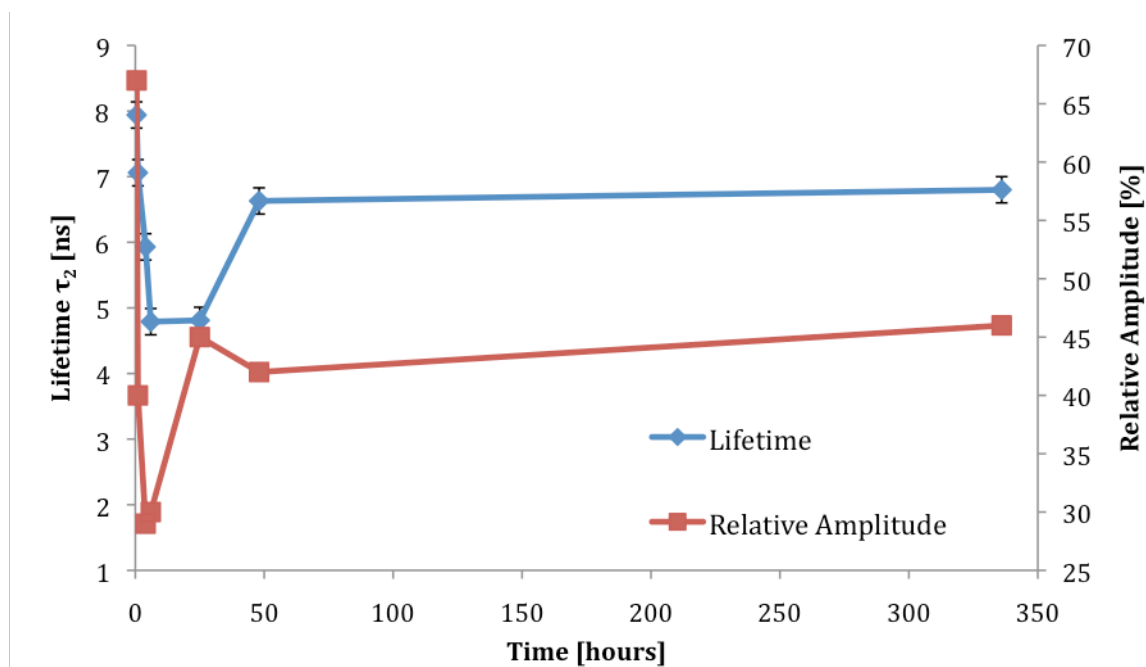


Figure 4.11b Fluorescence lifetime component τ_2 with corresponding relative amplitude component α_2 for 40 μM pH 10 eumelanin recorded between 0.5 and 336 hours.

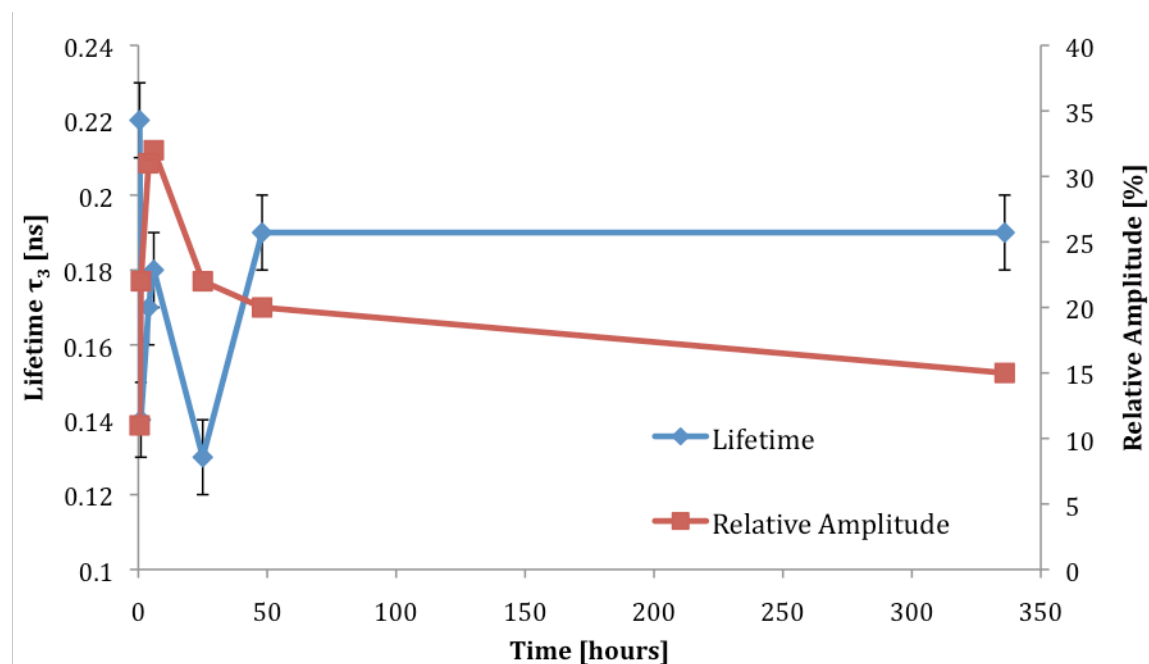


Figure 4.11c Fluorescence lifetime component τ_3 with corresponding relative amplitude component α_3 for 40 μM pH 10 eumelanin recorded between 0.5 and 336 hours.

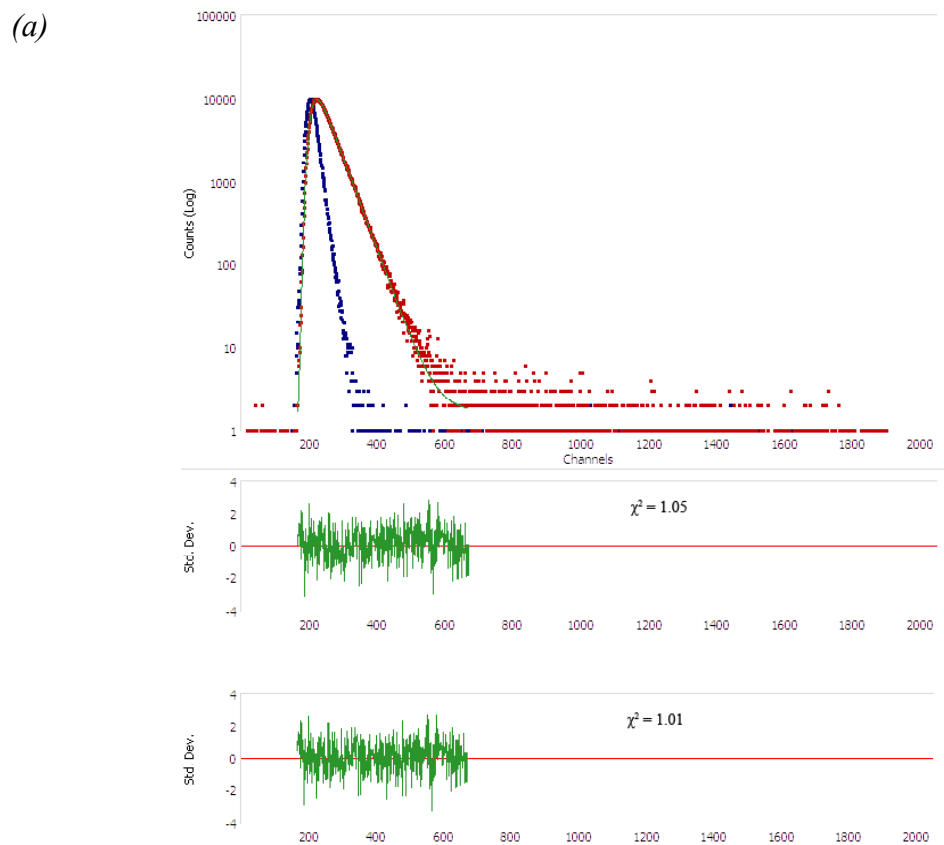
Fluorescence lifetimes recorded from pH 2 synthesis displayed a monoexponential lifetime around 1ns when excited at 280 nm for all time stages between 0.5 hours and 48 hours, again indicating that the sample was still predominantly comprised of L-DOPA. Fluorescence lifetimes recorded at neutral pH with only oxygen saturation also produced similar lifetimes, thus indicating that oxygen saturation alone is not enough to produce eumelanin synthesis over short timescales. The lifetimes of both these groups are shown below in Table 4.2

Time (hours)	τ_1 (ns)	α_1 (%)	χ^2
0.5	1.01	100	1.05
24	1.00	100	1.08
48	1.04	100	1.03

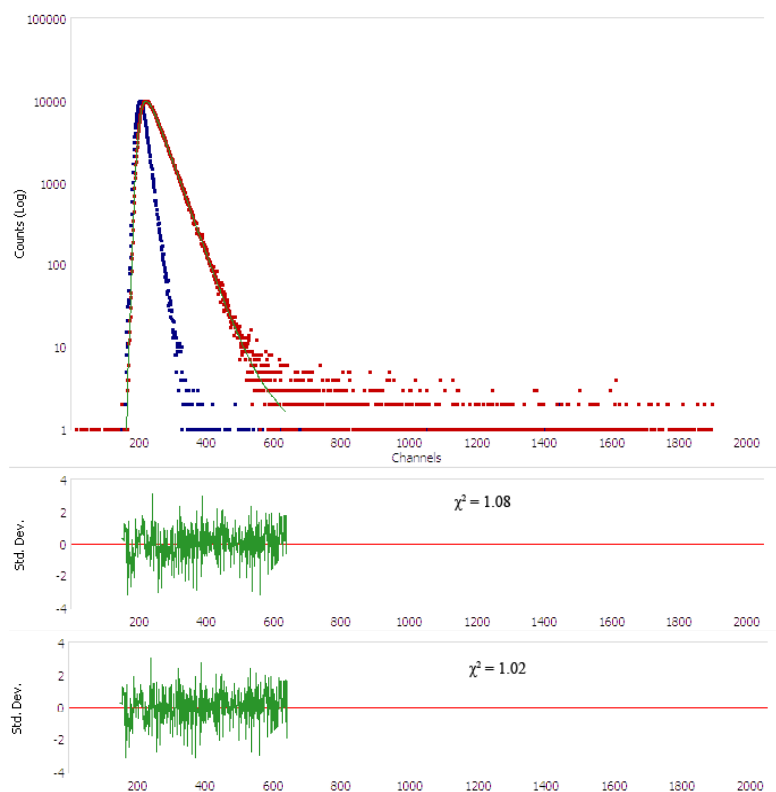
Time (hours)	τ_1 (ns)	α_1 (%)	χ^2
0.5	1.06	100	1.05
24	1.06	100	1.13
48	1.05	100	1.02

Table 4.2 Fluorescence lifetime values for 40 μ M pH 2 (top) and pH 7 (bottom) eumelanin recorded between 0 and 48 hours.

The fluorescence decays of L-DOPA at 0.5h, 24h and 48h is given below for pH 2 (Figure 4.12a,b,c) and pH 7 (Figure 4.13a,b,c), showing a good single-exponential fitting model ($\chi^2 < 1.2$).



(b)



(c)

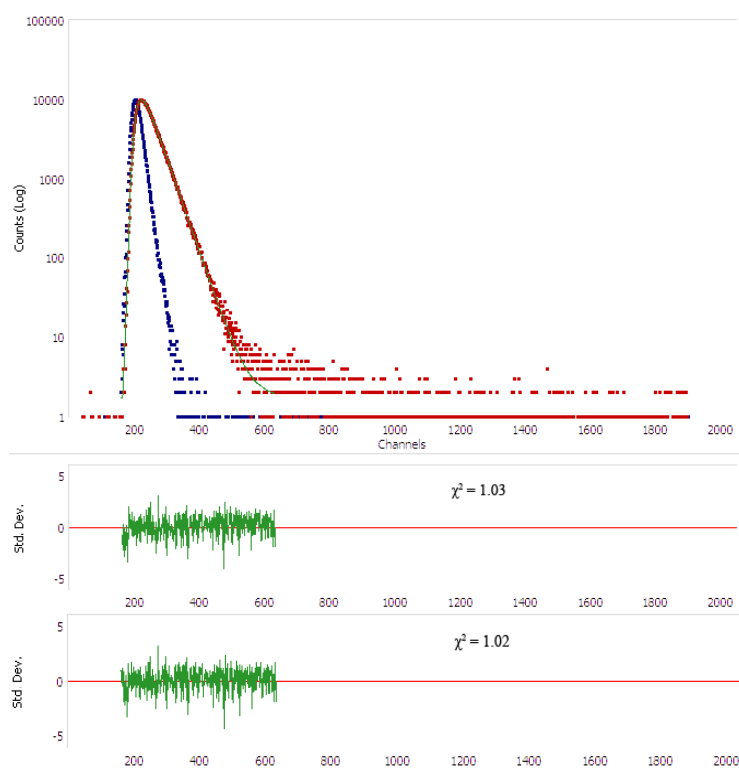
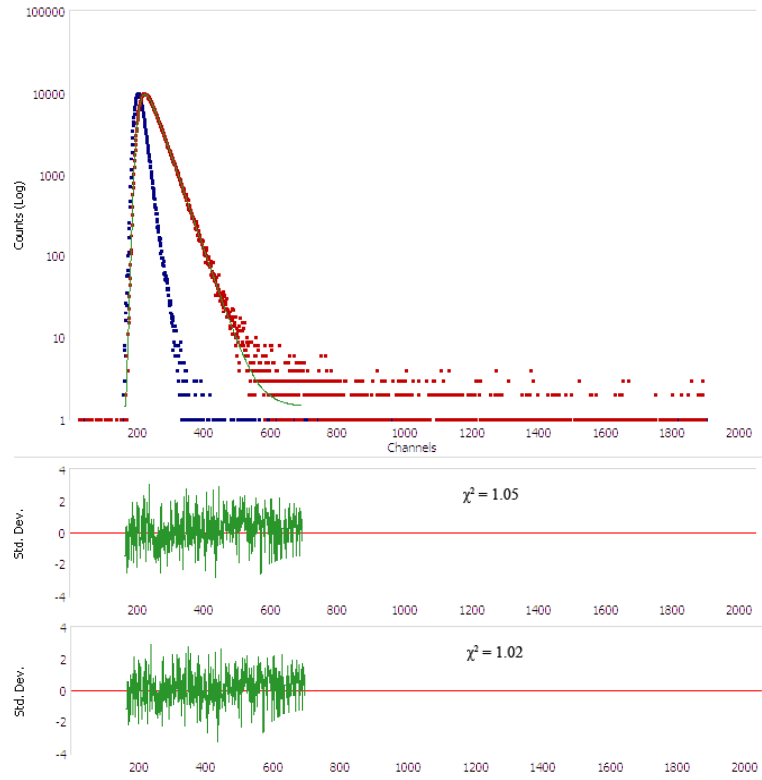
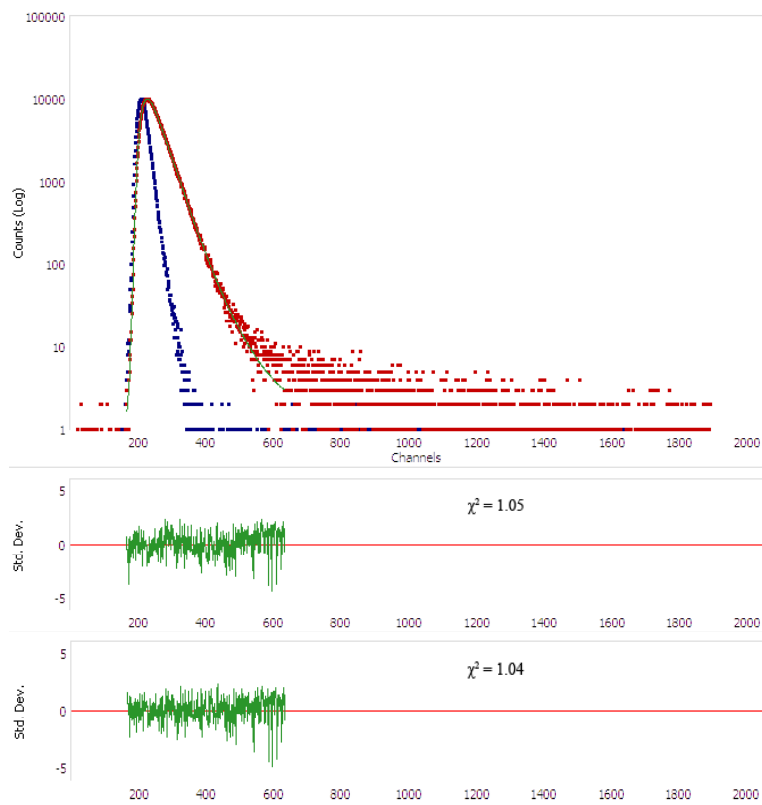


Figure 4.12 Fluorescence decays of pH 2 L-DOPA after (a) 0.5h, (b) 24h and (c) 48h fitted to one and two exponential decay models.

(a)



(b)



(c)

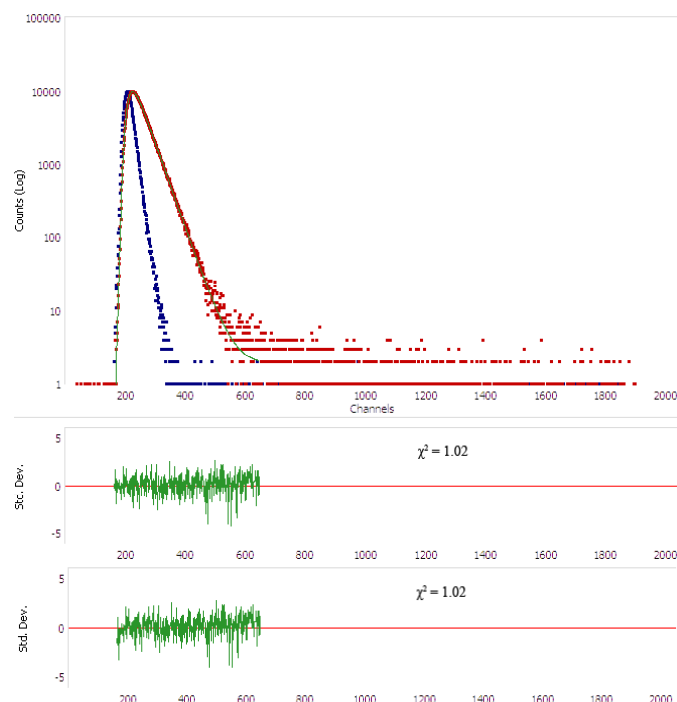


Figure 4.13 Fluorescence decays of pH 7 L-DOPA after (a) 0.5h, (b) 24h and (c) 48h fitted to one and two exponential decay models.

4.2.2.4 pH 10 Maximum Entropy Results

Maximum entropy analysis of eumelanin production allows us to analyse the fluorescence lifetime changes during melanin production using a different fitting procedure and thus potentially allowing more information to be taken from lifetime decays than in standard least-squares fittings. Figures 4.14a and 4.14b below show the progressive lifetime distribution changes as eumelanin forms from L-DOPA showing two distinct time regions where dramatic changes were observed – from 1 - 6 h and from 24 - 48 h.

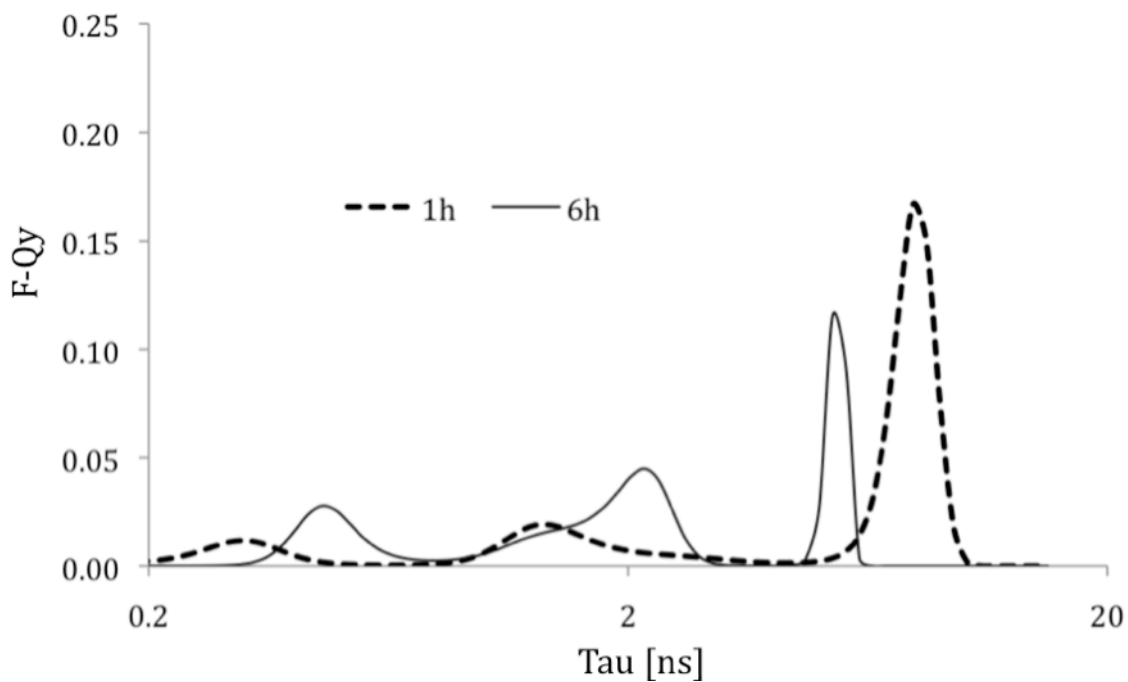


Figure 4.14a Fluorescence lifetime of 40 μ M pH 10 eumelanin between hours 1 and 6 of synthesis, fitted to a maximum entropy distribution showing contributions of lifetimes between 0.2 and 10ns.

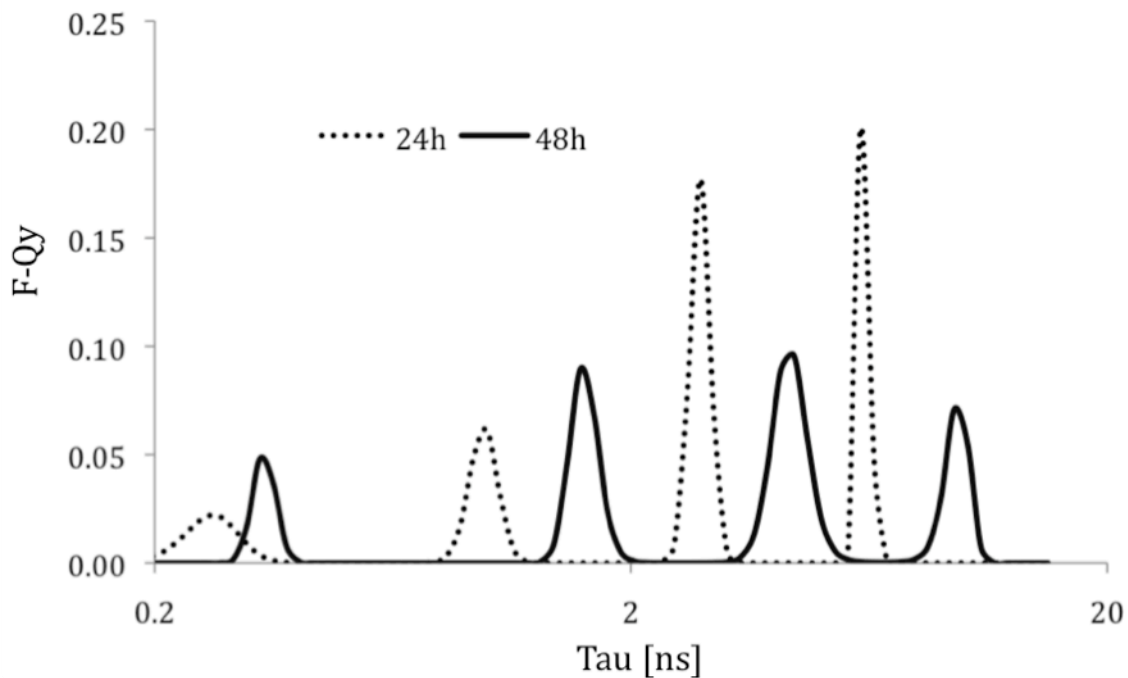


Figure 4.14b Fluorescence lifetime of 40 μ M pH 10 eumelanin between hours 24 and 48 of synthesis, fitted to a maximum entropy distribution showing contributions of lifetimes between 0.2 and 10ns.

The distributions initially begin with a three exponential decay component observed after one hour. The peak at around 8 ns shows a very narrow, defined peak indicating that an exponential model is adequate in fitting this lifetime component. However, the lifetime peaks present at approximately 1.2 ns and 0.3 ns are wider, with a larger full-width half-maximum (FWHM) indicating that an exponential model is less likely to fit these and that a large number of molecular species are contributing both decays. Furthermore, a shoulder is present at around 2.1 ns after 1 hour, indicating that the large FWHM from the 1.2 ns decay may be due to two discrete species contributing to the overall lifetime. In this case, a four-exponential decay may define the system better than the three-exponential system used in §4.2.2.3 Table 4.1. However, the chi-squared fitting function increases in likelihood of good fitting with increased number of exponential factors, and in practice most four-exponential systems would show an acceptable chi-sq value when fit to a three-exponential model. Conversely, this may explain the relatively high chi-squared values when using a three-exponential model to fit eumelanin.

The four-exponential model is further shown after 6h when the 2.1 ns shoulder first observed at 1h becomes the dominant peak in that region, increasing to a higher contribution than the 1.2ns component. The component at approximately 7.8 ns was observed after 1h to decrease dramatically, after 6h showing a lifetime of around 5.3 ns. The 0.3 ns component also increases after 6h to around 0.5ns.

This increase in number of exponential components over time likely corresponds to the complex heterogeneous chemical structure of eumelanin as observed in Figure 4.8. Likely these components comprise fluorescence lifetime responses of several distinct species within the eumelanin molecule.

4.2.2.5 pH 10 Copper Catalysed Eumelanin Results

The absorbance spectrum of L-DOPA solution containing copper sulphate is shown below in Figure 4.15, highlighting the change in the rate of production of eumelanin when copper is present during synthesis from L-DOPA. We observed that when copper sulphate was added to the sample at a ratio of $[\text{Cu}^{2+}] : [\text{L-DOPA}] = 1 : 10$, production of eumelanin from L-DOPA was increased dramatically. Typically, as seen in §4.2.2.1 Figure 4.2, complete eumelanin production is carried out within a period of 48 hours. However, with the addition of copper sulphate, a characteristic eumelanin absorbance spectrum was observed after a period of 24 hours, though the peak at 280 nm is more apparent, indicating the presence of higher concentrations of unprocessed L-DOPA than in other eumelanin forming processes in the absence of copper. Thus, L-DOPA in the presence of small concentrations of copper is able to form eumelanin at double the rate of eumelanin formation in its absence.

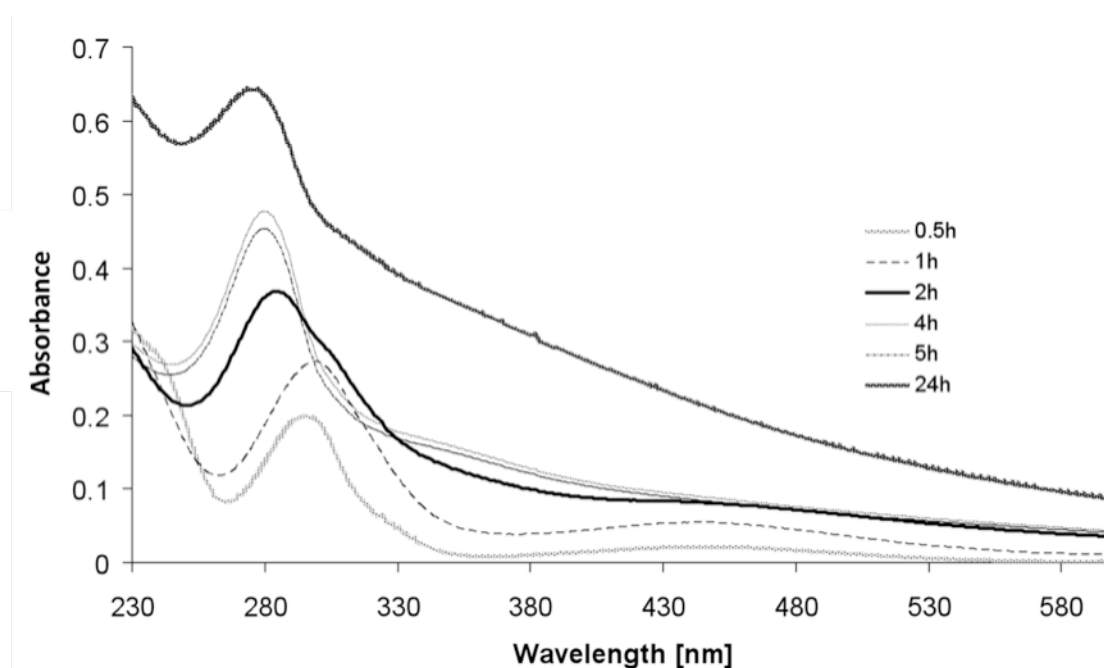


Figure 4.15 Absorbance spectra of 40 μM pH 10 eumelanin formation from L-DOPA containing 4 μM Copper sulphate. Spectra was recorded between 0.5 and 24 hours.

The fluorescence spectrum of copper-catalysed melanogenesis (Figure 4.16) is also similar to copper-free melanogenesis though, as with the copper-catalysed absorbance

spectrum, the fluorescence spectrum indicates melanin fluorescence after 24 hours. Furthermore, the final fluorescence is red-shifted with respect to its earlier precursors at 2, 4 and 5 hours, suggesting that some larger aggregate structure had formed by this stage. As with copper-free melanogenesis, the full-width half-maximum of the eumelanin produced after 24 hours is much larger than at 0.5 hours, indicating the likelihood of multiple fluorescent groups being produced over longer timescales.

The process behind the increase in rate of melanogenesis in the presence of copper ions is unknown, though some studies speculate that it is due to a complexation between copper and eumelanin⁹⁷. This may be the cause for the peak-wavelength variations in fluorescence spectra between pH 10 eumelanin and copper-catalysed eumelanin fluorescence.

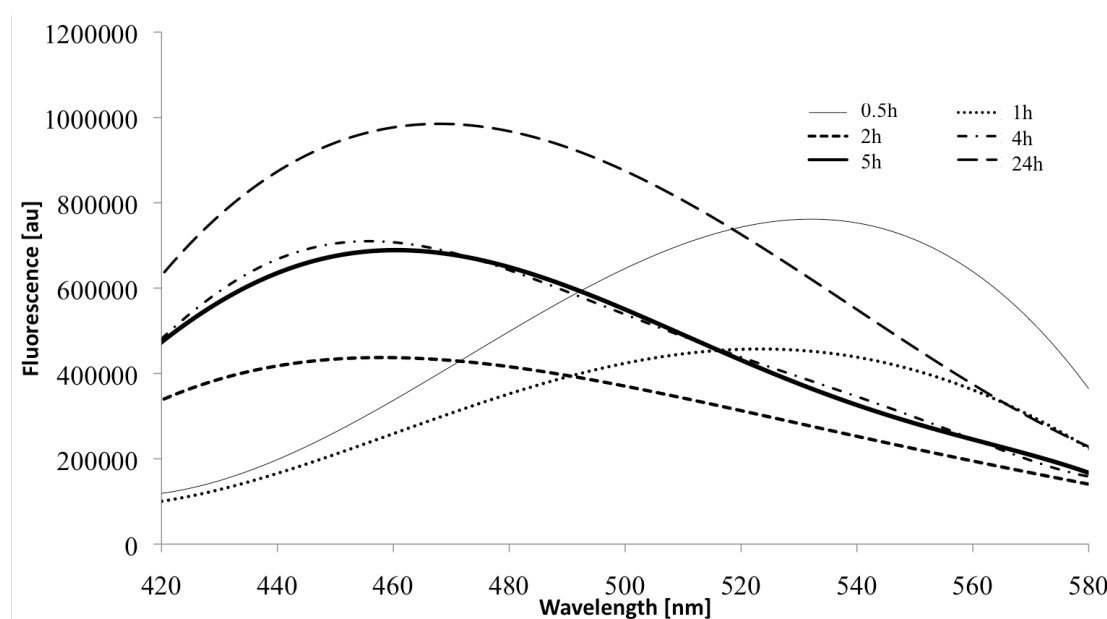


Figure 4.16 Fluorescence spectra of 40 μM pH 10 eumelanin formation from L-DOPA containing 4 μM Copper sulphate. Spectra was recorded between 0.5 and 24 hours.

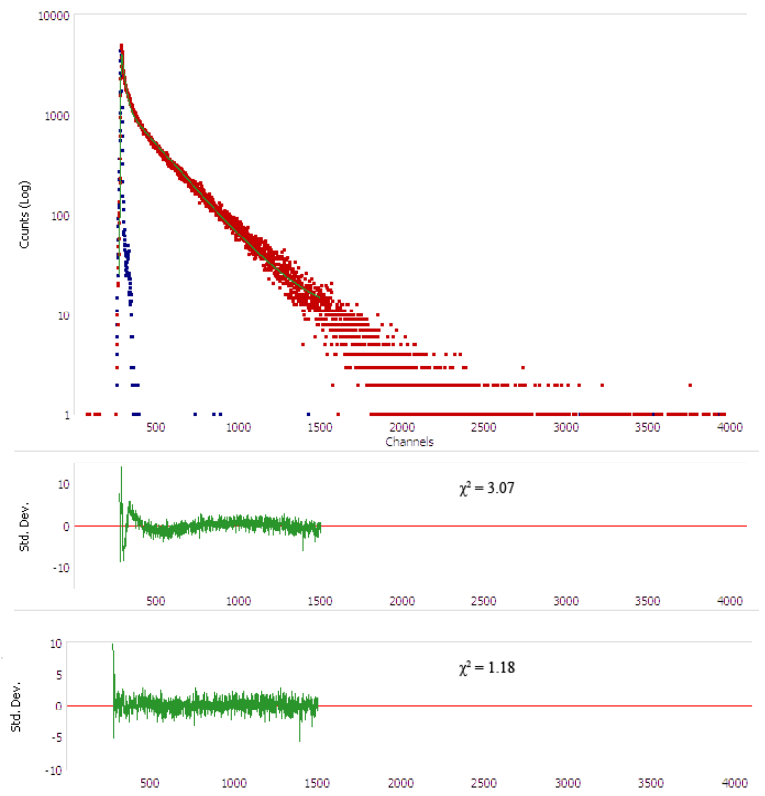
Fluorescence decays fitted to two and three exponential components after 0.5h and 24h are shown below in Figure 4.17, showing a inadequate fit to two exponential components ($\chi^2 > 1.2$) and a good fit to three exponential components ($\chi^2 < 1.2$).

As in the steady-state response of copper catalysed pH 10 eumelanin formation, the lifetime values remain similar but vary over shorter timescales, as shown below in Figures 4.18a-4.18c. As in the copper-free system, any morphological changes appear to occur on a short timescale. In both systems, the changes in lifetime constitute a large change in lifetimes in the first hours of synthesis, thereafter showing a “relaxation” response, with each lifetime then trending towards its initial value. These changes in lifetimes are also shown in Table 4.3.

Time (hrs)	τ_1 (ns)	α_1 (%)	τ_2 (ns)	α_2 (%)	τ_3 (ns)	α_3 (%)	χ^2
0.5	1.45±0.11	21	7.67 ± 0.18	70	0.25 ± 0.1	9	1.18
1	1.55±0.17	39	6.96 ± 0.10	49	0.12 ± 0.1	12	1.19
2	1.37±0.10	48	5.42 ± 0.09	28	0.1 ± 0.1	24	1.04
4	1.59±0.13	39	6.8 ± 0.12	45	0.13 ± 0.1	16	1.18
5	1.69±0.13	39	6.96 ± 0.11	46	0.15 ± 0.1	15	1.12
24	1.98±0.10	45	7.32 ± 0.18	42	0.25 ± 0.1	13	1.18

Table 4.3 Fluorescence lifetime values for 40 μ M pH 10 eumelanin containing 4 μ M copper sulphate, recorded between 0 and 336 hours. Lifetime decays are fit to three-exponential, with the χ^2 value indicating a good fitting regime (< 1.2).

(a)



(b)

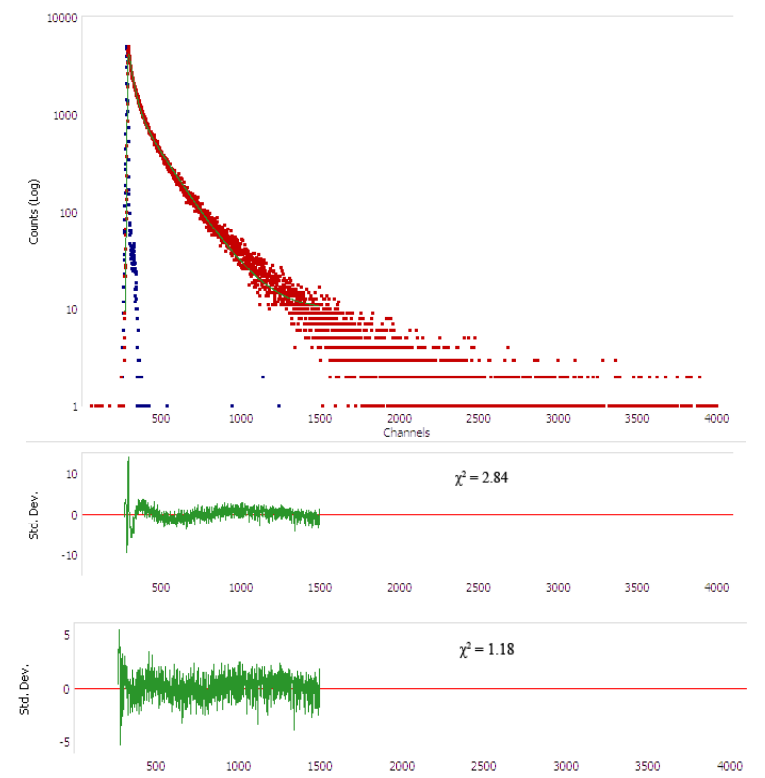


Figure 4.17 Fits of two and three exponential decay models of pH 10 eumelanin containing 4 μ M copper sulphate after (a) 0.5h and (b) 24 h

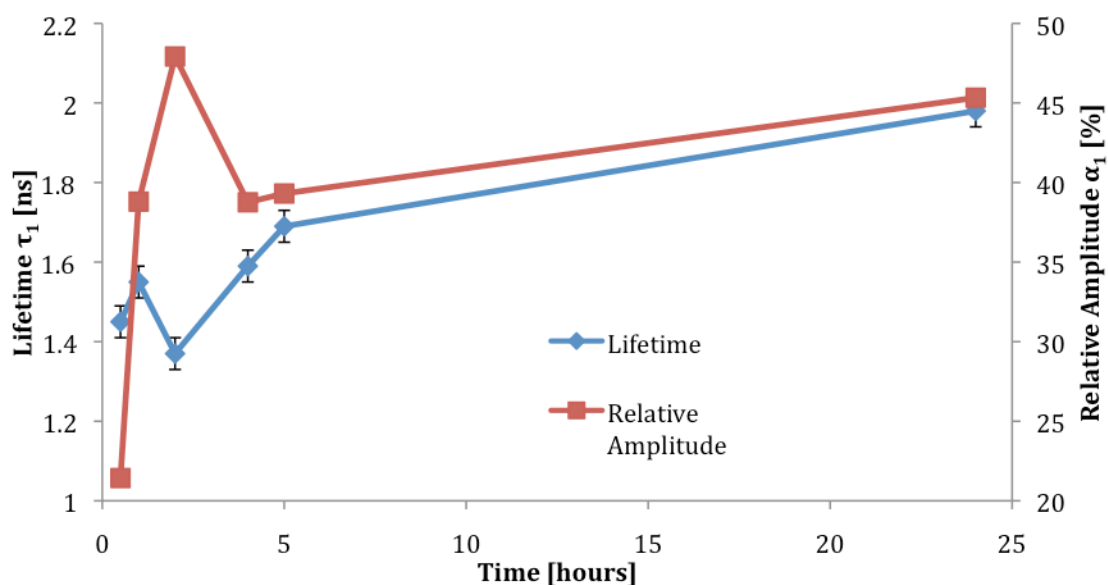


Figure 4.18a Fluorescence lifetime component τ_1 with corresponding relative amplitude component α_1 for 40 μ M pH 10 eumelanin with 4 μ M copper sulphate recorded between 0.5 and 24 hours.

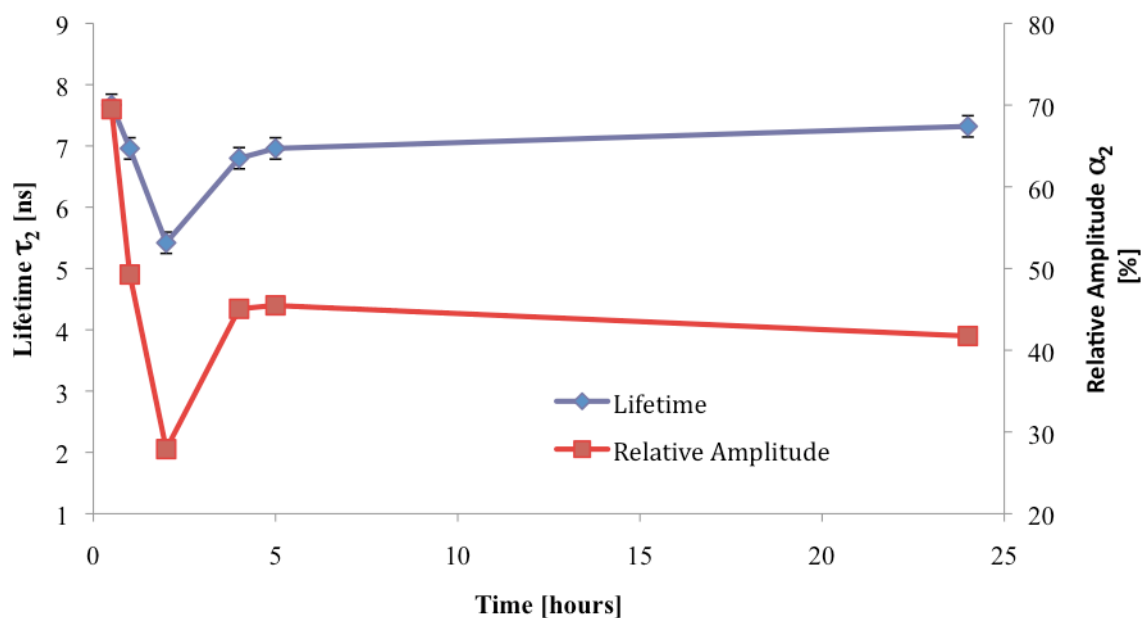


Figure 4.18b Fluorescence lifetime component τ_2 with corresponding relative amplitude component α_2 for 40 μ M pH 10 eumelanin with 4 μ M copper sulphate recorded between 0.5 and 24 hours.

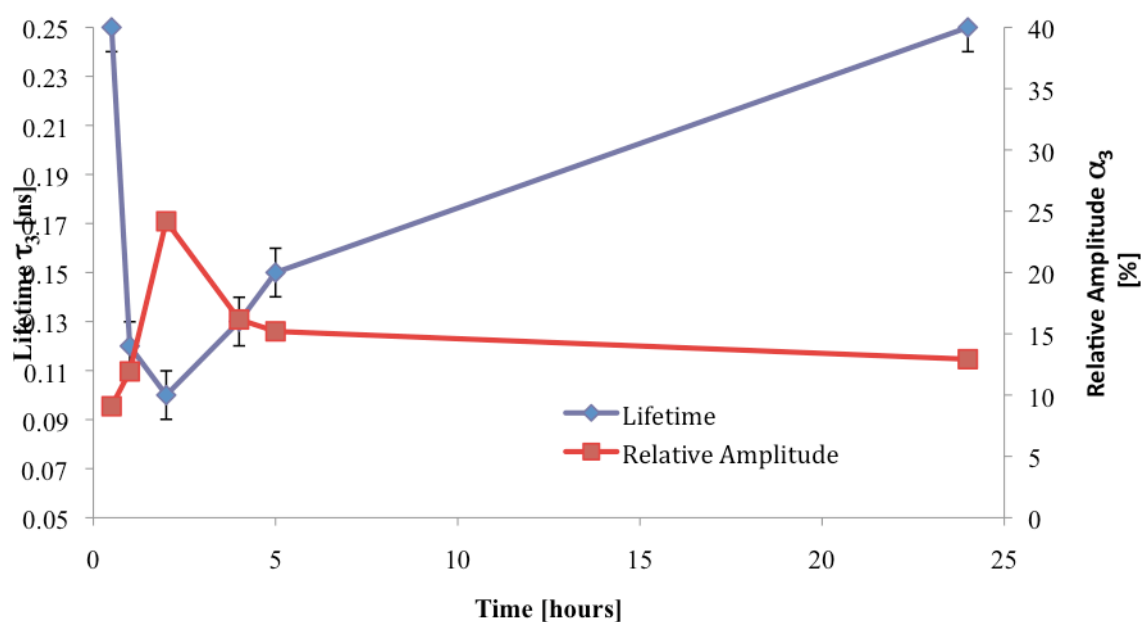


Figure 4.18c Fluorescence lifetime component τ_3 with corresponding relative amplitude component α_3 for 40 μM pH 10 eumelanin with 4 μM copper sulphate recorded between 0.5 and 24 hours.

4.3 High Temperature Neutral pH Formation of Eumelanin

As shown in §4.2.2.1, the rate of formation of eumelanin from L-DOPA progresses slowly at neutral and low pH values. However, presented below is a method of formation of eumelanin at neutral pH values with an increase in temperature to approximately body temperature – 37°C – a temperature often used to help catalyse its formation.⁸³

The synthesis of eumelanin has previously reported a variation in response for changes in pH values⁹⁸, and hence a neutral pH formation provides a valuable comparative system to pH 10 formations. Here we examine both the steady-state absorbance and emission spectra along with time-resolved lifetime values of such a system.

4.3.1 High Temperature Neutral pH Formation Experimental

The second method of formation of eumelanin from L-DOPA involved the production of a neutral pH eumelanin with increased temperature. Powdered L-DOPA was dissolved in deionised water to a concentration of 1 mM. After this initial dissolve, the aqueous L-DOPA solution was bubbled with air at a pump rate of 1.5 L/min. Simultaneous to this, the aqueous L-DOPA was held in a water bath that was maintained at an average temperature of approximately 37.2°C. As was the case in high pH samples, eumelanin production was indicated after 48 hours by a colour change to ink-black.

4.3.2 High Temperature Eumelanin Melanogenesis Results

4.3.2.1 High Temperature Absorbance, Fluorescence and Lifetime

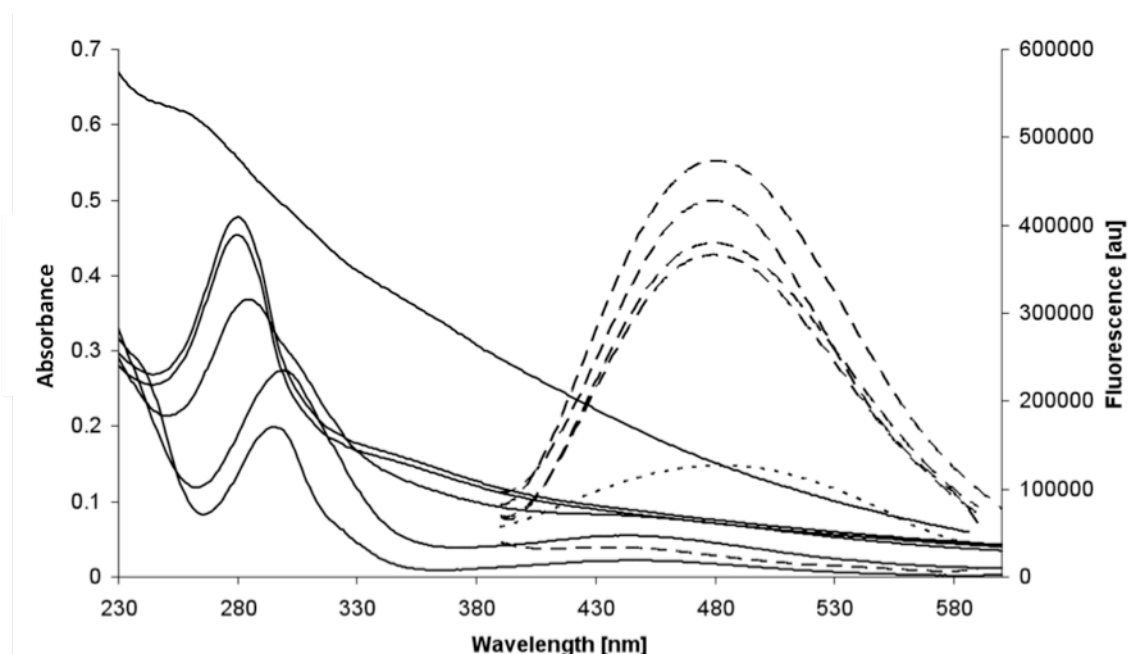


Figure 4.19 Absorbance (—) and fluorescence (---) spectra of 40 μM pH 7 eumelanin formation from L-DOPA, heated to 37°C. Fluorescence spectra was excited at a wavelength of 375 nm. The spectra were recorded after 0.5, 1, 3, 5, 26, and 48 hours.

Fluorescence and absorbance spectra for eumelanin heated to 37°C and bubbled with air for 48 hours are shown above in Figure 4.19 . Whilst initially high temperature pH 7 and basic pH 10 spectra appear similar, there are differences in both. Despite moving through the same synthetic pathway, the absorbance spectra preceding the eumelanin peak observed after 48 hours appears different in both, with peaks apparent at different wavelengths. This is likely due to changes absorbance measurement times causing different absorbance spectra due to differing intermediary species in the formation of eumelanin. Despite this, the absorbance spectra remains similar to the pH 10 sample after 48 hours, with eumelanin's typically exponentially rising absorbance as light nears the U.V. wavelengths.

As in the pH 10 experimentation, excitation under 280 nm at the time of the first measurement (0.5 hours) produced no discernable fluorescence. However, fluorescence emission was detected after 0.5 hours during excitation at 375 nm, whose fluorescence emission upon subsequent excitations between 1 hour and 48 hours increased in intensity. However, contrary to pH 10 results, fluorescence emission did not blue shift, instead retaining a fluorescence emission peak at around 480 nm during the course of all experiments. This suggests that despite similar absorbance spectra, the species produced in pH 10 and increased temperature experiments may differ in morphology or indeed molecular structure, and suggests that at pH 7, the species are better defined and more stable.

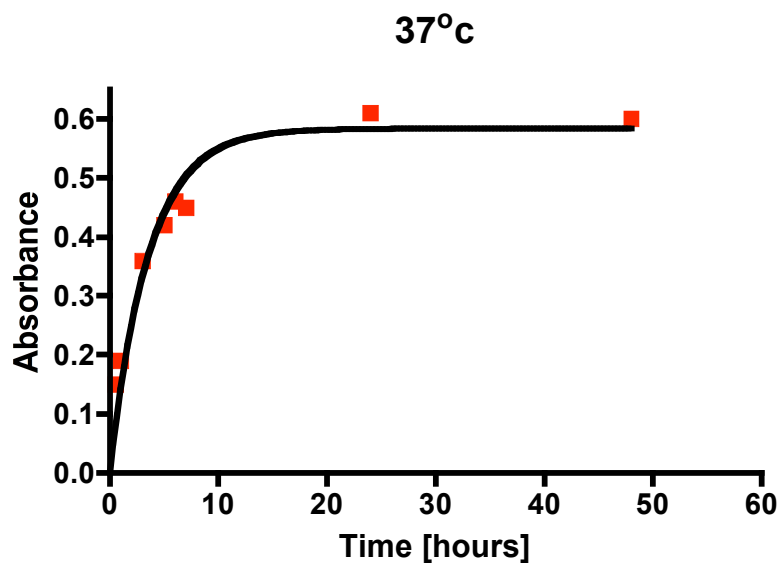


Figure 4.20 Absorbance changes over time at 280 nm excitation in pH 7 eumelanin synthesis from L-DOPA, heated to 37°C

Despite the potential morphological differences between samples, the rate of formation of melanin in high temperature neutral solutions appears similar to the rate of formation in high pH measurements at room temperature. The rate of change of absorbance at 280 nm in pH 7 systems heated to 37°C is shown in Figure 4.20 and analysed using equation 4.2. The half life τ of 37°C formation was found to be 2.43 ± 0.33 hours, and thus eumelanin forms at rates similar to pH 10 formations.

Fluorescence decays fitted to two and three exponential components after 0.5h and 350h are shown below in Figure 4.21, showing an inadequate fit to two exponential components ($\chi^2 > 1.2$) and a good fit to three exponential components ($\chi^2 < 1.2$).

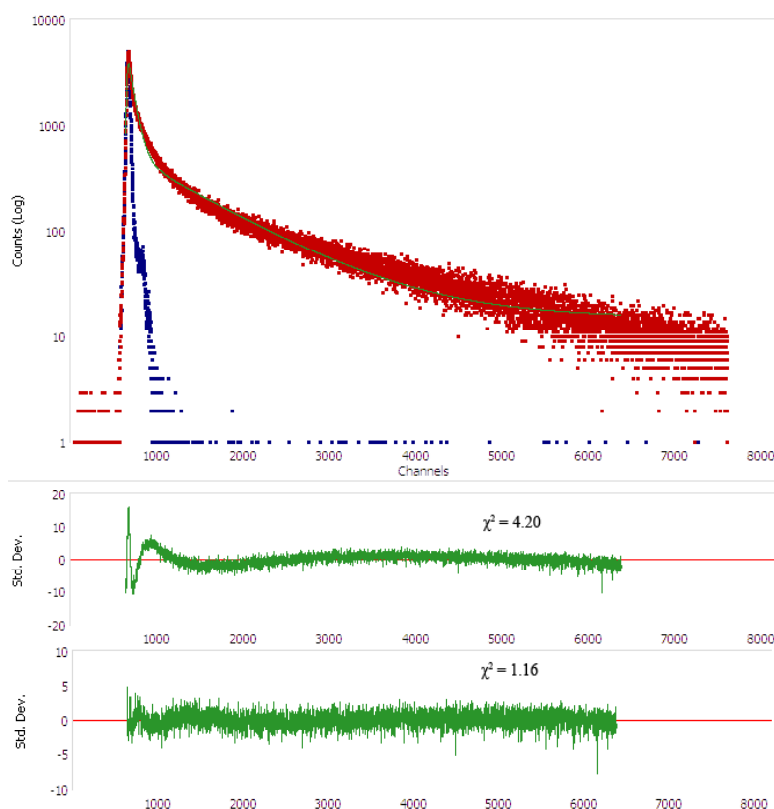
Lifetimes of eumelanin production during high temperature synthesis are shown in Table 4.4 and Figures 4.22a-4.22c. Lifetimes shown are markedly different from high pH formation, especially apparent in the longest lifetime component. Typically for high pH formation, lifetimes occurred at around 7-8 ns initially. In high temperature formations, lifetimes began at larger values, over 9 ns, but converged to similar values as high pH samples with time, indicating some lifetime differences in both formations. This means that different morphologies and structures in both samples

are likely leading to changes in lifetimes, though the remaining components show similar values in both.

Time (hrs)	τ_1 (ns)	α_1 (%)	τ_2 (ns)	α_2 (%)	τ_3 (ns)	α_3 (%)	χ^2
0.5	1.19 ± 0.10	33	8.32 ± 0.20	44	0.24 ± 0.1	23	1.16
1	1.26 ± 0.12	34	9.32 ± 0.15	47	0.25 ± 0.1	19	1.17
3	1.45 ± 0.12	37	8.47 ± 0.15	43	0.21 ± 0.1	20	1.16
5	1.44 ± 0.11	32	8.74 ± 0.17	46	0.2 ± 0.1	22	1.18
24	1.37 ± 0.18	19	6.49 ± 0.15	55	0.19 ± 0.1	26	1.2
26	1.28 ± 0.10	21	6.4 ± 0.14	55	0.19 ± 0.1	24	1.20
48	1.2 ± 0.19	20	6.27 ± 0.18	54	0.18 ± 0.1	26	1.18
350	1.18 ± 0.19	21	6.19 ± 0.19	53	0.18 ± 0.1	26	1.18

Table 4.4 Fluorescence lifetime values for 40 μM pH 7 eumelanin heated to 37°C recorded between 0.5 and 350 hours. Lifetime decays are fit to three-exponential, with the χ^2 value indicating a good fitting regime (< 1.2).

(a)



(b)

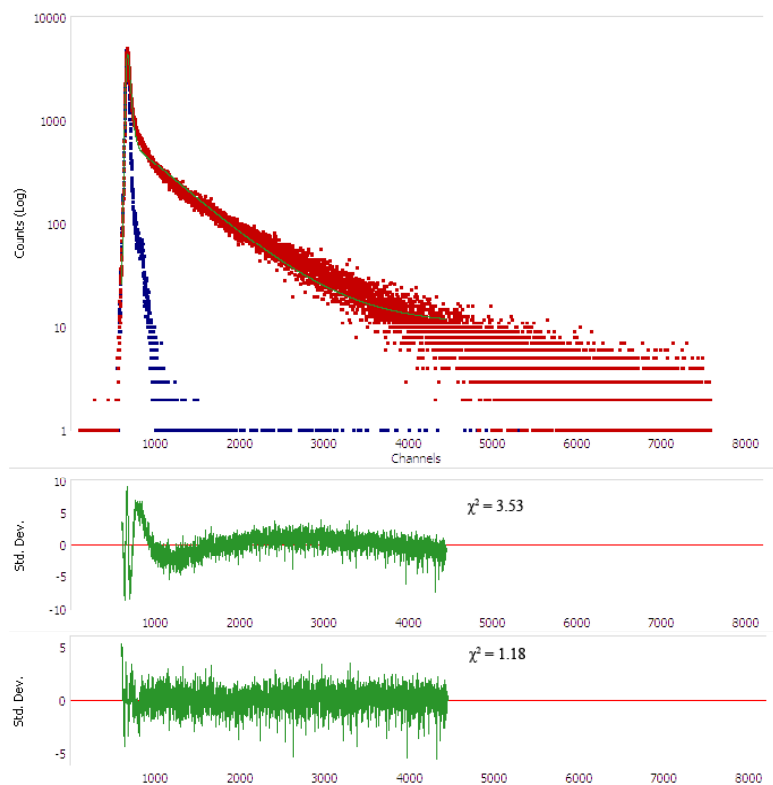


Figure 4.21 Fits of two and three exponential decay models of pH 7 eumelanin heated to 37°C after (a) 0.5h and (b) 350 h

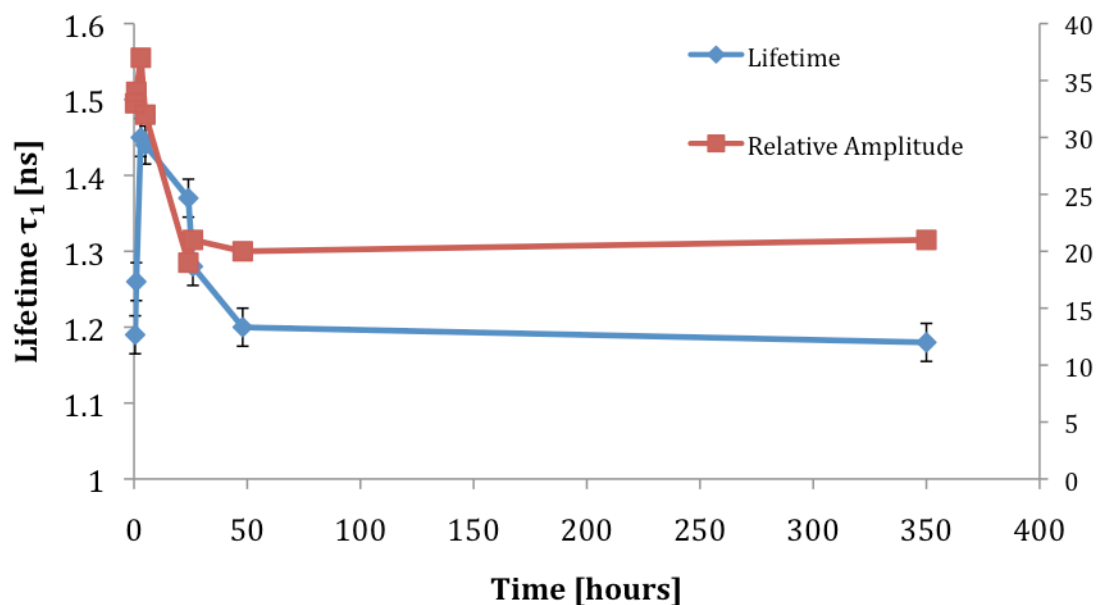


Figure 4.22a Fluorescence lifetime component τ_1 with corresponding relative amplitude component α_1 for 40 μM pH 10 eumelanin, heated to 37°C. Values were recorded between 0.5 and 350 hours.

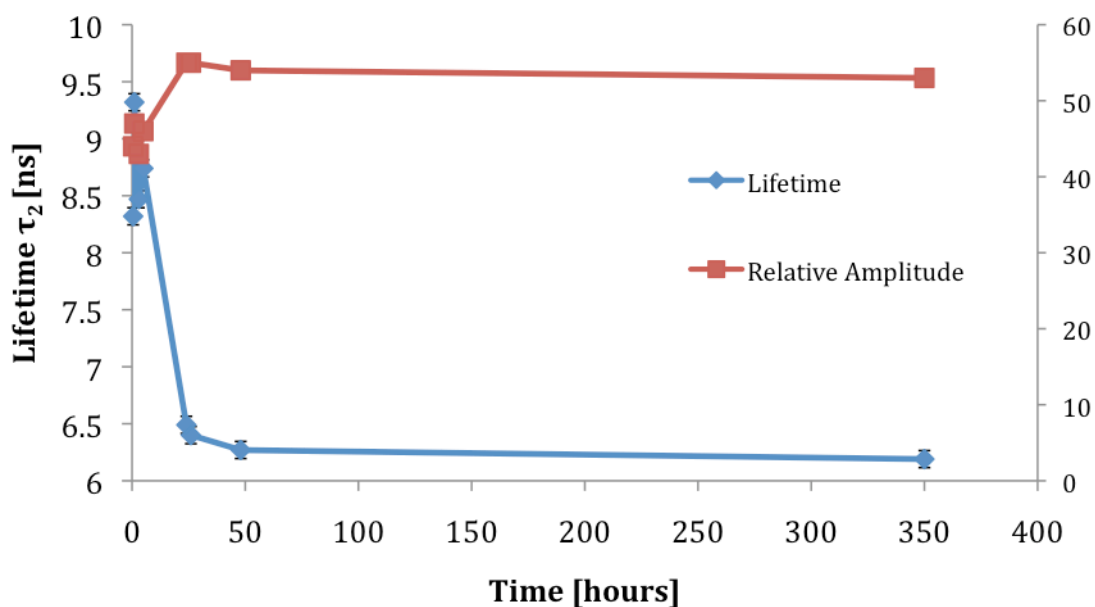


Figure 4.22b Fluorescence lifetime component τ_2 with corresponding relative amplitude component α_2 for 40 μM pH 10 eumelanin, heated to 37°C. Values were recorded between 0.5 and 350 hours.

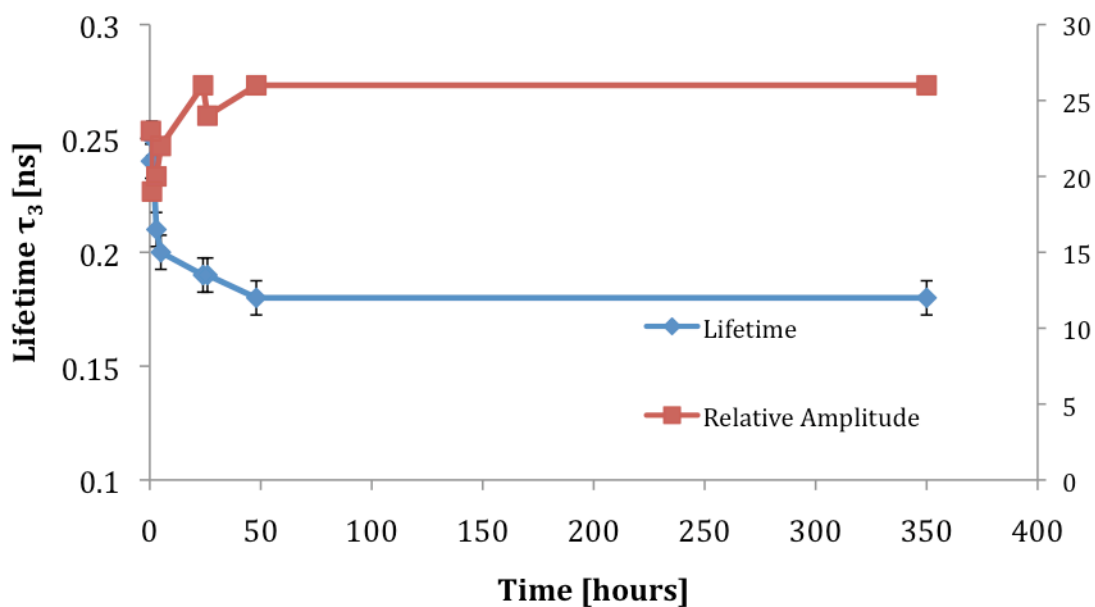


Figure 4.22c Fluorescence lifetime component τ_3 with corresponding relative amplitude component α_3 for 40 μM pH 10 eumelanin, heated to 37°C. Values were recorded between 0.5 and 350 hours.

4.4 Eumelanin Formation from L-DOPA Summary

Through the synthesis of eumelanin from L-DOPA, two environmental affectations were examined for their role in this process, namely pH and temperature.

Three pH values were studied using steady-state and time-resolved fluorescence techniques: approximately pH 2, 7 and 10. Eumelanin aggregate was shown not to be formed under conditions of either pH 2 or 7 in short time scales, with most of the aqueous solution still remaining as L-DOPA after several hundred hours. However, pH 10 solution was observed to form eumelanin within 48 hours. The examination of these formations was carried out by observing time-resolved and steady-state fluorescence characteristics. Several excitation spectra of eumelanin after 48 hours were shown, providing evidence for its heterogeneity due to emission wavelengths having varying excitation spectra.

The fluorescence lifetime of eumelanin under both synthetic environments was observed to fit to a three-exponential decay model via a least-squares fitting decay model, though subsequent analysis by maximum entropy methods revealed a four-exponential decay structure after 48 hours. This could indicate that a standard least-squares fitted model is inappropriate for eumelanin decays, meaning maximum entropy fitting would be more adequate for describing their decays due to their apparently complex and heterogeneous structures.

Copper catalysis at pH 10 was studied, showing that for small volumes of copper sulphate in 1:10 concentration to L-DOPA, the kinetics of eumelanin production doubled, forming within 24 hours as opposed to 48 hours in pH 10 only systems.

As a comparison to pH 10 data at room temperature, steady-state and time-resolved data was obtained for a neutral pH system with a temperature increase to 37°C. Whilst the steady-state absorbance data remained similar to that of pH 10, the

fluorescence spectra was markedly different, with no blue-shift during eumelanin production observed.

Furthermore, lifetimes between both systems maintained differences at early time-points, with the longest component in the high-temperature system being around 1 ns longer, though components of both systems converged over longer timescales. The differences between both systems indicate that changes to the environment during eumelanin production are likely to have some effect on the constituents found in the final eumelanin molecule.

5 Fibril Formation from Melanin

5.1 Introduction

Despite widespread effort, the non-repeating nature of melanin has so far defied attempts to identify its molecular structure. SEM (scanning electron microscopy) studies on melanin produced in the ink sacs of *Sepia officinalis* (commonly known as the cuttlefish) indicate that eumelanin in native form consists of an aggregate of diameter ~ 150 nm. This model of eumelanin as a bio-nanoparticle is well established. An example of this clustered-like aggregate as studied using high frequency AFM-tapping by Clancy et al⁹⁹ is shown below in Figure 5.1

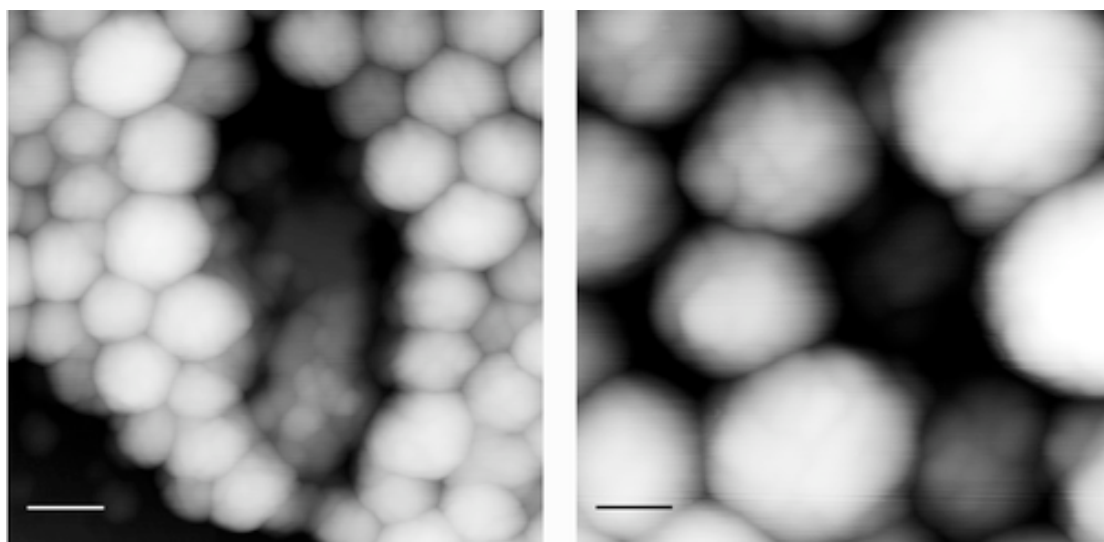


Figure 5.1 Clustered eumelanin aggregation as imaged via AFM by Clancy et al⁸⁵.

However, we have discovered an alternative structural product from the eumelanin synthesis pathway that is fibril rather than particulate in nature and which has similar constituent molecules to naturally occurring melanin.

The fibrillation of L-DOPA derived melanin has potentially wider bearing in helping to understand neurodegenerative diseases as a number of conditions including Alzheimer's, Parkinson's and Huntington's disease are thought to be fibril-based. Indeed, L-DOPA is used in the treatment of Parkinson's disease in order to increase

dopamine concentrations in the brain due to dopamine's inability to cross the blood-brain barrier. Moreover, L-DOPA and dopamine have been shown to disaggregate and inhibit formation of polypeptide amyloid fibrils of β -amyloid¹⁰⁰, which is associated with Alzheimer's disease¹⁹, and α -synuclein, which is associated with Parkinson's disease²¹.

Recently, the formation of fibrils has been observed in *Sepia officianalis* melanin derived from the ink-sacs of cuttlefish¹⁰¹. However, hitherto, no study of fibril formation in L-DOPA eumelanin has been reported. Despite differences in production of both eumelanins, the structural organisations in both cases appear similar.

Outlined in this section are two methods for fibril formation during eumelanin synthesis from L-DOPA, namely a pH 10 formation using the addition of ammonia as a catalyst for eumelanin synthesis, and a pH 7 formation with an increase in temperature to 37°C as a catalyst for eumelanin synthesis. Both are measured via FLIM, AFM and SEM techniques.

AFM images reveal details of the morphology of fibrils at higher resolutions than is available via bright field microscopy. Any standard photon-based microscopy is limited to diffraction dependent resolutions: typically we may only observe details to a scale of around half the wavelength of the incident light, usually resulting in resolution limits of 200 nm. This may be overcome, however, in stimulated emission depletion microscopy (STED) by using a donut-shaped de-excitation beam¹⁰²; or by photo-activated localisation¹⁰³ (PALM) or stochastic optical resolution¹⁰⁴ (STORM) microscopy, which both use a combination of stochastic fluorophore emission and point spread functions to overcome resolution limits.

AFM is limited only by the quality and sharpness of the tip used to carry out measurements. This means that it is theoretically possible to carry out the study of single atoms¹⁰⁵, and that AFM is often used to study the properties of single molecules¹⁰⁶.

As an advancement of the AFM, scanning electron microscopy (SEM) imaging was carried out on fibrils to examine the nanoscale topography of fibrils shown via AFM at higher resolutions. Whilst AFM is limited by properties of the cantilever tip, SEM is free of this problem. An SEM image can be expected to provide images of < 10 nm resolution, though this is dependant on properties of the sample examined. For example, one condition for the use of SEM imaging is that the surface must be conductive in order to remove the flux of incident electrons from the area of the sample that they strike. Fortunately, and somewhat unusually for an organic material, the conductivity of eumelanin has been well investigated and it was determined to be a good electrical conductor¹⁰⁷.

SEM is capable of magnifications to around 500,000 times, though this size of magnification was not used to measure fibrils.

5.2. Slide Treatment

We have also developed a generic procedure to clean and surface treat microscopy slides to be hydrophilic. The method of treatment of slides for FLIM is a two-step process. Firstly, the slide must be cleaned to ensure that it is free of impurities that may affect fluorescence measurements. Since FLIM imaging is carried out on millimeter or micrometer scales, any fluorescent response must be determined to be from our fluorescent molecule and not from contamination on the slide or in the water. In order to make sure no contaminants come from the slides, a solution of 5% potassium hydroxide (by weight) in methanol is prepared by dissolving 11.87g of potassium hydroxide crystals in 300ml of methanol. The mixture is sonicated for 1h to dissolve the potassium hydroxide crystals completely, at which point the slides were immersed for 24h to ensure that all contaminants were removed.

The second part of the slide treatment process involves making the slides hydrophilic i.e. water affinitive. When solvent is added to a hydrophilic slide, even in very small volumes, it will spread out and create a large surface area. This is useful for concentration distribution as it ensures that there is no “halo” of concentration around

the outside of the deposited sample as there would be on a hydrophobic slide, whilst also allowing faster drying times in comparison to untreated slides. To make the hydrophobic slides, they are immersed for a further 24h in a dilute mixture of water, ammonium hydroxide and hydrogen peroxide in 5:1:1 ratio, named “Cleaning Solution 1”. In this instance, 240ml water was mixed with 40ml of both ammonium hydroxide and hydrogen peroxide. After 24h, the slides are removed from the solution and stored in pure deionised water before use.

5.3 pH 10 Eumelanin Formation

5.3.1 pH 10 Eumelanin Formation Experimental

L-DOPA was dissolved from powdered form at a concentration of 1 mM in deionised water, which was free of background fluorescence. The rate of fibril formation increases with the pH and saturated with oxygen. The use of basic pH and oxygen in accelerating oxidative melanogenesis processes with an L-DOPA precursor has been studied previously¹⁰⁸. Hence, we bubbled the sample with air, and 1 mM ammonia was added to increase the pH to 10. Air was pumped through the sample for 48h at a flow rate of 1.5 L/min.

Ammonia was used in place of conventional bases used for eumelanin oxidation such as sodium hydroxide and borate buffer. When depositing sodium hydroxide onto microscope slides, crystallisation was observed and therefore microscopy was not possible, whilst borate is known to complex with L-DOPA¹⁰⁹, which may affect the synthesis of eumelanin.

Eumelanin production was suggested from steady-state absorbance spectroscopic analysis (Figure 2) and by observing colour change in the sample from clear solution to a dark red after approximately 4 hours, then to an inky-black after 48 hours. The sample was then incubated for a period of 2 weeks to allow time for fibril growth. After this period the fibrils were deposited onto glass slides which were cleaned of contaminants using a dilute mixture of 5% potassium hydroxide in methanol and

treated to be hydrophilic using a dilute mixture of water, ammonium hydroxide and hydrogen peroxide in a 5:1:1 ratio as described in §5.2.

Early in the polymerization L-DOPA requires excitation at a wavelength of 280 nm to fluoresce. However, an excitation wavelength of 375 nm is able to measure fluorescence of eumelanin as a measure of aggregate formation. For fluorescence lifetime measurements in a bulk solution, the sample at pH 10 was dissolved in 2.5 ml water in a 4×1×1 cm path-length quartz cuvette at an L-DOPA concentration of 40 μ M. All chemicals described above were purchased in purest form from Sigma Aldrich.

Fluorescence lifetime imaging microscopy (FLIM) was performed using a Zeiss LSM 510 laser-scanning microscope recorded through a 10x water-immersion objective (NA= 0.3; Carl Zeiss, Germany). Excitation of samples on the microscope slide was via a mode-locked Coherent Chameleon wavelength-tunable laser, producing 140fs pulses with a repetition rate of 80MHz and set at wavelengths of either 800 nm or 900 nm to induce multiphoton excitation. The maximum power of the laser is 2.5W at 800nm and 1.7W at 900nm. Excitation wavelengths used were less than or equal to 15% of the total laser power to reduce the potential for photobleaching under multiple scans used to produce FLIM images. Photon counting and image production was carried out using a Becker and Hickl PMC-100 TCSPC module (Becker and Hickl, Germany). Images generated are 256 × 256 pixels, with each pixel containing a unique fluorescence lifetime. Greater than 20,000 counts were taken in each data fit given in this thesis to increase accuracy of bi-exponential fitting functions used to fit fibril lifetimes. After acquisition, images were analysed used SPCImage software (Becker and Hickl, Germany).

Both excitation wavelengths were recorded over the same area of a single sample and both fluorescence signals were collected over the bandpass-chosen spectral region 435-485 nm using a non-descanned detector.

Optical images were taken by a Nikon D300 (Japan) camera modified to fit on the external viewing port of the FLIM system by use of a T-2 Nikon bayonet adapter. AFM images are taken on a Witec Alpha SNOM with AFM adaptor (Germany) using

a 285 kHz resonance tip for high-resolution images. SEM images are taken on an FEI Sirion 200 (USA) field emission scanning electron microscope. Fluorescence decay time measurements were obtained using a Horiba Jobin IBH FluoroCube (UK) system incorporating time-correlated single-photon counting (TCSPC) and NanoLED excitation at 375 nm, with the emission being collected at 480 nm.

To carry out AFM scanning, samples were deposited on glass slides from solution and allowed to dry to avoid any effects of surface water on AFM results. As with FLIM imaging, samples were deposited onto slides at a concentration of 1 mM to improve the likelihood of observing fibril formations.

Samples were clipped onto the AFM stage table to avoid movement during scans. The AFM cantilever was fitted with high frequency tips (AppNano, Germany), operating at around 330 kHz. The exact frequency of the tip was calibrated using dedicated software. The cantilever was operated on a z-piezoelectric stage allowing precise movements over the span of micrometers. The stage was lowered until which point the voltage feedback indicated the same voltage as the setpoint, meaning that the tip would be in contact with the sample.

All measurements were taken in AC mode (detailed in §2.12) to avoid any damage to the sample, and were carried out using a Witek AlphaSNOM Atomic Force Microscope.

Scans were carried out over selected areas of the slide corresponding to obvious fibril formations. These were observed via the attached surface camera operating in bright-field mode.

5.3.2 pH 10 Fibril Formation Results

5.3.2.1 Bright Field Microscopy of pH 10 Fibril Formation



Figure 5.2 Deposition of pH 10 eumelanin onto a slide after 2 weeks incubation at room temperature showing evidence of fibril formation. Fibrils formed under these conditions appeared to show selective branching angles between 20° and 22°.

Figure 5.2 shows a bright field microscopy image indicating fibril formation on a slide. The Branch-like fibril formation observed from bright field microscopy was present throughout the sample, with the dominant branching angle found to be in the range of 20° - 22°, as shown in Figure 5.3.

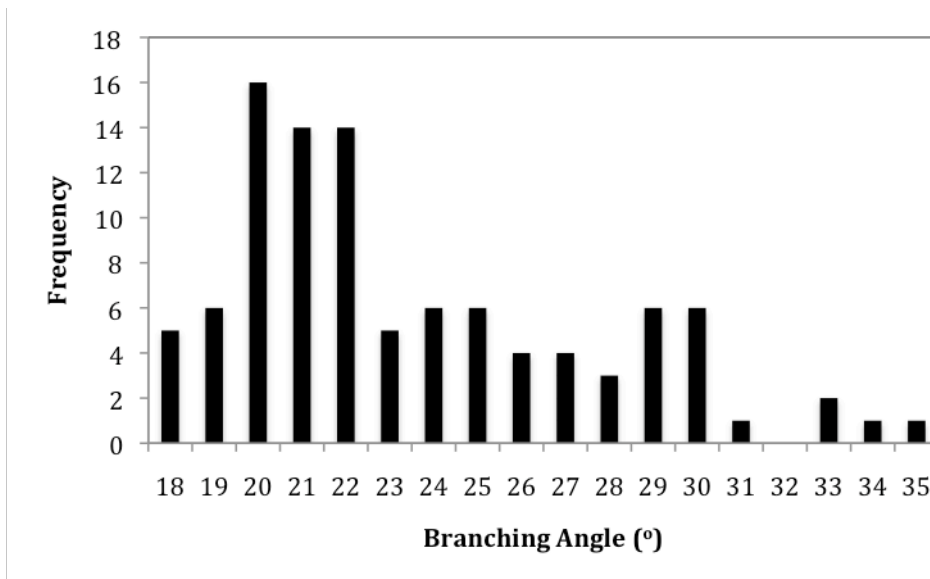


Figure 5.3 Branching angles with their corresponding frequency of occurrence, taken as an average over several areas of slide containing fibril formations formed from pH 10 eumelanin after 2 weeks incubation at room temperature. Fibrils formed under these conditions appeared to show selective branching angles between 20° and 22°.

This process was ubiquitous throughout the slide and remained constant throughout samples. However, specific branching angles of slide-deposited fibrils may be considered to be a consequence of the drying process rather than a natural process. Fibrils are deposited onto slides via a pipette tip before being incubated during the drying processes, so it must be considered that the motion of the liquid during deposition or, indeed, the hydrophobia of slides may play a part in this phenomena.



Figure 5.4 Deposition of pH 10 eumelanin onto a slide after 2 weeks incubation at room temperature showing evidence of fibril formation. Fibrils appear to show no apparent aggregate structure at the nexus of their formation.

More general structural properties can be taken from bright field images. Figure 5.4 above shows that the dried sample contains no clustered aggregate at the nucleus, and shows instead that the fibrils appear to be continuous with some common directionality. All fibrils observed in pH 10 eumelanin solutions displayed this characteristic fibrillar branching, though bright-field microscopy was not able to reveal if branching was a consequence of particular species present at the junctions or was a spontaneous process.

5.3.2.2 Multiphoton Microscopy of pH 10 Fibril Formation

Figures 5.5a and 5.5b show multiphoton microscopy images after excitation under both 800 nm (= 400 nm single photon) and 900 nm (=450 nm single photon) light respectively, with the fluorescence emitted from the sample passing through a bandpass filter of 435-485 nm.

Excitation under 800 nm wavelength light shows clustered fluorescence: fluorescence emission was not observed from all points of the fibril strand, instead discrete emission sites are observed only from specific points on the fibril body. At other areas of the fibril body no discernable fluorescence emission is present. Excitation

under 900 nm wavelength light showed an opposing effect – fluorescence emission was observed from all points of the fibril body, though some more intense clustered emission was still present.

This effect of clustered fluorescence is likely due to either a homogeneous fibril whose specific conformations at cluster sites are favourably oriented for fluorescence, or a heterogeneous fibril made up of several discrete species. From previous knowledge of eumelanin's large numbers of discrete molecular species¹¹⁰, the latter explanation is probable.

Whilst imaging at 800 nm excitation produces a higher fluorescence intensity than 900 nm excitation, this does not necessarily highlight an increased fluorescence response, and may be due to the ti:sapphire laser's inherent peak power being produced at 800 nm.

It should be noted, however, that continuous fibril fluorescence under irradiation under 900 nm excitation may be due to second-harmonic generation, a nonlinear process generating a frequency-doubled fluorescence response, known to occur at high wavelengths and prevalent in continuous fibrillous species such as collagen⁵⁶, evidenced by the apparent differences in fluorescence response under 800 nm and 900 nm light.

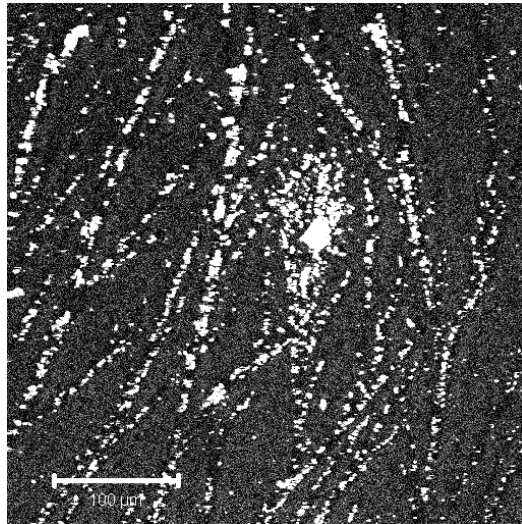


Figure 5.5a Multiphoton fluorescence image of pH 10 eumelanin fibrils, incubated for 2 weeks, excited under 800 nm wavelength light. Fluorescence was collected between 435-485 nm.

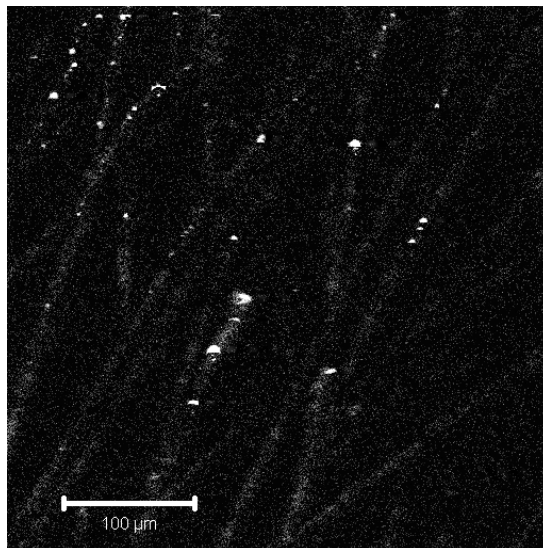


Figure 5.5b Multiphoton fluorescence image of pH 10 eumelanin fibrils, incubated for 2 weeks, excited under 900 nm wavelength light. Fluorescence was collected between 435-485 nm.

5.3.2.3 FLIM Imaging of pH 10 Fibril Formation

Figures 5.6a and 5.6c show multiphoton FLIM images of the shorter lifetime component τ_1 in clusters when excited at 800 nm (5.6a) and 900 nm (5.6c) after 2 weeks incubation, whilst Figures 5.6b and 5.6d show multiphoton FLIM images of

the shorter lifetime component τ_2 when excited at 800 nm (5.6b) and 900 nm (5.6d) after 2 weeks incubation.

Each scan at both wavelengths is taken over the same area of the sample, dimensions $420 \mu\text{m} \times 420 \mu\text{m}$. The lack of fluorescence from most of the fibrils is consistent with the efficient non-radiative processes in eumelanin. Notably there are discrete fluorescent sites within, or most probably outside the fibrils, suggesting isolated monomeric/oligomeric species such as those shown in §3 Figure 3.1, which are not polymerized in the core structure. A comparison between Figures 5.6c and 5.6d show that, at 900 nm, whilst all areas of the fibril display a short lifetime component (τ_1 in Table 5.1), only localized sites at specific areas of each fibril display a longer lifetime component (τ_2 in Table 5.1).

Recent work has suggested excitation at 375 nm corresponds to excitation of DHICA units⁹⁴. The two-photon excitation at 900 nm (\equiv 1 photon at 450 nm) shows a more intense fluorescence during FLIM acquisition than excitation at 800 nm. A two-component decay analysis of the FLIM image suggests most of the fluorescence is between 50 and 200 ps, which is close to the estimated FLIM resolution. A more detailed decay time analysis obtained of a 2 week old sample in a cuvette (§4 Table 4.1) shows that 3 decay components are needed to represent the fluorescence decay and little change in either decay components or their relative intensities occurs as the fibrils grow. This suggests a complex heterogeneous structure to the fibrils based on fundamental oligomer units with unique photophysics, which are formed sequentially from the beginning of the growth process, endure and remain distinct. This would be consistent with growth by the addition of monomers such as DHICA and indolequinone which are π and/or hydrogen bonded analogous to the stacked β -sheets thought to constitute peptide fibrils¹¹¹, though it is impossible to preclude with the current data the possibility that fibrils are formed by some external mechanism such as bacterial growth.

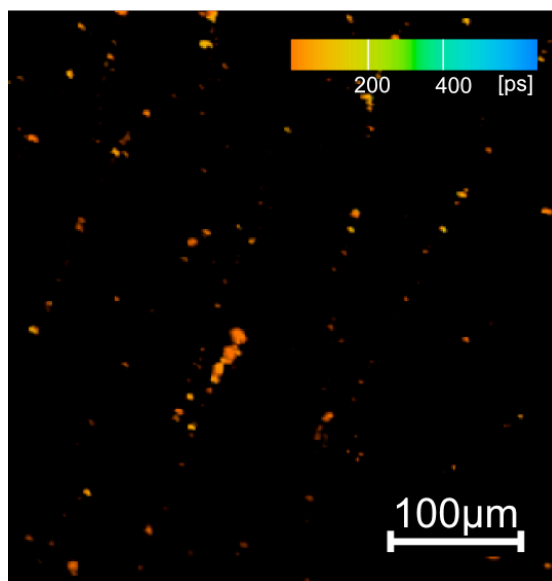


Figure 5.6a Fluorescence lifetime image of pH 10 fibrils, incubated for 2 weeks, showing the τ_1 lifetime component, i.e. the fastest lifetime component, after excitation by 800 nm wavelength light. Lifetimes are distributed between 0 and 500 ps, showing the majority of fluorescence of the fast component comprises of lifetimes < 200 ps. Excitation at this wavelength provided fluorescence only from specific regions of the fibril, apparent as clusters on the lifetime image. Fluorescence was collected between 435-485 nm.

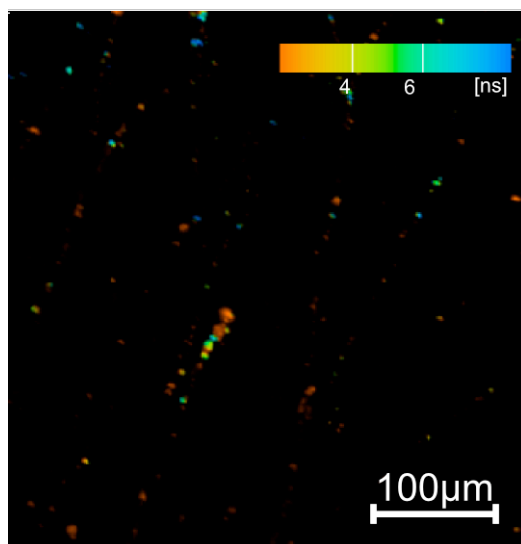


Figure 5.6b Fluorescence lifetime image of pH 10 fibrils, incubated for 2 weeks, showing the τ_2 lifetime component, i.e. the slowest lifetime component, after excitation by 800 nm wavelength light. Lifetimes are distributed between 2 and 8 ns, showing that fluorescence is distributed between 2-7 ns for the slowest component. Excitation at this wavelength provided fluorescence only from specific regions of the fibril,

apparent as clusters on the lifetime image. Fluorescence was collected between 435-485 nm.

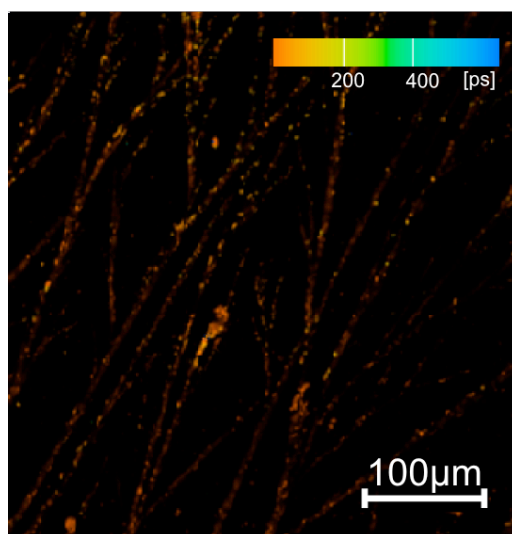


Figure 5.6c Fluorescence lifetime image of pH 10 fibrils, incubated for 2 weeks, showing the τ_1 lifetime component, i.e. the fastest lifetime component, after excitation by 900 nm wavelength light. Lifetimes are distributed between 0 and 500 ps, showing showing the majority of fluorescence of the fast component comprises of lifetimes < 200 ps. Excitation at this wavelength provided fluorescence throughout the fibril, though lifetimes were often too short to be identified. Fluorescence was collected between 435-485 nm.

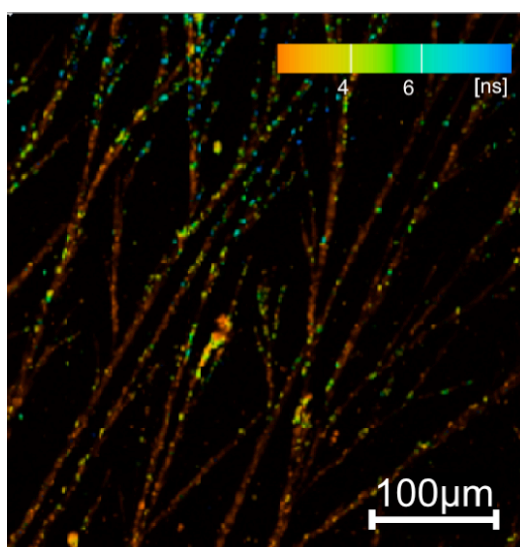


Figure 5.6d Fluorescence lifetime image of pH 10 fibrils, incubated for 2 weeks, showing the τ_2 lifetime component, i.e. the slowest lifetime component, after excitation by 900 nm wavelength light. Lifetimes are distributed between 2 and 8 ns, showing

that fluorescence is distributed between 2-7 ns for the slowest component. Excitation at this wavelength provided fluorescence throughout the fibril, though lifetimes were often too short to be identified. Fluorescence was collected between 435-485 nm.

$\lambda_{excitation}$ (nm)	τ_1 (ns)	α_1 (%)	τ_2 (ns)	α_2 (%)	χ^2
800	≤ 0.2	83.2	2.6	16.8	1.17
900	≤ 0.2	87.6	3.3	12.4	1.18

Table 5.1 Representative lifetime values, taken from sites where “clustered” fluorescence was apparent in fluorescence lifetime images. Lifetimes after excitation by both wavelengths of light showed a two exponential decay comprised of a short, < 200 ps component and a longer component of a few ns.

5.3.2.4 Atomic Force Microscopy of pH 10 Fibril Formation

AFM imaging of eumelanin fibrils shows that there are some morphological structural properties of fibrils only observable on a nano-scale *i.e.* not visible in bright-field or multiphoton imaging. Images showing 50×50 μm regions (Figure 5.6a) indicated that fibril branching visible in bright-field imaging was present. As with bright-field microscopy, these regions of branching are ubiquitous throughout the sample.

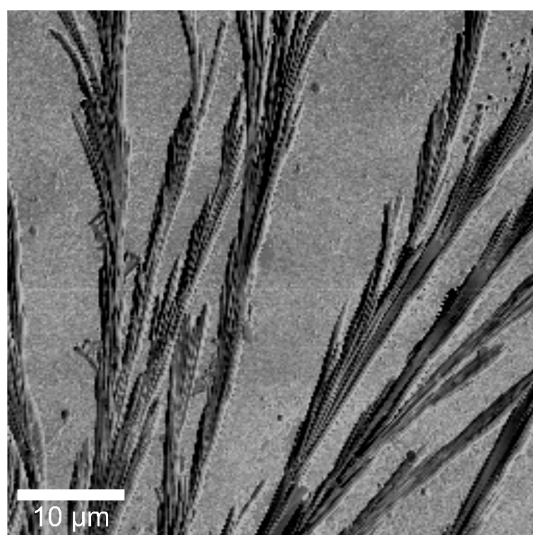


Figure 5.7a Atomic force microscopy phase image of pH 10 eumelanin fibrils after incubation for 2 weeks at room temperature, measured over a region of 50 × 50 μm . Images show evidence of a stacked-fibril structure.

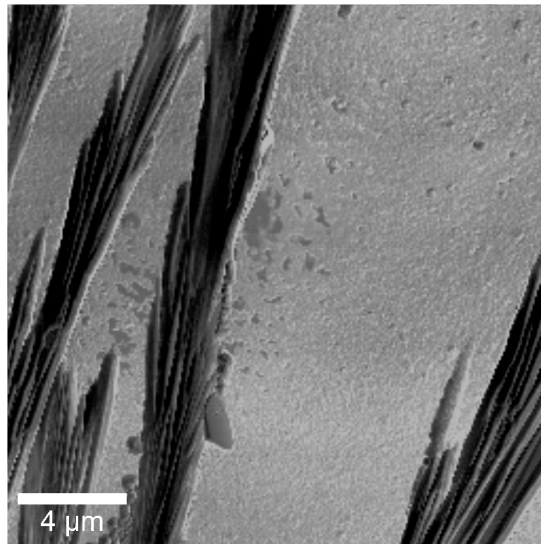


Figure 5.7b Atomic force microscopy phase image of pH 10 eumelanin fibrils after incubation for 2 weeks at room temperature, measured over a region of 20 × 20 μm. Images show evidence of a stacked-fibril structure.

Imaging of smaller regions of the sample (Figures 5.7b and 5.7c) over areas of 20×20 μm and 10×10 μm revealed some even finer structure present on the surface of fibrils. At this size we are able to observe an apparent layering structure of the fibrils wherein each fibril filament is itself made of smaller protofibrils. Aggregation of fibrils appears to be in a horizontal direction, parallel with the slide surface, whilst also some mechanism appears to cause the fibrils to bundle together in a vertical direction, parallel to each other. This aggregation is most apparent in Figure 5.7c.

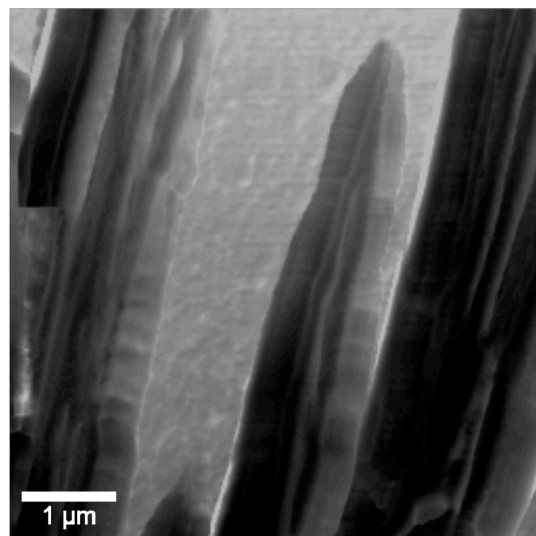


Figure 5.7c Atomic force microscopy phase image of pH 10 eumelanin fibrils after incubation for 2 weeks at room temperature, measured over a region of 5 × 5 μm. Images show evidence of a stacked-fibril structure.

5.3.2.5 Fibril Scanning Electron Microscopy of pH 10 Fibril Formation

SEM imaging of eumelanin fibrils was carried out at magnifications between 1000 \times (Figure 5.8a) and 25,000 \times (Figure 5.8d). Figure 5.8a shows that the branching first identified by bright field microscopy and atomic force microscopy is present on the slide. Furthermore, the image highlights that the size of the fibrils are typically around 2 μm in diameter and therefore have a far larger radius than other organic fibrils. For example, beta amyloid peptide fibrils typically have a radius on the scale of tens of nanometers¹¹².

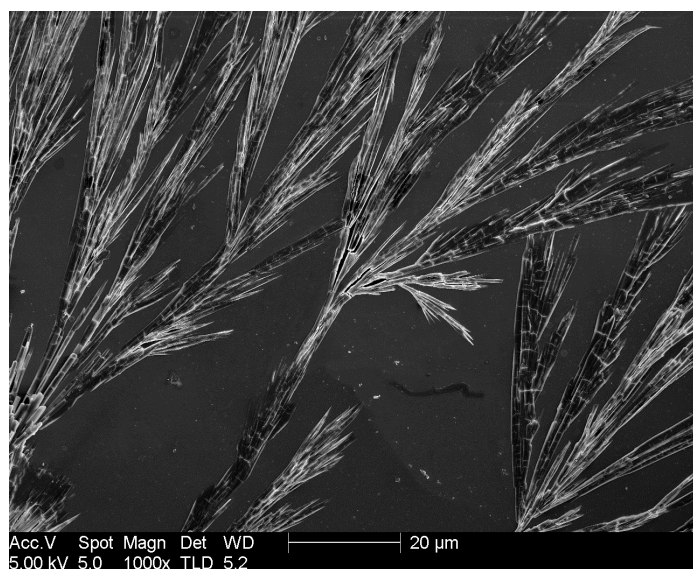


Figure 5.8a Scanning electron microscopy image of pH 10 eumelanin fibrils after incubation for 2 weeks at room temperature, measured at 1000 \times magnification. Images show evidence of a stacked-fibril structure and branching.

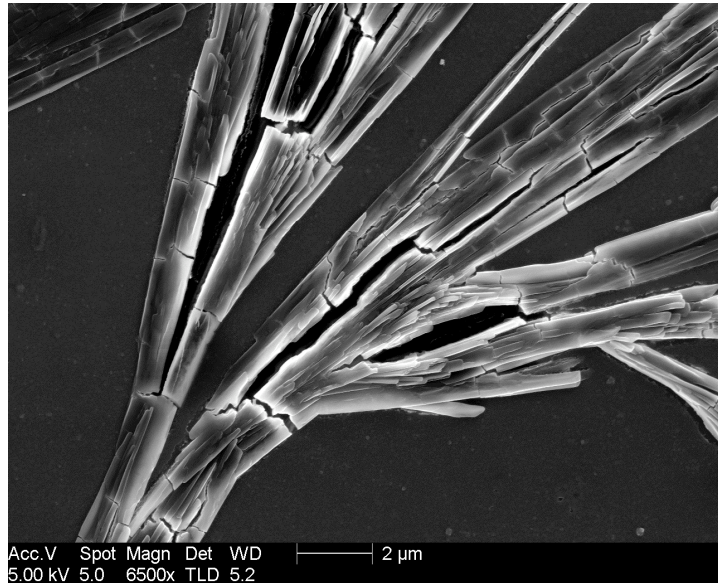


Figure 5.8b Scanning electron microscopy image of pH 10 eumelanin fibrils after incubation for 2 weeks at room temperature, measured at 6500 \times magnification. Images show evidence of a stacked-fibril structure and branching.

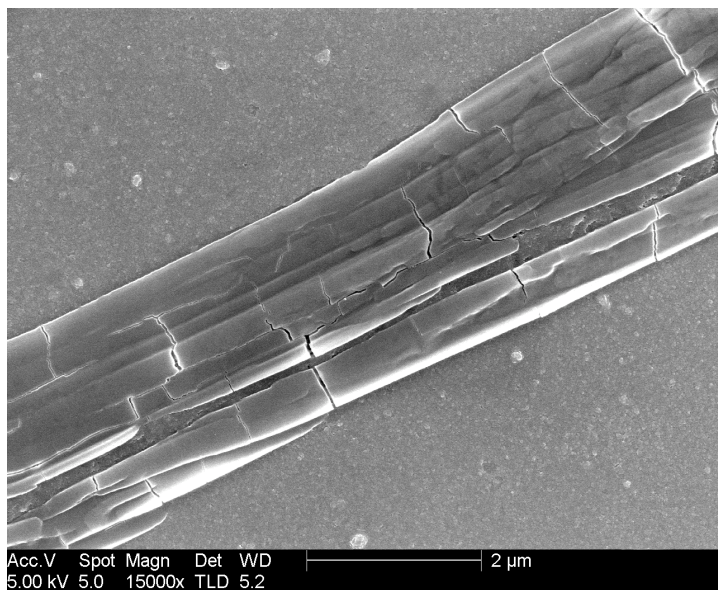


Figure 5.8c Scanning electron microscopy image of pH 10 eumelanin fibrils after incubation for 2 weeks at room temperature, measured at 15000 \times magnification. Images show evidence of a stacked-fibril structure and branching.

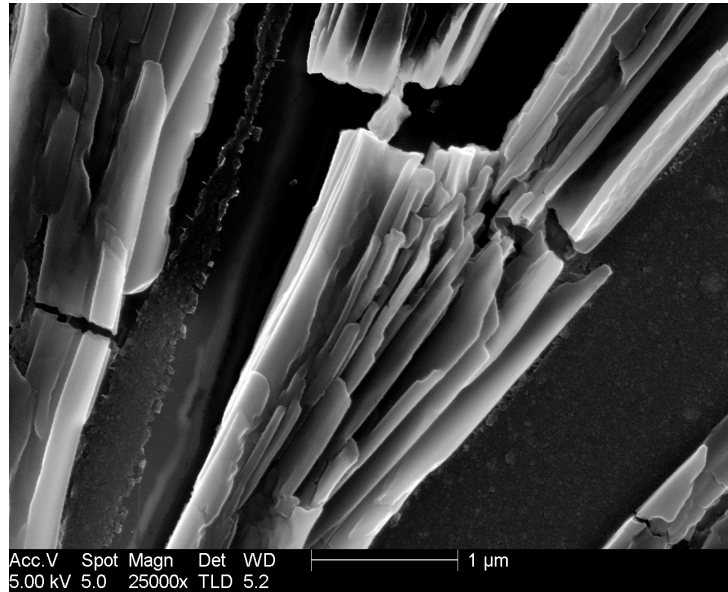


Figure 5.8d Scanning electron microscopy image of pH 10 eumelanin fibrils after incubation for 2 weeks at room temperature, measured at 25000 \times magnification. Images show evidence of a stacked-fibril structure and branching.

Figures 5.8a and 5.8b shows a fibril branch at its nexus. From this image, and the subsequent images 5.8c-5.8d, we were able to confirm the hypothesis made using AFM that fibrils were some collection of smaller filaments. Branching of fibrils appears to occur when, through some mechanism, the larger fibrils “split” and the aggregation of smaller filaments continues in a changed direction. However, effects of the slide surface, e.g. its hydrophobic properties, may drive this directionality of aggregation after splitting.

In all images, some degree of cracking of the fibrils was observed. This is likely a symptom of the drying process of fibrils that occurred before microscopy was carried out. This, however, would indicate that the fibrils have a degree of structural weaknesses which allows them to crack when drying, whereas electron microscopy imaging of other fibrils produced from beta amyloid or alpha synuclein typically show no cracking¹¹³⁻¹¹⁵.

5.4 Fibril Formation at High Temperature

5.4.2 Fibril Formation at High Temperature Experimental

Fibrils were prepared in part as in §5.3.1. L-DOPA was dissolved in deionised water to a concentration of 1 mM. The sample, once fully dissolved, was bubbled with air.

The oxygen-saturated system was simultaneously added to a water bath at an average temperature of approximately 37.5°C. Eumelanin synthesis was observed by a light brown colour apparent after 1 hour and had fully completed after the sample turned an inky-black after approximately 48 hours.

Production of fibrils was confirmed firstly via bright-field microscopy around six weeks after initial dissolving. Slides were monitored before this time, however no fibril production was observed.

All further equipment used is as described in §5.3.1.

5.4.3 Fibril Formation at High Temperature Results

5.4.3.1 Bright Field Microscopy of High Temperature Fibril Formation

Bright Field imaging of body temperature-produced fibrils showed two distinct fibril morphologies – a branched aggregate as observed in pH 10 samples and a denser, more tangled aggregate. Both structures are shown below in Figure 5.9, with the upper area of the slide showing branched fibril formations and the lower area showing the tangled aggregate.

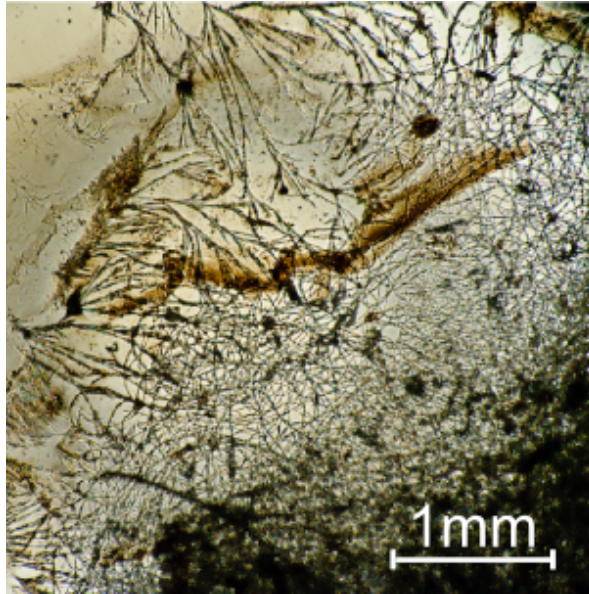


Figure 5.9 Deposition of pH 7 eumelanin onto a slide which was heated to 37°C for 48 hours incubated for 6 weeks at room temperature, showing evidence of fibril formation. Fibrils appear to show structures which are either branched (top of image) or tangled (bottom of image).

It should be noted that whilst bright field imaging revealed both structures, the tangled aggregate was far more prevalent in the sample. Furthermore, the aggregation of both structures appeared to be related, with the branched aggregate often interceding in areas with the tangled aggregate.

5.4.3.2 Multiphoton Microscopy of High Temperature Fibril Formation

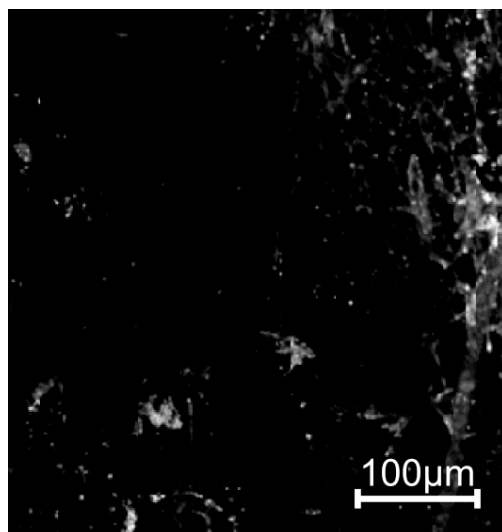


Figure 5.10a Multiphoton fluorescence image of pH 7 eumelanin fibrils heated to 37°C for 48 hours then incubated for 6 weeks at room temperature, excited under 800 nm wavelength light. Fluorescence was collected between 435-485 nm.

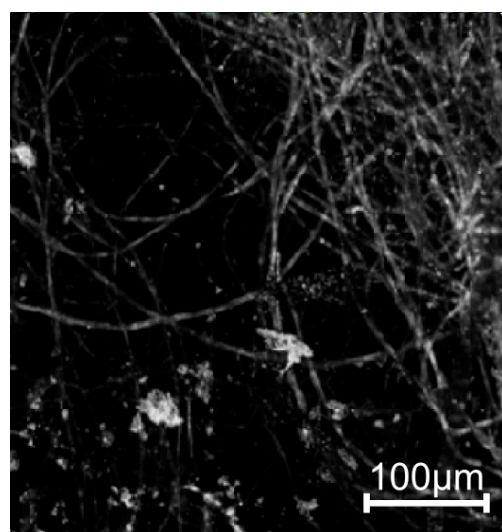


Figure 5.10b Multiphoton fluorescence image of pH 7 eumelanin fibrils heated to 37°C for 48 hours then incubated for 6 weeks at room temperature, excited under 900 nm wavelength light. Fluorescence was collected between 435-485 nm.

Multiphoton excitation at 800 nm and 900 nm is shown in Figures 5.10a and 5.10b respectively. As with pH 10 eumelanin fibril formation, selective excitation

wavelengths appear to produce fluorescence from different areas of fibrils. From Figure 5.10a, we observe that 800 nm excitation produces fluorescence from a greater number of fluorophores than in pH 10 samples, indicating the likelihood of a higher concentration of 800 nm absorbing fluorophores present in the sample. This would suggest that different methods of synthesis produce eumelanin whose concentrations of constituents may vary.

5.4.3.3 FLIM Imaging of High Temperature Fibril Formation

FLIM imaging of fibrils produced over a period of around six weeks was observed to produce fibrils as shown in Figure 5.11a. However, the morphology of the high-temperature melanogenesis fibrils is in contrast to high pH fibrils showed modest concentrations of branched fibrils: most instead having a layered, intertwined structure more akin to amyloid fibrils¹¹⁶. It should be noted, also, that before a period of around six weeks no fibril formation was apparent from the sample and therefore the process of fibril formation in body temperature conditions would appear to take three times as long as high pH formation (shown in §5.4.2)

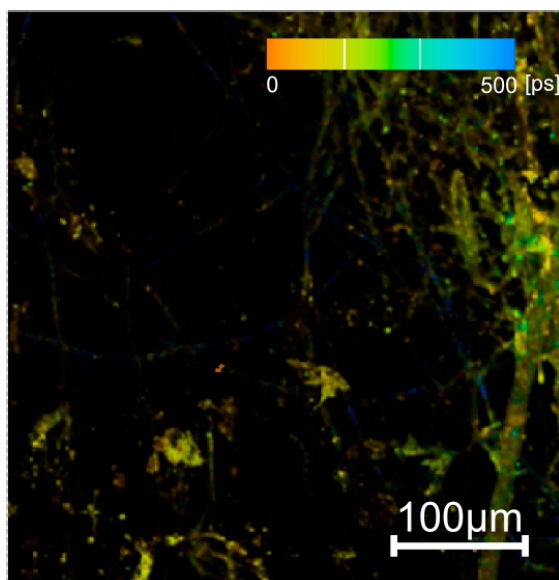


Figure 5.11a Fluorescence lifetime image of pH 7 fibrils heated to 37°C for 48 hours then incubated for 6 weeks at room temperature, showing the τ_1 lifetime component, i.e. the fastest lifetime component, after excitation by 800 nm wavelength light. Lifetimes are distributed between 0 and 500 ps, showing the majority of fluorescence

of the fast component comprises of lifetimes around 250 ps. Excitation at this wavelength provided fluorescence only from specific regions of the fibril. Fluorescence was collected between 435-485 nm.

Despite the morphological differences, some photophysical properties remain similar to high pH formation. When examined via FLIM microscopy, body temperature fibrils appeared to show the clustered, selective excitation characteristics akin to high pH fibril formation. Shown below are samples excited selectively at 800nm and 900nm, with their fluorescence collected at 435-485nm. At 800nm excitation, in Figures 5.11a and 5.11b we see selective excitation of clusters within the fibrils, producing a two-exponential component whose fluorescence lifetimes are given below in Table 5.2.

During excitation at 900 nm (Figures 5.11c and 5.11d), fluorescence is apparent continuously throughout the length of the fibril. Contrary to pH 10 formation, however, fluorescence lifetime values may be obtained from any point on the fibril strand, again indicating the probability of both methods of fibril formation producing fibrils of different concentrations of constituents.

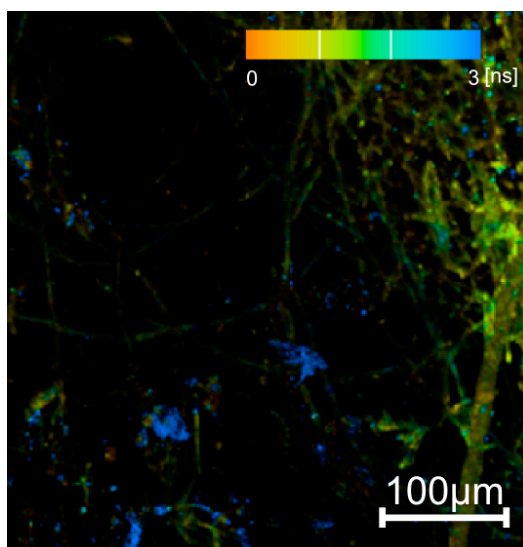


Figure 5.11b Fluorescence lifetime image of pH 7 fibrils heated to 37°C for 48 hours then incubated for 6 weeks at room temperature, showing the τ_2 lifetime component,

i.e. the slowest lifetime component, after excitation by 800 nm wavelength light. Lifetimes are distributed between 0 and 3 ns, showing a distribution in fluorescence from around 1.5-3 ns. Excitation at this wavelength provided fluorescence only from specific regions of the fibril. Fluorescence was collected between 435-485 nm.

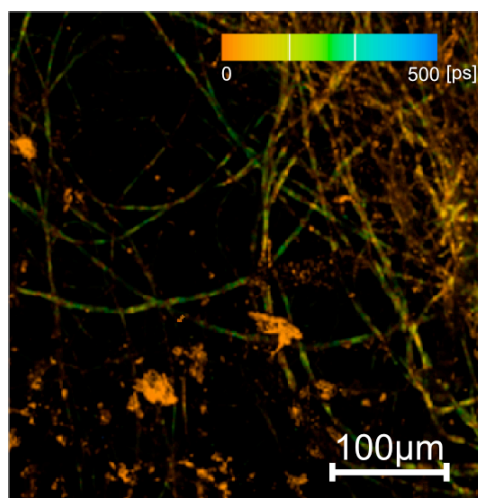


Figure 5.11c Fluorescence lifetime image of pH 7 fibrils heated to 37°C for 48 hours then incubated for 6 weeks at room temperature, showing the τ_1 lifetime component, i.e. the fastest lifetime component, after excitation by 900 nm wavelength light. Lifetimes are distributed between 0 and 500 ps, showing the majority of fluorescence of the fast component comprises of lifetimes < 200 ps, though some evidence of longer lifetimes is present. Excitation at this wavelength provided fluorescence throughout the fibril. Fluorescence was collected between 435-485 nm.

The fluorescence lifetimes of high temperature-formed fibrils are similar to that of high pH fibrils. Typical values of lifetimes taken from sites of clustered fluorescence are shown in Table 5.2. The two-exponential model chosen for both fits appeared to be an adequately fitted model for the fluorescence with both excitation wavelengths reporting χ^2 values <1.2

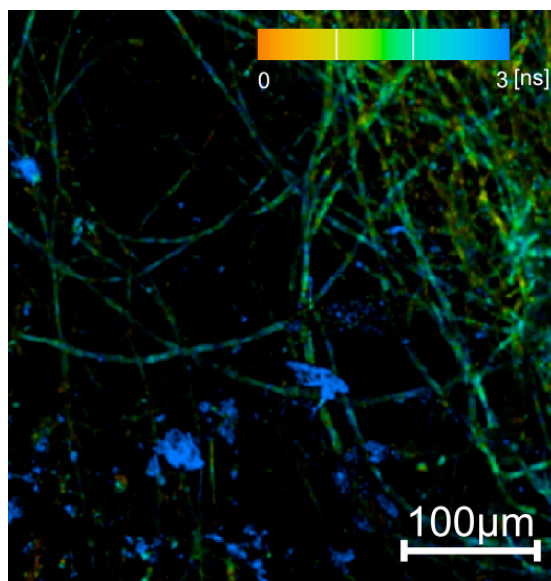


Figure 5.11d Fluorescence lifetime image of pH 7 fibrils heated to 37°C for 48 hours then incubated for 6 weeks at room temperature, showing the τ_2 lifetime component, i.e. the slowest lifetime component, after excitation by 900 nm wavelength light. Lifetimes are distributed between 0 and 3 ns, showing a distribution in fluorescence from around 1.5-3 ns. Excitation at this wavelength provided fluorescence throughout the fibril. Fluorescence was collected between 435-485 nm.

$\lambda_{excitation}$ (nm)	τ_1 (ns)	α_1 (%)	τ_2 (ns)	α_2 (%)	χ^2
800	≤ 0.2	80.5	1.6	19.5	1.16
900	≤ 0.2	84.1	2.8	15.9	1.16

Table 5.2 Representative lifetime values from fibrils, taken from fluorescence lifetime images. Lifetimes after excitation by both wavelengths of light showed a two exponential decay comprised of a short, < 200 ps component and a longer component of a few ns.

The fluorescence from clusters is again dominated by the τ_1 component of less than 200 ps, with the smaller relative amplitude component reporting fluorescence lifetimes of a few nanoseconds (values taken from several points the slide gave components between 2 and 6ns). The similarity between fluorescence lifetime components in heated samples and high pH samples suggest that heated samples

likely show the clusters at a more advanced morphological stage than high pH samples, but that this change in fibril deposition morphology does not effect the fluorescence lifetimes of the sample greatly.

5.4.3.4 Atomic Force Microscopy of High Temperature Fibril Formation

AFM studies of neutral pH body temperature formed eumelanin fibrils showed, as is suggested with bright field microscopy, that unlike pH 10 fibril formations more than one morphology of fibril is present in the sample. As with pH 10 fibrils, one such fibril morphology is branched networks of layered filaments. These are shown below in Figures 5.12a-5.12c.

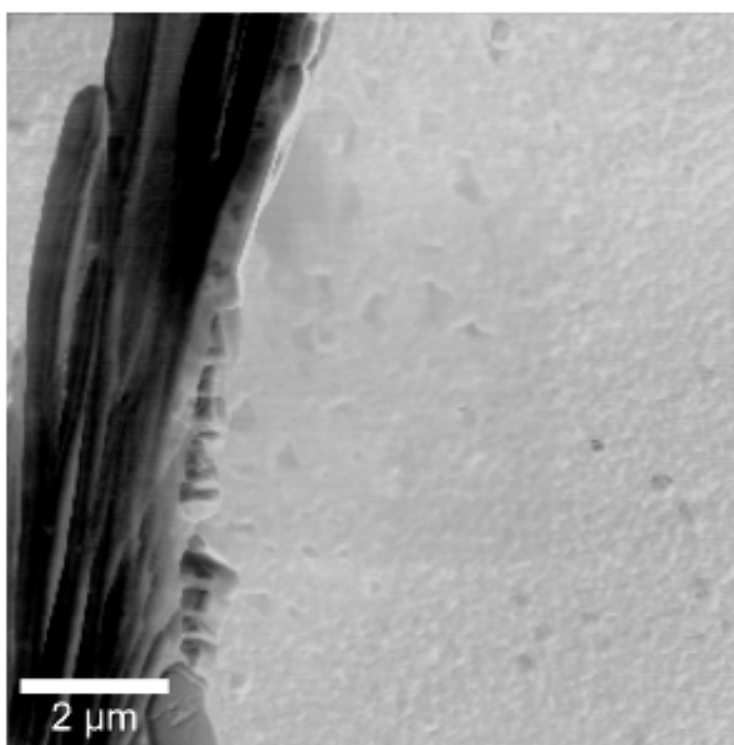


Figure 5.12a Atomic force microscopy phase image of pH 7 eumelanin fibrils heated to 37°C for 48 hours then incubated for 6 weeks at room temperature, measured over a region of 10 ×10 μm. Images show evidence of a stacked-fibril structure.

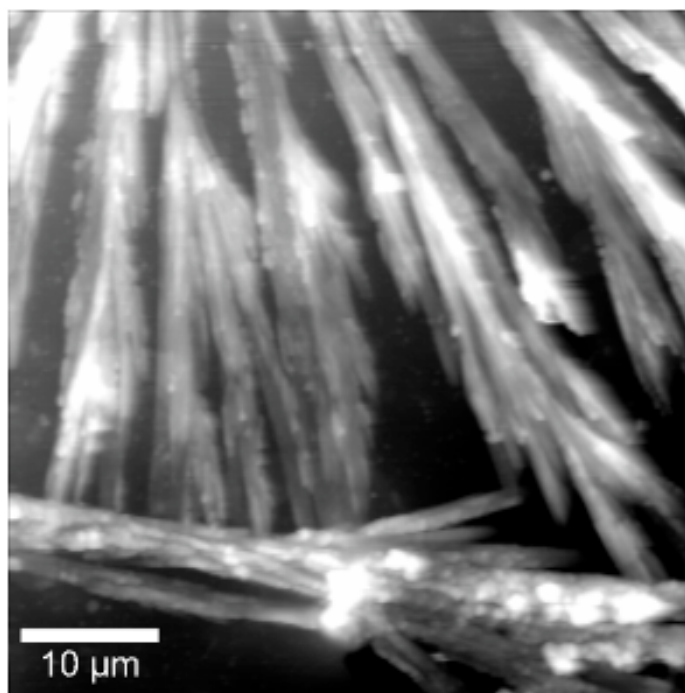


Figure 5.12b Atomic force microscopy topography image of pH 7 eumelanin fibrils heated to 37°C for 48 hours then incubated for 6 weeks at room temperature, measured over a region of 50 × 50 μm. Images show evidence of a stacked-fibril structure.

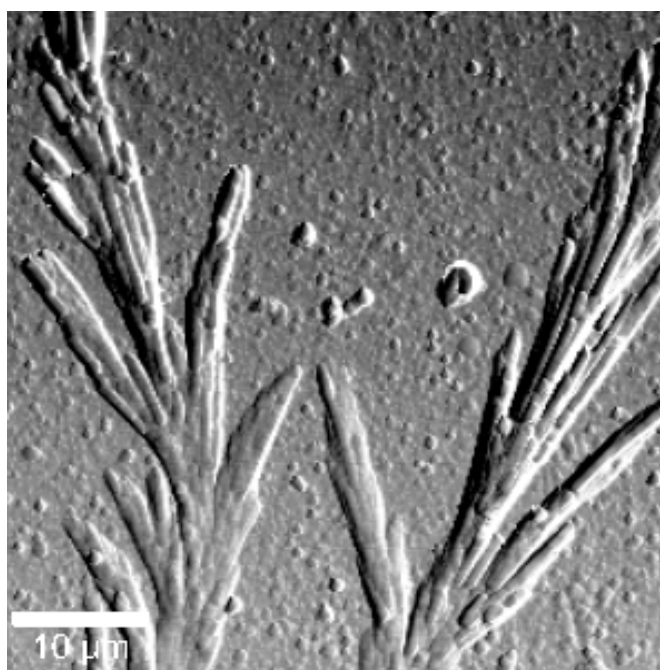


Figure 5.12c Atomic force microscopy phase image of pH 7 eumelanin fibrils heated to 37°C for 48 hours then incubated for 6 weeks at room temperature, measured over

a region of 50 ×50 μm. Images show evidence of a stacked-fibril structure and fibril branching.

Figure 5.12a shows an AFM phase image of the stacked filament structure, whose dimensions are approximately 2 μm wide: analogous in size and structure to high pH fibril formation. This is further confirmed by larger-scale AFM probing of 50×50 μm fibrils as shown via topographical imaging (Figure 5.12b) and phase imaging (Figure 5.12c), where we observed that fibrils of this type were distributed in a branching network, again as shown before during high pH formation.

AFM studies were also able to confirm that these fibrils have a z-depth similar to high pH formations, of around 5-10 μm. An AFM topography image showing structure in three dimensions is shown below in Figure 5.12d.

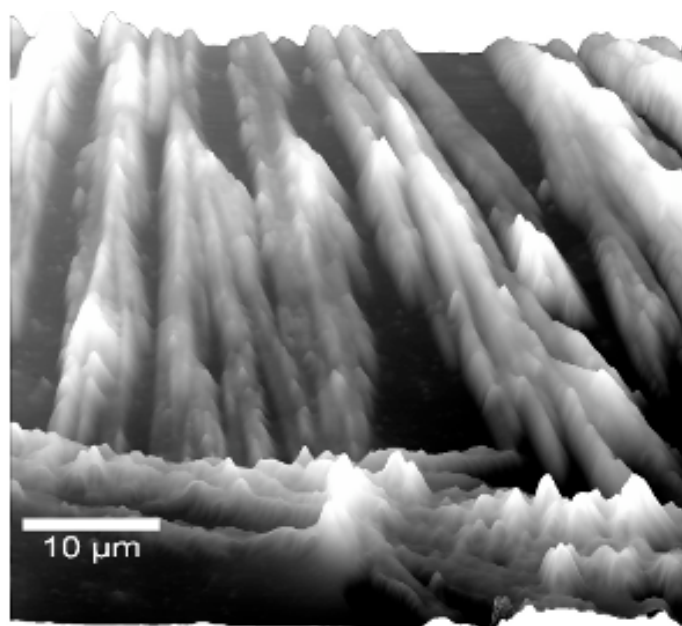


Figure 5.12d 3-dimensional atomic force microscopy topography image of pH 7 eumelanin fibrils heated to 37°C for 48 hours then incubated for 6 weeks at room temperature, measured over a region of 50 ×50 μm. Images show evidence of stacked-fibril structures and show surface heights of around 5-10 μm.

However, larger more intertwined fibril networks, which were observed via bright field and fluorescence imaging microscopy, were confirmed via AFM. These networks are shown below in Figure 5.12e in both two and three dimensions.

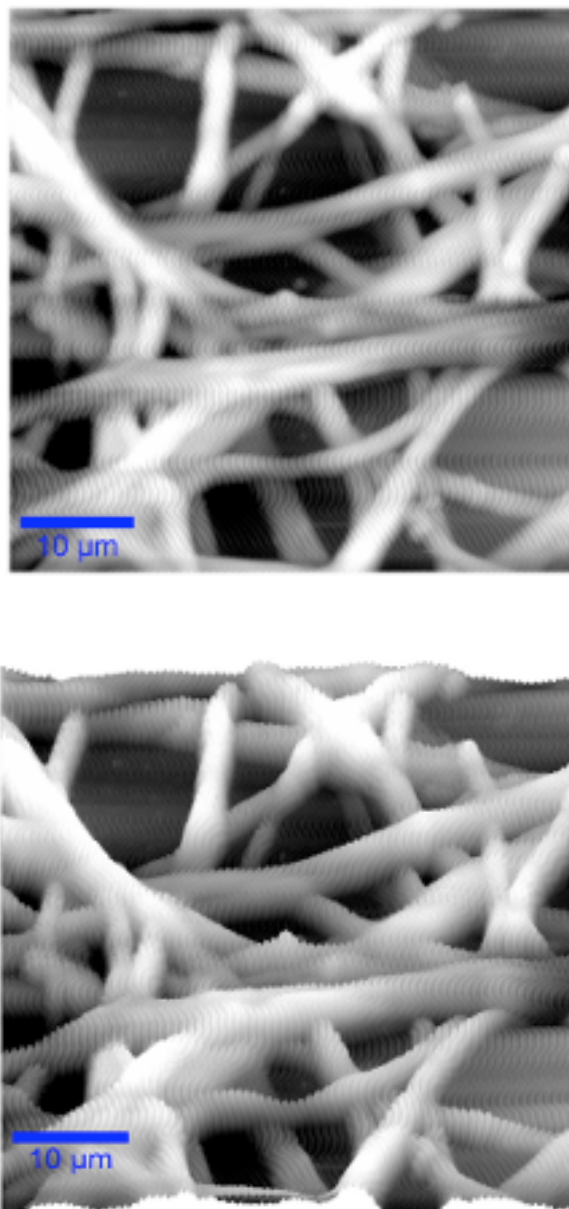


Figure 5.12e 2-dimensional (top) and 3-dimensional (bottom) atomic force microscopy topography image of pH 7 eumelanin fibrils heated to 37°C for 48 hours then incubated for 6 weeks at room temperature, measured over a region of 50 × 50 μm. Images show evidence of tangled fibril structures, with surface heights of around 5-10 μm.

5.4.3.5 Scanning Electron Microscopy of High Temperature Fibril Formation

As with high pH eumelanin formation, SEM of neutral pH eumelanin fibrils was able to confirm their structural properties by examination at a higher magnification and resolution.

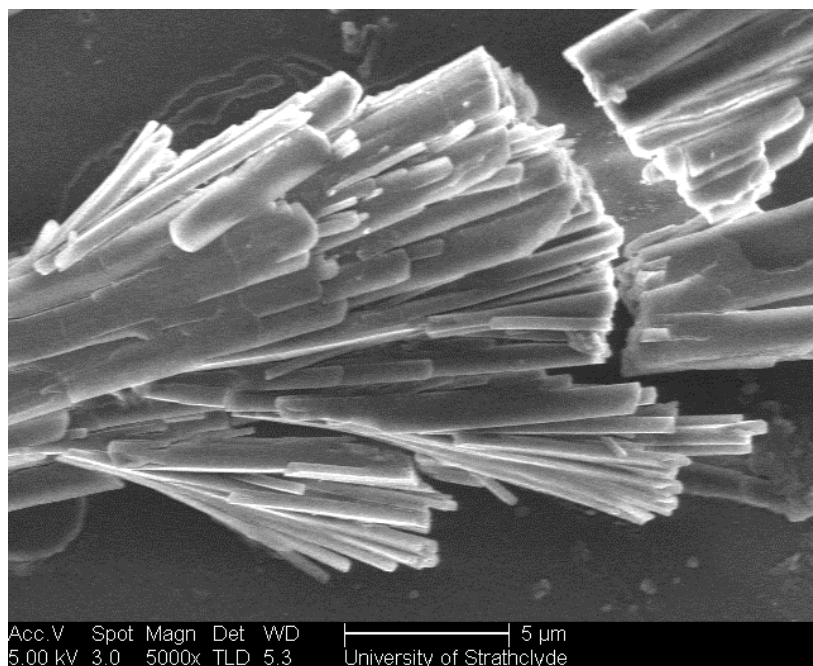


Figure 5.13a Scanning electron microscopy image of pH 7 eumelanin fibrils, heated to 37°C then incubated for 6 weeks at room temperature, measured at 5000× magnification. Images show evidence of a stacked-fibril structure and branching.

Different morphologies of fibrils were observed on the slide. Firstly, the parallel-stacked filament formation was observed throughout the sample (Figure 5.13a). Analogous to high pH fibrils, cracking after drying at room temperature was present in this specific morphology. Again, branching appeared to occur at the site of this fibril cracking (Figure 5.13b).

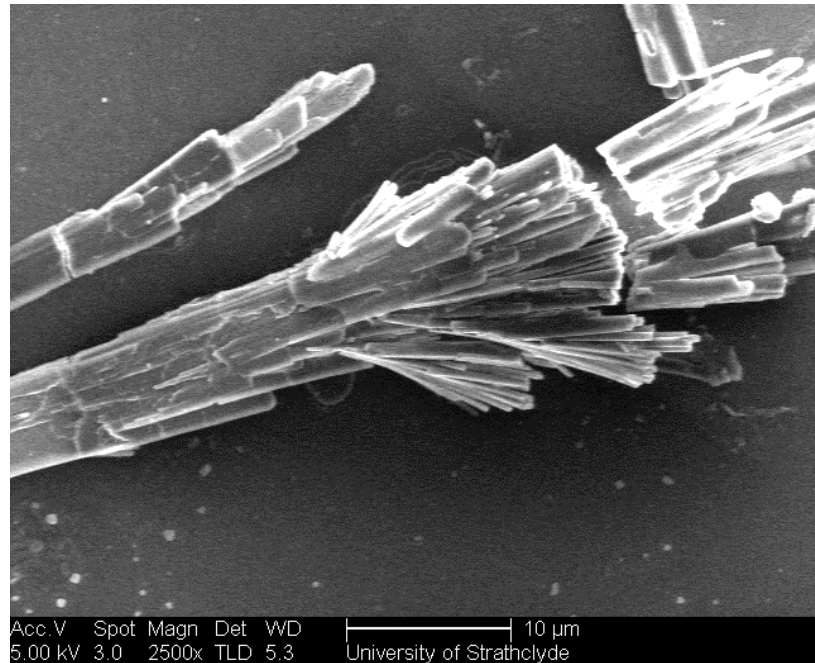


Figure 5.13b Scanning electron microscopy image of pH 7 eumelanin fibrils, heated to 37°C then incubated for 6 weeks at room temperature, measured at 2500× magnification. Images show evidence of a stacked-fibril structure and branching, with some cracking due to drying apparent.

The second morphology present in the sample was an intertwined fibrilisation (Figure 5.13c). This morphology of fibrils was suggested by bright field and AFM imaging of slides and was shown to occur on specific areas of the slide where branched fibrils were infrequent. The intertwined morphology is similar to that of traditional fibrils, though it has no specific directionality (as is common in branched fibrils). SEM imaging of fibrils further shows that branched fibrils and intertwined having a common locus, with the intertwined fibrils forming directly from branched fibrils. This may be observed in Figure 5.13d, an expansion of figure 5.13c, where several points of intersection are highlighted.

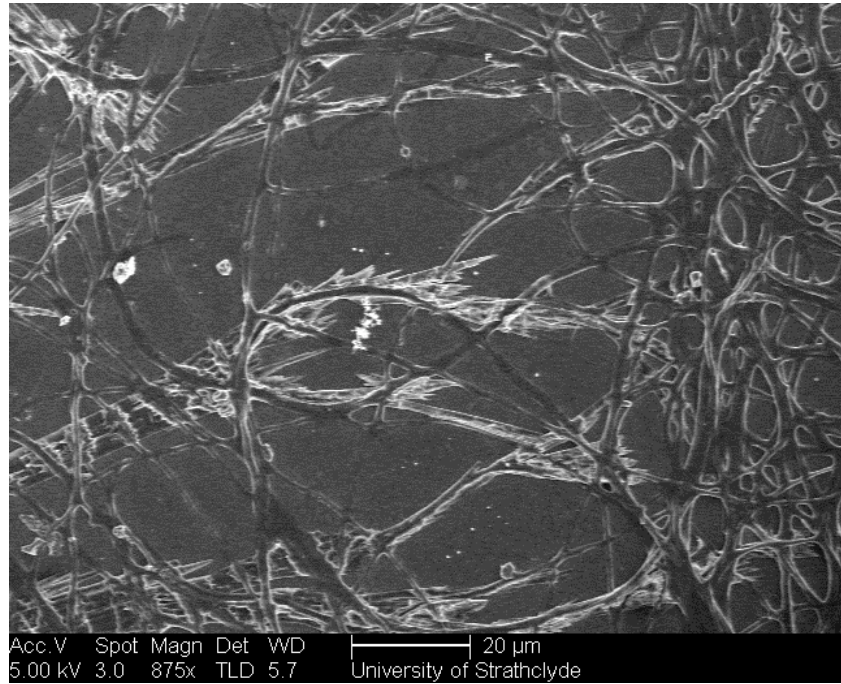


Figure 5.7c Scanning electron microscopy image of pH 7 eumelanin fibrils, heated to 37°C then incubated for 6 weeks at room temperature, measured at 875× magnification. Images show a tangled, unbranched fibril morphology.

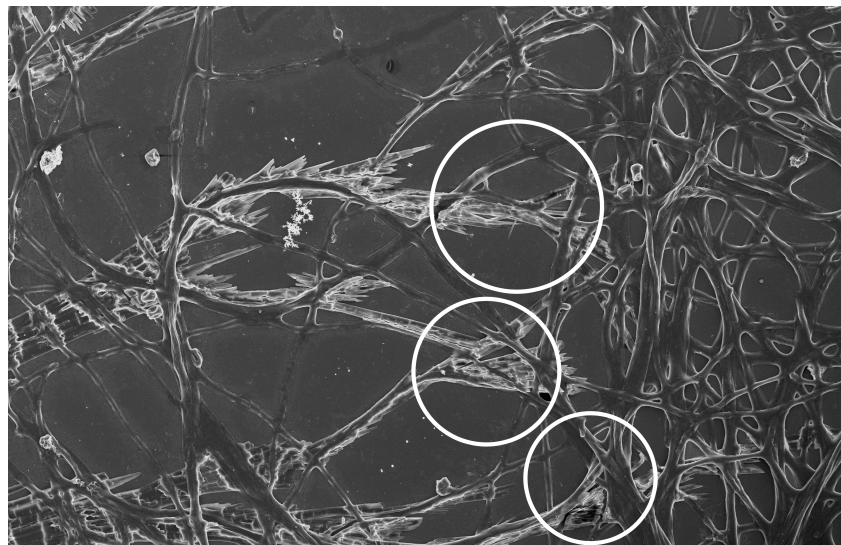


Figure 5.7d Scanning electron microscopy image of pH 7 eumelanin fibrils, heated to 37°C then incubated for 6 weeks at room temperature, measured at 875× magnification. Highlighted areas display regions at which branched fibrils and tangled fibrils appear to join.

Despite these morphologies being the only visible structures that were observed via bright field and AFM imaging, a third morphology was shown to be present in the sample after examination by SEM. This third morphology is shown below in Figure 5.7e, comprising of a connected series of fibrils derived from “doughnut” shaped repeating structures.

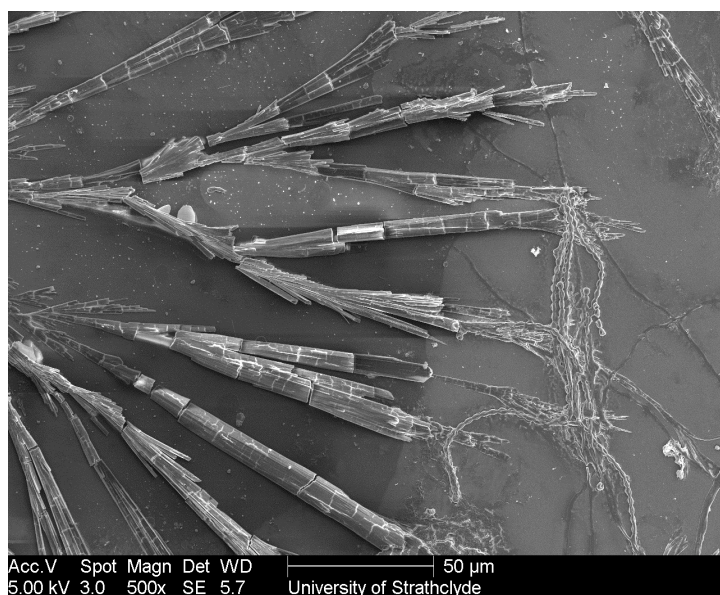


Figure 5.7e Scanning electron microscopy image of pH 7 eumelanin fibrils, heated to 37°C then incubated for 6 weeks at room temperature, measured at 500× magnification. Images show a third fibril morphology comprising of twisted fibril aggregates. From the image, the twisted fibrils appear to be produced from branched fibrils, similarly to tangled fibrils.

However, at higher magnifications, these bead-like structures appear to be caused by twisted aggregation of two or three filament strands, shown in Figure 5.7f. Twisting during aggregation is a pattern usually observed in beta-amyloid fibrils, though twisting on amyloid fibrils generally occurs in a more “loose” manner, occurring over a long length of the fibrils, whereas eumelanin fibril twisting appears to occur over $\sim 2 \mu\text{m}$ filament sections. This gives the fibrils the appearance of bead-like structures at smaller magnifications.

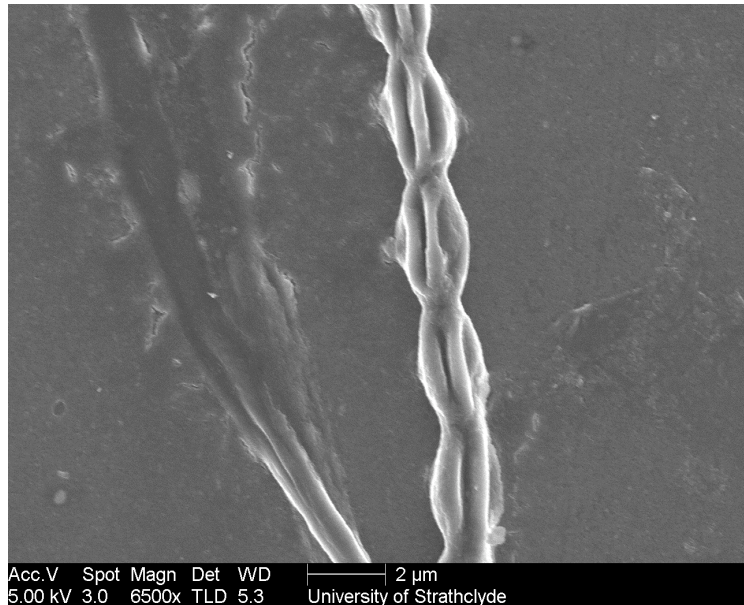


Figure 5.7f Scanning electron microscopy image of pH 7 eumelanin fibrils, heated to 37°C then incubated for 6 weeks at room temperature, measured at 6500× magnification. Images show a third fibril morphology comprising of twisted fibril aggregates leading to a “beaded” structure. This aggregation pattern was not observed in pH 10 fibril synthesis.

From expansion of Figure 5.7e, shown below in Figure 5.7g, twisted fibrils appear to grow directly from cracked fibril sections. However, this form of aggregation was only observed in very few regions of the slide and was highly infrequent. From observations of several areas of the slide, twisted fibril formation did not appear grow from tangled fibril formation at any point.

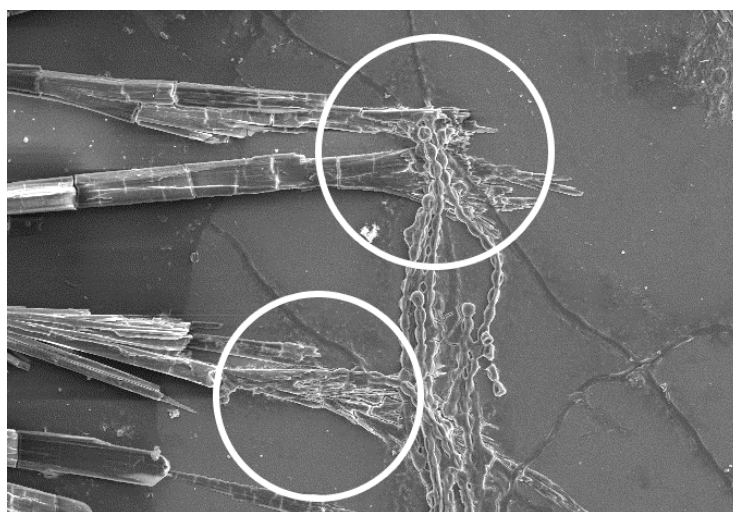


Figure 5.7g Scanning electron microscopy image of pH 7 eumelanin fibrils, heated to 37°C then incubated for 6 weeks at room temperature, measured at 500× magnification. Images show a third fibril morphology comprising of twisted fibril

aggregates. From the image, the twisted fibrils appear to be produced from branched fibrils, similarly to tangled fibrils, at the areas highlighted.

5.5 Eumelanin Fibril Formation Summary

Microscopy studies examining the formation of fibrils in the eumelanin synthesis pathway show that their morphology and photophysical response is highly dependant on environment.

Examination at pH 10 revealed all fibrils present were comprised of a branched network, typically branching at angles of 20°-22°. Both their structure and fluorescence response were examined via FLIM, providing us data on structure available in light microscopy and data of the internal structure of the fibrils which conventional microscopy cannot probe. Fibrils were observed to have a two-exponential lifetime fit comprising a fast, sub-nanosecond component and a longer component of a few nanoseconds duration. Adequate fitting was only available on clustered sites within the fibrils, assumed to be conformations or intermediary species whose absorbance and emission were favourable at the chosen wavelengths.

Further study by AFM and SEM aided in the examination of the outer structure at micrometer and nanometer resolutions. Fibrils were revealed to consist of smaller protofibrils who had stacked together perpendicular to the slide surface.

As a comparison, fibrils formed at pH 7 but with the addition of 37°C heat were studied. FLIM images reported lifetimes similar to that of pH 10 fibril formations, though their fluorescence this time was not observed at clustered sites but throughout the length of the fibrils, thus showing that fibrils were likely constituted by differing concentrations, or indeed species of intermediary.

AFM and SEM of these high temperature fibrils showed three separate structural formations: branched fibrils as observed in pH 10 solutions, tangled fibrils and twisted aggregates. Both tangled and twisted fibrils were produced from the sites of branched fibrils, leading to questions of the branched fibrils role in their production.

It should be noted, however, that these results on fibril formation under both synthetic conditions still require work for full characterisation of properties and differences. For example, pH 10 fibril formations were observed only on slides after drying, whilst high-temperature fibril formations were observed both on slides and in solution.

Given the lack of reproducibility of the fibrils formed at high temperature in solution the question remains as to their synthetic origin. Clearly it is not based only on the melanin chemistry outlined already or the fibrils would be formed every time and have the same morphology. One possibility is the bubbling process allowing bacteria leading to fungal growth into the system, which then acts as a scaffold. This behaviour has been observed before, for example bacterial cellulose is known to form these structures^{117,118}.

6. Duel Synthesis Pathways – a Model for Fibril Formation

6.1 Introduction

Hitherto, the widely accepted model of eumelanin aggregates were of a granular, nanometer scale clustered aggregate, typically made up of oligomers of DHI and DHICA molecules and their precursors⁸³. Many previous studies have confirmed the aggregation pathway¹¹⁹ and photophysics¹²⁰ of such an aggregate. Both *Sepia officinalis* and synthetic eumelanin are generally regarded to be this type of aggregate.

However, in §4, we described a fibril-like aggregate that, depending on conditions of its environment, may increase in size up to several millimeters long. This large, thread-like aggregate has been suggested by studies using x-ray diffraction¹²¹ and during examination of melanin's conductive properties¹²².

Here we describe a new possibility of formation comprising a dual synthesis pathway, allowing L-DOPA to actively both form both cluster aggregates and fibril aggregates spontaneously in solution. This dual-synthesis may also apply to dependants who intake a high concentration of L-DOPA into their bodies, *e.g.* Parkinson's disease sufferers.

6.2 Dual Synthesis Pathway Experimentation

L-DOPA melanogenesis, for purposes of FTIR experimentation, must be carried out using a D₂O solvent. This is crucial for examination of amide bonds at $\sim 1600\text{cm}^{-1}$, where a typical water solvent would produce a vibrational spectrum at 1650cm^{-1} ¹²³. Furthermore, NaOD as a base is preferred to NaOH for similar reasons. The sample must therefore be kept free of any addition of water or other contamination which may effect the spectra produced from eumelanin. To this end, L-DOPA is bubbled with dry air to induce melanogenesis and the process of eumelanin formation is carried out in a sealed glove box to minimise atmospheric water affecting the sample.

The glove box was also purged with dry air during the course of the melanogenesis process to help eliminate atmospheric contaminations present in the room.

L-DOPA was dissolved in D₂O solvent (Sigma Aldrich Co., UK) at a concentration of 1mM. NaOD was added to the solvent to increase the pH to ~10. After a period of time, 100uL of the 1m M L-DOPA was removed and deposited into a FTIR cell, used to measure an FTIR spectrum. A spacer was used to provide a path length of 25 microns for absorbance measurements, consistent with the Beer-Lambert law given in Equation 2.4.

6.3 Dual Synthesis Pathway Results

Fourier-Transform Infrared Spectroscopy (FTIR) was used to analyse vibrational transitions of the eumelanin formation from L-DOPA. The results of FTIR over the course of 248 hours (*i.e.* approximately 10 days) with subtraction of background produced by D₂O are shown in Figure 6.1. Between 0 hours and 24 hours, no transition due to eumelanin or its precursors are observed. This is likely due to the relatively low concentration of L-DOPA (1mM). Up to the period of 24 hours, the peak observed at 1550cm⁻¹ is due to the D₂O solvent used to dissolve L-DOPA. However, between the period of 24 hours and 120 hours, peaks were observed to appear at 1460cm⁻¹, 1530cm⁻¹ and 1600cm⁻¹. These peaks suggest that the L-DOPA precursor has aggregated into a larger structure that was not present in the sample from 0 to 24 hours. The peaks at the given wavelengths, after 120 hours, appear similar to FTIR results tracking the formation of α -helical, random coil or β -sheet formation in proteins¹²⁴. Therefore, we find that long, protein-like structures appear to form in solution.

To further verify these results, a sample was prepared containing the D₂O solvent and the NaOD base. Between 1300cm⁻¹ and 1800cm⁻¹, the sample showed only a peak due to D₂O vibrations between 0 hours and 248 hours. Therefore, we may rule out any vibrational spectrum from the solvent or base causing the appearance of peaks after 120 hours.

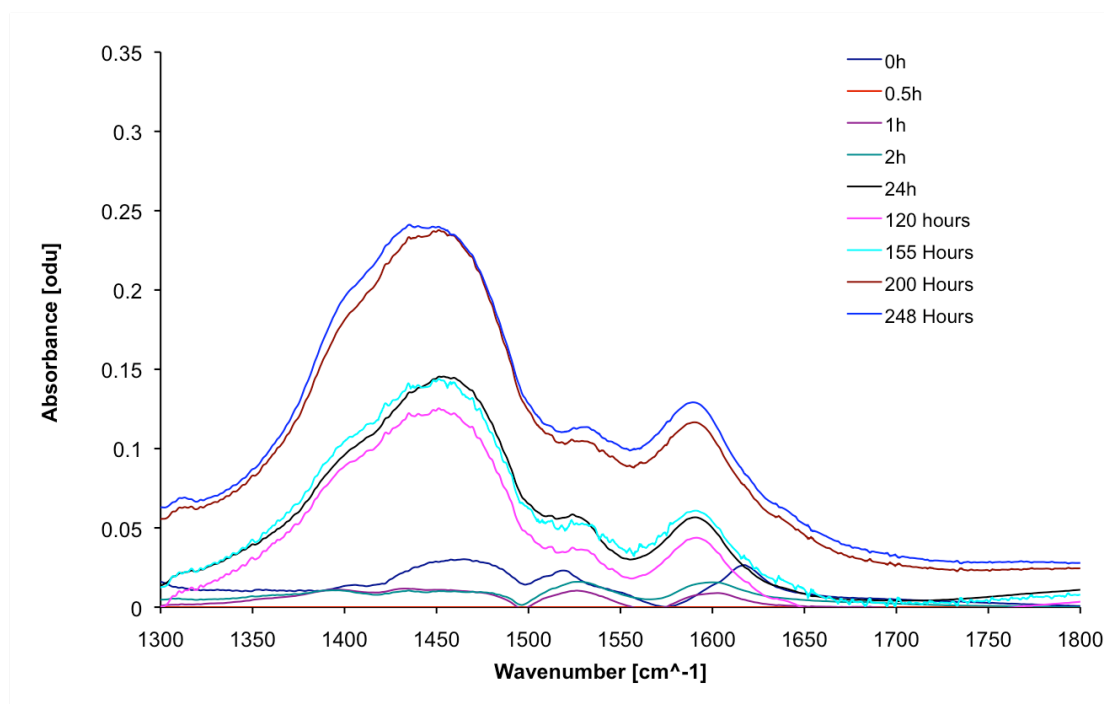


Figure 6.1 Fourier-transform infrared spectroscopy (FTIR) scan of pH 10 eumelanin fibril formation from L-DOPA between 0 hours and 248 hours, taken over 1300-1800 cm^{-1} . FTIR spectra shows evidence of fibril formation after 120 hours. Spectra are corrected to remove FTIR signal produced by D_2O .

From previous research on *Sepia officinalis* aggregates of similar structure to those observed in these formations, we may assume that aggregation is via π -stacked sheets formed in the intermediary stages of eumelanin melanogenesis, and that these stacked-sheets aggregate via hydrogen bonding of phenol and indole groups present in solution. A diagram illustrating this formation is given in Figure 6.2.

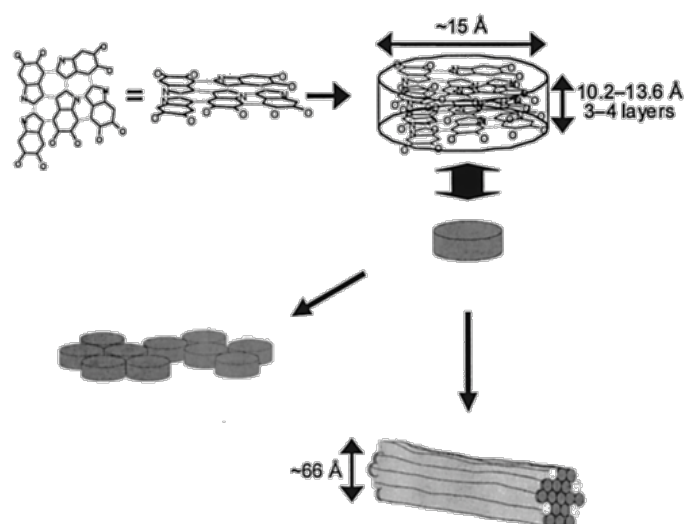


Figure 6.2 Formation of stacked oligomer structures as observed in *Sepia officianlis* melanins¹⁰¹

The results of these studies support the stacked oligomer model proposed for synthetic eumelanin formation. At a primary level, the structure of these fibrilous aggregates likely contains a approximately 3-5 DHI or DHICA monomer units. These planar sheets π stack to form smaller sub-fibrils, which proceed to hydrogen bond in a horizontal direction to form larger macrofibrils observable through bright field imaging. This is possible through oxidation states available in eumelanin formation, where some primary structure may be earlier synthetic states of DHICA and DHI. The uniform diameters observed in our studies suggest that there is a limit to the overall diameter of the macrofibrils. Further studies are required to determine the cause of this, though it may simply be a limit on number of protofibrils available for hydrogen bonding.

Unpublished data in our group suggests that L-DOPA and eumelanin derivatives have the potential to form stacked, π -bonded structures needed for this model. Thioflavin T (ThT) was used to study aggregation akin to its use in the study of amyloid fibrils, wherein its binding into sheet-like aggregates induces an increase in fluorescence emission intensity. However, more study is needed in this area to verify the particular mechanisms of eumelanin and its products in the formation of fibrils.

Despite these studies, it is likely that branching angles as observed in pH 10 fibrils are a product of substrate-fibril interactions and therefore have no likely consequences in the overall potential for the production of fibrils *in-vivo*.

6.4 Dual Synthesis Pathway Conclusions

A model was established for the formation of fibrils during eumelanin synthesis involving two products: both the granular, nanometer scale aggregate produced in the traditional view of melanin, and also a amino-acid fibril consisting of a stacked-aggregate of one or more eumelanin derivatives.

FTIR data provides evidence for this, reporting the structure to be similar to that of a deuterated amide bonded formation. During the early hours of formations, FTIR reports only a deuterium peak, until after 120 hours peaks are apparent whose wavenumbers correspond to protein aggregation. The presence of these peaks are likely due to a co-operative structural formation.

Despite this evidence pointing towards protein-like fibril formation, much more research is required before a formal theory may be adopted, with the question of this method of fibril formation in high pH systems still unanswered.

7. Conclusions and Future Research

7.1 Conclusions

Fluorescence techniques were used in conjunction with several systems of microscopy in order to establish both intrinsic photophysical and structural information on eumelanin and its derivatives, specifically L-DOPA.

The tyrosine-based amino acid L-DOPA was studied initially. Its absorbance and fluorescence spectra at neutral pH values were presented and compared with that of the other fluorescent amino acids: tyrosine, tryptophan and phenylalanine. Examination of both their molecular structures and their steady-state and time-resolved fluorescence responses indicated that the small changes in molecular makeup of the functional group responsible for fluorescence produces a large change in photophysical characteristics, including a shift of both its absorbance and fluorescence spectra peaks to different wavelengths, and a change in its lifetime values. Studies of molar extinction coefficients revealed increasing $-OH$ group presence on the benzene ring lead to higher extinction coefficients in the fluorescent amino acids.

The synthesis of the skin pigment eumelanin from L-DOPA was investigated in detail. The local mechanisms which drive the formation of eumelanin were studied including pH and temperature effects. Steady-state and time-resolved fluorescence was used to study formation at three specific pH values: 2, 7 and 10. From these studies, we observed that only in pH 10 solution was eumelanin able to form within a period of two days.

Thus, pH 10 formation was studied in a more detail. The excitation spectra of the 48 hour product was examined and showed that several emission wavelengths produced different excitation spectra, indicating the inhomogeneity of the molecule. Analysis of lifetimes was carried out by both exponential fitting methods and maximum entropy fitting methods. Exponential fitting methods indicated a three exponential

decay, though contrary to this maximum entropy fitting indicated a four exponential decay. This is likely due to high-exponential systems generally fitting both three and four exponential, though this provides an explanation for the relatively high chi-squared values in three-exponential fitting models.

The effect of copper on pH 10 eumelanin production was subsequently studied, indicating that in a solution containing 1:10 copper: eumelanin concentration, eumelanin production is increased, with reaction kinetics twice the rate as copper-free solution and forming eumelanin in only 24 hours. The lifetime spectra was also studied and concluded to be similar to that of copper-free pH 10 eumelanin.

To compliment the observation of eumelanin formation in a high pH system, a study was carried out into the development of eumelanin by the mechanism of heating to body temperature. The results of the study showed eumelanin formation in similar time periods to high pH synthesis, but with a different steady-state fluorescence response. This was likely due to different structural and conformational formations in melanin due to different synthetic environments as eumelanin is reported to be highly pH-sensitive.⁹⁸

The structure of eumelanins produced at high pH and high temperatures were studied and revealed to comprise of a network of fibrils. High pH formations were initially studied, indicating a branched fibril structure when observed via microscopy. These structures produced fluorescence lifetimes of similar values to bulk fluorescence lifetimes, indicating that these forms are likely present in the sample throughout its production, though in early stages may be too small to observe via light microscopy. Higher resolution examination at smaller scales was carried out by both AFM and SEM imaging and indicated that the large macroscopic fibrils observed via bright field imaging and FLIM were the product of many smaller protofibrils, as is the case with some fibril systems in nature such as cellulose.¹²⁵

Further to the high pH study, bright field and FLIM imaging of high temperature fibrils indicated two fibril forms: one similar in its branched layout to high pH fibrils and another more analogous to typical fibril formations of beta amyloid with a tangled overlapping structure. Lifetimes of tangled fibrils taken by FLIM indicated some

similarities to branched fibrils whilst also indicating that tangled fibrils produced fluorescence lifetimes throughout their structure, contrary to the branched fibril system which only produced discernable fluorescence lifetimes at specific sites. Further SEM study revealed a third fibril structure comprised of a thinner, weaved fibril.

Finally, a model for the formation of fibrils was proposed, with FTIR studies indicating the presence of long aggregated networks akin to protein α -helix, β -sheet or random coil formations in a eumelanin system produced from L-DOPA in heavy water. From this, a theory was established of dual synthesis pathways of both a fibril like structure, produced from aggregates of monomeric species of L-DOPA and eumelanin precursors, and a clustered particulate structure produced from DHI and DHICA in the traditional view of eumelanin. However, the effect of potential bacteria in the solution producing a scaffold for L-DOPA aggregation cannot be discounted.

Despite thorough investigation, more study is needed to identify both the true nature of fibril formation and its potential for formation and damage in the human body. Additional future work is detailed in the following section.

7.2 Future Research

Although significant progress had been made onto the structures of eumelanin, much remains to be studied.

In the process of fibril formations, it would be appropriate that the morphology of fibril formation using microscopy and their photophysical properties using fluorescence be studied a low-pH environment in greater depth due to neutral and high pH systems being discussed in some detail in this thesis. Notwithstanding difficulties in formation of eumelanin at low pH values, an increase in temperature may be able to overcome this obstacle. Due to formations of fibrils in eumelanin synthesis having differing structures at both neutral and high pH values, there is a

possibility that low pH values may induce a fourth fibril structure. Also, based on the neutral pH and high pH studies taken in this report, further investigation into the time between formation of a characteristic eumelanin absorbance spectra (48 hours) and observation of fibrils (2 weeks) may provide more information into the kinetics of formations.

As aggregation of fibrils is crucial to their development, and in any potential pathology in the human body, a FRET sensor may be in future used to monitor their aggregation and examine their magnitude of formation in solution.

Besides pH changes, there is a need for study of systems related to the body. Due to studies carried out into the potential of fibrils to cause a number of diseases (referenced elsewhere in this report) it seems essential that some study is carried out, for example using immunohistochemistry in a murine model of fibril formation, to understand the potential for humans with higher than average L-DOPA amino acids in their bodies – Parkinson's sufferers being one such case – to induce L-DOPA fibrils in the body. This may be carried out in a mouse or rat model, used often in medicine and immunology as an analogous system to the human body. For in-vitro studies, it may be useful to examine fibril formations using a confined cavity sol-gel or some other small environment as a model system.

Recalling the main thrust of the work was to accelerate the fibril formation previously observed, it would be crucial to investigate further the eumelanin formed under sealed conditions without bubbling in order to exclude the possibility of bacteria producing fibrils observed in this thesis.

References

- 1 Kyriakidis, N. B. & Skarkalis, P. Fluorescence spectra measurement of olive oil and other vegetable oils. *Journal of AOAC International* **83**, 1435-1439 (2000).
- 2 Karoui, R. *et al.* Development of a rapid method based on front face fluorescence spectroscopy for the monitoring of egg freshness: 1—evolution of thick and thin egg albumens. *European Food Research and Technology* **223**, 303-312 (2006).
- 3 Egelandsdal, B. r., Wold, J. P., Sponnich, A., Neegard, S. & Hildrum, K. I. On attempts to measure the tenderness of Longissimus Dorsi muscles using fluorescence emission spectra. *Meat Science* **60**, 187-202 (2002).
- 4 Kennedy, T. C., Lam, S. & Hirsch, F. R. Review of Recent Advances in Fluorescence Bronchoscopy in Early Localization of Central Airway Lung Cancer. *The Oncologist* **6**, 257-262 (2001).
- 5 Martin, K. *et al.* Detection of Early Bladder Cancer by 5-Aminolevulinic Acid Induced Porphyrin Fluorescence. *The Journal of Urology* **155**, 105-110 (1996).
- 6 Klucken, J., Outeiro, T. F., Nguyen, P., McLean, P. J. & Hyman, B. T. Detection of novel intracellular alpha-synuclein oligomeric species by fluorescence lifetime imaging. *The FASEB Journal* **20**, 2050-2057 (2006).
- 7 Galletly, N. P. *et al.* Fluorescence lifetime imaging distinguishes basal cell carcinoma from surrounding uninvolved skin. *British Journal of Dermatology* **159**, 152-161 (2008).
- 8 Teale, F. & Weber, G. Ultraviolet fluorescence of the aromatic amino acids. *Biochemical Journal* **65**, 476 (1957).
- 9 Macmillan, A. M. *et al.* in *Fluorescence Methods and Applications: Spectroscopy, Imaging, and Probes* Vol. 1130 *Annals of the New York Academy of Sciences* (ed O. S. Wolfbeis) 300-304 (Blackwell Publishing, 2008).
- 10 Teale, F. The ultraviolet fluorescence of proteins in neutral solution. *Biochemical Journal* **76**, 381 (1960).
- 11 McGuinness, C. D., Sagoo, K., McLoskey, D. & Birch, D. J. S. Selective excitation of tryptophan fluorescence decay in proteins using a subnanosecond 295 nm light-emitting diode and time-correlated single-photon counting. *Applied Physics Letters* **86**, 261911-261913 (2005).
- 12 Gong, H. *et al.* Tryptophan fluorescence reveals induced folding of *Vibrio harveyi* acyl carrier protein upon interaction with partner enzymes. *Biochimica et Biophysica Acta (BBA) - Proteins & Proteomics* **1784**, 1835-1843 (2008).
- 13 Neitchev, V. Z. & Boudevska, H. L. The kinetics of complex formation of tryptophan containing proteins with pyridinium salts. *Molecular Biology Reports* **2**, 303-309 (1975).
- 14 Dusa, A. *et al.* Characterization of Oligomers during Alpha-Synuclein Aggregation Using Intrinsic Tryptophan Fluorescence. *Biochemistry* **45**, 2752-2760 (2006).

- 15 Clancy, C. M. R., Nofsinger, J. B., Hanks, R. K. & Simon, J. D. A hierarchical self-assembly of eumelanin. *Journal of Physical Chemistry B* **104**, 7871-7873 (2000).
- 16 Bridelli, M. G. Self-assembly of melanin studied by laser light scattering. *Biophysical Chemistry* **73**, 227-239 (1998).
- 17 Halliday, G. M. *et al.* Evidence for specific phases in the development of human neuromelanin. *Journal of Neural Transmission* **113**, 721-728 (2006).
- 18 Zecca, L. *et al.* Substantia nigra neuromelanin: Structure, synthesis, and molecular behaviour. *Molecular Pathology* **54**, 414-418 (2001).
- 19 Bernstein, S. L. *et al.* Amyloid-beta protein oligomerization and the importance of tetramers and dodecamers in the aetiology of Alzheimer's disease. *Nature Chemistry* **1**, 326-331 (2009).
- 20 Chiang, P. K., Lam, M. A. & Luo, Y. The many faces of amyloid beta in Alzheimer's disease. *Current Molecular Medicine* **8**, 580-584 (2008).
- 21 Conway, K. A., Harper, J. D. & Lansbury, P. T. Accelerated in vitro fibril formation by a mutant α -synuclein linked to early-onset Parkinson disease. *Nature Medicine* **4**, 1318-1320 (1998).
- 22 Braak, H. & Braak, E. Cognitive impairment in Parkinson's disease: amyloid plaques, neurofibrillary tangles, and neuropil threads in the cerebral cortex. *Journal of Neural Transmission: Parkinson's Disease and Dementia Section* **2**, 45-57 (1990).
- 23 Scherzinger, E. *et al.* Huntingtin-encoded polyglutamine expansions form amyloid-like protein aggregates in vitro and in vivo. *Cell* **90**, 549-558 (1997).
- 24 McGowan, D. P. *et al.* Amyloid-like inclusions in Huntington's disease. *Neuroscience* **100**, 677-680 (2000).
- 25 Stokes, G. G. On the Change of Refrangibility of Light. *Philosophical Transactions of the Royal Society of London* **142**, 463-562 (1852).
- 26 Landgraf, S. Use of ultrabright LEDs for the determination of static and time-resolved fluorescence information of liquid and solid crude oil samples. *Journal of Biochemical and Biophysical Methods* **61**, 125-134 (2004).
- 27 Magde, D., Rojas, G. E. & Seybold, P. G. Solvent Dependence of the Fluorescence Lifetimes of Xanthene Dyes. *Photochemistry and Photobiology* **70**, 737-744 (1999).
- 28 Chen, R. F. Measurements of Absolute Values in Biochemical Fluorescence Spectroscopy. *Journal of Research of the National Bureau of Standards Section C-Engineering and Instrumentation A* **76**, 593-606 (1972).
- 29 Gan, C. L., Zhang, Y. P., Battaglia, D., Peng, X. G. & Xiao, M. Fluorescence lifetime of Mn-doped ZnSe quantum dots with size dependence. *Applied Physics Letters* **92**, 241111 (2008).
- 30 Zhu, H. *et al.* Fluorescent intensity of dye solutions under different pH conditions. *Journal of ASTM International* **2** (2005).
- 31 Smith, T. A., Bajada, L. M. & Dunstan, D. E. Fluorescence Polarization Measurements of the Local Viscosity of Hydroxypropyl Guar in Solution. *Macromolecules* **35**, 2736-2742 (2002).
- 32 Ismail, L. Fluorescence quenching of coumarin 314 by Ce(III) ions. *Journal of Chemical Sciences* **104**, 325-329 (1992).
- 33 Deuschle, K. *et al.* Rapid Metabolism of Glucose Detected with FRET Glucose Nanosensors in Epidermal Cells and Intact Roots of Arabidopsis RNA-Silencing Mutants. *Plant Cell* **18**, 2314-2325 (2006).

- 34 McGuinness, C. D., Sagoo, K., McLoskey, D. & Birch, D. J. S. A new sub-nanosecond LED at 280 nm: application to protein fluorescence. *Measurement Science & Technology* **15**, 19-22 (2004).
- 35 Birch, D. J. S. & Imhof, R. E. Coaxial nanosecond flashlamp. *Review of Scientific Instruments* **52**, 1206-1212 (1981).
- 36 Birch, D. & Imhof, R. Time-domain fluorescence spectroscopy using time-correlated single-photon counting. *Topics in fluorescence spectroscopy*, 1-95 (2002).
- 37 Haldar, S., Kombrabail, M., Krishnamoorthy, G. & Chattopadhyay, A. Monitoring Membrane Protein Conformational Heterogeneity by Fluorescence Lifetime Distribution Analysis Using the Maximum Entropy Method. *Journal of Fluorescence* **20**, 407-413 (2010).
- 38 Gafni, A., Modlin, R. L. & Brand, L. Analysis of fluorescence decay curves by means of the Laplace transformation. *Biophysics Journal* **15**, 263-280 (1975).
- 39 Macmillan, A. *et al.* Effect of pH on Aqueous Phenylalanine Studied Using a 265-nm Pulsed Light-emitting Diode. *Annals of the New York Academy of Sciences* **1130**, 300-304 (2008).
- 40 Lakowicz, J. R. Principles of fluorescence spectroscopy. NY: Plenum Press **698**, 1 (1999).
- 41 Swaminathan, R., Krishnamoorthy, G. & Periasamy, N. Similarity of fluorescence lifetime distributions for single tryptophan proteins in the random coil state. *Biophysical journal* **67**, 2013-2023 (1994).
- 42 Brochon, J.-C., Livesey, A. K., Pouget, J. & Valeur, B. Data analysis in frequency-domain fluorometry by the maximum entropy method -- recovery of fluorescence lifetime distributions. *Chemical Physics Letters* **174**, 517-522 (1990).
- 43 Shervani, Z. & Ikushima, Y. Determination of hydrodynamic radius of AOT reverse micelles prepared in near-critical propane. *Colloids and Surfaces A: Physicochemical and Engineering Aspects* **164**, 307-313 (2000).
- 44 Fuchs, P., Parola, A., Robbins, P. & Blout, E. Fluorescence polarization and viscosities of membrane lipids of 3T3 cells. *Proceedings of the National Academy of Sciences* **72**, 3351 (1975).
- 45 Baffou, G., Kreuzer, M. P., Kulzer, F. & Quidant, R. Temperature mapping near plasmonic nanostructures using fluorescence polarization anisotropy. *Optics Express* **17**, 3291-3298 (2009).
- 46 Witec. (2004).
- 47 Sugimoto, Y. *et al.* Chemical identification of individual surface atoms by atomic force microscopy. *Nature* **446**, 64-67 (2007).
- 48 Gudel, H. U. & Pollnau, M. Near-infrared to visible photon upconversion processes in lanthanide doped chloride, bromide and iodide lattices. *Journal of Alloys and Compounds* **303**, 307-315 (2000).
- 49 Li, C. *et al.* Imaging leukocyte trafficking in vivo with two-photon-excited endogenous tryptophan fluorescence. *Optics Express* **18**, 988-999 (2010).
- 50 D'Amore, J. *et al.* In vivo multiphoton imaging of a transgenic mouse model of Alzheimer disease reveals marked thioflavine-S-associated alterations in neurite trajectories. *Journal of Neuropathology & Experimental Neurology* **62**, 137 (2003).
- 51 Buurman, E. *et al.* Fluorescence lifetime imaging using a confocal laser scanning microscope. *Scanning* **14**, 155-159 (1992).

- 52 Vroom, H. & Sytsma, J. *Two-photon excitation in fluorescence lifetime imaging*. (Springer Us, 1998).
- 53 Morgan, C., Mitchell, A., Peacock, N. & Murray, J. High frequency modulated light source for phase fluorometry and fluorescence lifetime imaging. *Review of Scientific Instruments* **66**, 48-51 (2009).
- 54 Morgan, C., Mitchell, A. & Murray, J. Fluorescence decay time imaging using an imaging photon detector with a radio frequency photon correlation system. *Proceedings of SPIE* **1204**, 798 (1990).
- 55 Morgan, C. G., Mitchell, A. C. & Murray, J. G. In-situ fluorescence analysis using nanosecond decay time imaging. *TrAC Trends in Analytical Chemistry* **11**, 32-41 (1992).
- 56 Brown, E. & McKee, T. Dynamic imaging of collagen and its modulation in tumors in vivo using second-harmonic generation. *Nature medicine* **9**, 796-800 (2003).
- 57 Konig, K., Schenke-Layland, K., Riemann, I. & Stock, U. Multiphoton autofluorescence imaging of intratissue elastic fibers. *Biomaterials* **26**, 495-500 (2005).
- 58 Duncan, R., Bergmann, A., Cousin, M., Apps, D. & Shipston, M. Multi-dimensional time-correlated single photon counting (TCSPC) fluorescence lifetime imaging microscopy (FLIM) to detect FRET in cells. *Journal of microscopy* **215**, 1 (2004).
- 59 Larsen, O. F. A. & Woutersen, S. Vibrational relaxation of the H₂O bending mode in liquid water. *The Journal of Chemical Physics* **121**, 12143-12145 (2004).
- 60 Fromm, J., Rockel, B., Lautner, S., Windeisen, E. & Wanner, G. Lignin distribution in wood cell walls determined by TEM and backscattered SEM techniques. *Journal of Structural Biology* **143**, 77-84 (2003).
- 61 DeGroot, R. & Kuster, T. SEM X-ray microanalysis of pentachlorophenol in tracheid cell walls of southern pine sapwood. *Holzforschung* **38** (1984).
- 62 Toth, M., Knowles, W. & Thiel, B. Secondary electron imaging of nonconductors with nanometer resolution. *Applied Physics Letters* **88**, 023105 (2006).
- 63 Laskin, A. & Cowin, J. Automated single-particle SEM/EDX analysis of submicrometer particles down to 0.1 m. *Anal. Chem* **73**, 1023-1029 (2001).
- 64 Barr, M. L., Kustin, K. & Liu, S.-T. Anomalous complexation kinetics of transition metal ions with L-dopa (3,4-dihydroxyphenylalanine). Kinetics and complex formation with nickel(II) and cobalt(II). *Inorganic Chemistry* **12**, 1486-1490 (1973).
- 65 Fitzpatrick, T. B., et al. *Biochemistry and Physiology of the Skin*. (Oxford University Press, 1983).
- 66 Friis, M. L., Paulson, O. B., Hertz, M. M. & Bolwig, T. G. Blood-Brain Barrier Permeability of L-DOPA in Man. *European Journal of Clinical Investigation* **11**, 231-234 (1981).
- 67 Barbeau, A. L-Dopa therapy in Parkinson's disease: a critical review of nine years' experience. *Canadian Medical Association Journal* **101**, 59-68 (1969).
- 68 Ha, J.-H., Yoo, S. I., Jung, G. Y., Paeng, I. R. & Kim, Y.-R. Substitution effect of hydroxyl group on photophysical properties of tetraphenylporphyrin (H₂TPP) and germanium(IV) tetraphenylporphyrin dichloride (Ge(IV)TPPCl₂). *Journal of Molecular Structure* **606**, 189-195 (2002).

- 69 Giri, R., Rathi, S., Machwe, M. & Murti, V. Effect of substituents on the fluorescence and absorption spectra of coumarins. *Spectrochimica Acta Part A: Molecular Spectroscopy* **44**, 805-807 (1988).
- 70 Leroy, E., Lami, H. & Laustriat, G. Fluorescence Lifetime and Quantum Yield of Phenylalanine Aqueous Solutions. Temperature and Concentration Effects. *Photochemistry and Photobiology* **13**, 411-421 (1971).
- 71 Szabelski, M. *et al.* Acidity of carboxyl group of tyrosine and its analogues and derivatives studied by steady-state fluorescence spectroscopy. *Journal of Photochemistry and Photobiology A: Chemistry* **152**, 73-78 (2002).
- 72 Smith, G. J. The fluorescence of dihydroxyphenylalanine: the effects of protonation deprotonation. *Coloration Technology* **115**, 346-349 (1999).
- 73 Dawson, R. M. C., Elliott, D. C., Elliott, W. H. & Jones, K. M. Data for Biochemical Research Third Edition (1986).
- 74 Fasman, G. D. CRC Handbook of Biochemistry and Molecular Biology Proteins Vol 1(1976).
- 75 Waite, J. H. & Tanzer, M. L. The Bioadhesive of Mytilus Byssus - a Protein Containing L-DOPA. *Biochemical and Biophysical Research Communications* **96**, 1554-1561 (1980).
- 76 Cheng, N.-n. *et al.* Differential neurotoxicity induced by L-DOPA and dopamine in cultured striatal neurons. *Brain Research* **743**, 278-283 (1996).
- 77 Clark, W. G. *et al.* Acute Toxicity of L-Dopa. *Toxicology and Applied Pharmacology* **28**, 1-7 (1974).
- 78 Raper, H. S. The Aerobic Oxidases. *Physiological Reviews* **8**, 245-282 (1928).
- 79 Mason, H. S. The Chemistry Of Melanin. *Journal of Biological Chemistry* **172**, 83-99 (1948).
- 80 Binns, F., Chapman, R. F., Robson, N. C., Swan, G. A. & Waggott, A. Studies Related to Chemistry of Melanins .8. Pyrrolecarboxylic Acids Formed by Oxidation or Hydrolysis of Melanins Derived from 3,4-Dihydroxyphenethylamine or 3,4-Dihydroxyphenylalanine. *Journal of the Chemical Society C-Organic*, 1128-& (1970).
- 81 del Marmol, V. & Beermann, F. Tyrosinase and related proteins in mammalian pigmentation. *FEBS Letters* **381**, 165-168 (1996).
- 82 Omote, Y., Fujinuma, Y. & Sugiyama, N. Synthesis and Melanogenesis of the DOPA Dimer. *Bulletin of the Chemical Society of Japan* **42**, 1752-1754 (1969).
- 83 Ito, S. Reexamination of the structure of eumelanin. *Biochimica et Biophysica Acta (BBA) - General Subjects* **883**, 155-161 (1986).
- 84 Pezzella, A., Vogna, D. & Protà, G. Atropoisomeric melanin intermediates by oxidation of the melanogenic precursor 5,6-dihydroxyindole-2-carboxylic acid under biomimetic conditions. *Tetrahedron* **58**, 3681-3687 (2002).
- 85 Burchill, S. A., Ito, S. & Thody, A. J. Tyrosinase expression and its relationship to eumelanin and pheomelanin synthesis in human hair follicles. *Journal of Dermatological Science* **2**, 281-286 (1991).
- 86 Lerner, A. B., Fitzpatrick, T. B., Calkins, E. & Summerson, W. H. Mammalian Tyrosinase - The Relationship of Copper to Enzymatic Activity. *Journal of Biological Chemistry* **187**, 793-802 (1950).
- 87 Saito, N. & Morishima, T. Eumelanin and pheomelanin contents in hair and 5-S-cysteinyl-dopa and 5-hydroxy-6-methoxyindole-2-carboxylic acid levels in urine in Japanese oculocutaneous albinism. *Archives of Dermatological Research* **283**, 7-9 (1991).

- 88 Pezzella, A. *et al.* Disentangling Eumelanin "Black Chromophore": Visible Absorption Changes As Signatures of Oxidation State- and Aggregation-Dependent Dynamic Interactions in a Model Water-Soluble 5,6-Dihydroxyindole Polymer. *Journal of the American Chemical Society* **131**, 15270-15275 (2009).
- 89 Meredith, P. *et al.* Towards structure-property-function relationships for eumelanin. *Soft Matter* **2**, 37-44 (2006).
- 90 Nofsinger, J. B., Ye, T. & Simon, J. D. Ultrafast Nonradiative Relaxation Dynamics of Eumelanin. *The Journal of Physical Chemistry B* **105**, 2864-2866 (2001).
- 91 Meng, S. & Kaxiras, E. Mechanisms for Ultrafast Nonradiative Relaxation in Electronically Excited Eumelanin Constituents. *Biophysical Journal* **95**, 4396-4402 (2008).
- 92 Nighswander-Rempel, S. P., Riesz, J., Gilmore, J. & Meredith, P. A quantum yield map for synthetic eumelanin. *Journal of Chemical Physics* **123** (2005).
- 93 Gallas, J. M. & Eisner, M. Fluorescence of Melanin Dependence Upon Excitation Wavelength and Concentration. *Photochemistry and Photobiology* **45**, 595-600 (1987).
- 94 Nighswander-Rempel, S. P., Riesz, J., Gilmore, J., Bothma, J. P. & Meredith, P. Quantitative Fluorescence Excitation Spectra of Synthetic Eumelanin. *The Journal of Physical Chemistry B* **109**, 20629-20635 (2005).
- 95 D'Ischia, M. *et al.* in *Advances in Heterocyclic Chemistry, Vol 89* Vol. 89 *Advances in Heterocyclic Chemistry* 1-63 (Elsevier Academic Press Inc, 2005).
- 96 Birch, D. J. S., Ganesan, A. & Karolin, J. Metabolic sensing using fluorescence. *Synthetic Metals* **155**, 410-413 (2005).
- 97 Stainsack, J. *et al.* Spectroscopic investigation of hard and soft metal binding sites in synthetic melanin. *Inorganica Chimica Acta* **356**, 243-248 (2003).
- 98 Neptuno Rodriguez-Lopez, J., Tudela, J., Varon, R. & Garcia-Canovas, F. Kinetic study on the effect of pH on the melanin biosynthesis pathway. *Biochimica et Biophysica Acta (BBA) - Protein Structure and Molecular Enzymology* **1076**, 379-386 (1991).
- 99 Clancy, C., Nofsinger, J., Hanks, R. & Simon, J. A hierarchical self-assembly of eumelanin. *Journal of Physical Chemistry B* **104**, 7871-7873 (2000).
- 100 Li, J. I. E., Zhu, M. I. N., Manning-Bog, A. B., Di Monte, D. A. & Fink, A. L. Dopamine and L-dopa disaggregate amyloid fibrils: implications for Parkinson's and Alzheimer's disease. *FASEB Journal* **18**, 962-964 (2004).
- 101 Clancy, C. M. R. & Simon, J. D. Ultrastructural Organization of Eumelanin from *Sepia officinalis* Measured by Atomic Force Microscopy. *Biochemistry* **40**, 13353-13360 (2001).
- 102 Hell, S. W. & Wichmann, J. Breaking the diffraction resolution limit by stimulated emission: stimulated-emission-depletion fluorescence microscopy. *Optics letters* **19**, 780-782 (1994).
- 103 Betzig, E. *et al.* Imaging intracellular fluorescent proteins at nanometer resolution. *Science* **313**, 1642 (2006).
- 104 Rust, M. J., Bates, M. & Zhuang, X. Sub-diffraction-limit imaging by stochastic optical reconstruction microscopy (STORM). *Nature methods* **3**, 793-796 (2006).
- 105 Custance, O., Perez, R. & Morita, S. Atomic force microscopy as a tool for atom manipulation. *Nature Nanotechnology* **4**, 803-810 (2009).

- 106 Puntheeranurak, T., Wildling, L., Gruber, H. J., Kinne, R. K. H. & Hinterdorfer, P. Ligands on the string: single-molecule AFM studies on the interaction of antibodies and substrates with the Na⁺-glucose co-transporter SGLT1 in living cells. *Journal of Cell Science*, 2960-2967 (2006).
- 107 Powell, M. R. & Rosenberg, B. The nature of the charge carriers in solvated biomacromolecules. *Journal of Bioenergetics and Biomembranes* **1**, 493-509 (1970).
- 108 Jimbow, K. *et al.* Characterization of melanogenesis and morphogenesis of melanosomes by physicochemical properties of melanin and melanosomes in malignant melanoma. *Cancer Research* **44**, 1128 (1984).
- 109 Lee, B., Huang, K., Nunalee, F., Shull, K. & Messersmith, P. Synthesis of 3, 4-dihydroxyphenylalanine (L-DOPA) containing monomers and their copolymerization with PEG-diacrylate to form hydrogels. *Journal of Biomaterials Science, Polymer Edition* **15**, 449-464 (2004).
- 110 Perna, G. *et al.* Fluorescence spectroscopy of synthetic melanin in solution. *Journal of Luminescence* **129**, 44-49 (2009).
- 111 Li, L., Darden, T., Bartolotti, L., Kominos, D. & Pedersen, L. An Atomic Model for the Pleated [beta]-Sheet Structure of $\alpha\beta$ Amyloid Protofilaments. *Biophysical journal* **76**, 2871-2878 (1999).
- 112 Shirahama, T. & Cohen, A. S. High-resolution electron microscopic analysis of the amyloid fibril. *Journal of Cell Biology* **33**, 679-708 (1967).
- 113 Sachse, C., F \ddot{u} ndrich, M. & Grigorieff, N. Paired β -sheet structure of a β (1-40) amyloid fibril revealed by electron microscopy. *Proceedings of the National Academy of Sciences* **105**, 7462-7466 (2008).
- 114 Antzutkin, O., Leapman, R., Balbach, J. & Tycko, R. Supramolecular Structural Constraints on Alzheimer's β -Amyloid Fibrils from Electron Microscopy and Solid-State Nuclear Magnetic Resonance. *Biochemistry* **41**, 15436-15450 (2002).
- 115 Madine, J., Doig, A., Kitmitto, A. & Middleton, D. Studies of the aggregation of an amyloidogenic α -synuclein peptide fragment. *Biochemical Society Transactions* **33**, 1113-1115 (2005).
- 116 Chen, B., Thurber, K. R., Shewmaker, F., Wickner, R. B. & Tycko, R. Measurement of amyloid fibril mass-per-length by tilted-beam transmission electron microscopy. *Proceedings of the National Academy of Sciences* **106**, 14339-14344 (2009).
- 117 Yamanaka, S. *et al.* The structure and mechanical properties of sheets prepared from bacterial cellulose. *Journal of Materials Science* **24**, 3141-3145 (1989).
- 118 Cheng, K.-C., Catchmark, J. & Demirci, A. Effect of different additives on bacterial cellulose production by *Acetobacter xylinum* and analysis of material property. *Cellulose* **16**, 1033-1045 (2009).
- 119 Giuseppe, P. Melanins, Melanogenesis and Melanocytes: Looking at Their Functional Significance from the Chemist's Viewpoint. *Pigment Cell Research* **13**, 283-293 (2000).
- 120 Tran, M. L., Powell, B. J. & Meredith, P. Chemical and Structural Disorder in Eumelanins: A Possible Explanation for Broadband Absorbance. *Biophysics Journal* **90**, 743-752 (2006).
- 121 Zajac, G. W., Gallas, J. M. & Alvaradoswaisgood, A. E. Tunneling Microscopy Verification of an X-Ray Scattering-Derived Molecular-Model of

- Tyrosine-Based Melanin. *Journal of Vacuum Science Technology B* **12**, 1512-1516 (1994).
- 122 McGinness, J., Corry, P. & Proctor, P. Amorphous Semiconductor Switching in Melanins. *Science* **183**, 853-855 (1974).
- 123 Bräunlich, G., Gamer, G. & Petty, M. S. Detection of pollutants in water by raman spectroscopy. *Water Research* **7**, 1643-1647 (1973).
- 124 DeFlores, L. P., Ganim, Z., Nicodemus, R. A. & Tokmakoff, A. Amide I '-II ' 2D IR Spectroscopy Provides Enhanced Protein Secondary Structural Sensitivity. *Journal of the American Chemical Society* **131**, 3385-3391 (2009).
- 125 Tsuji, M., Frank, J. & Manley, R. S. J. Image analysis in the electron microscopy of cellulose microfibrils II. Digital correlation methods. *Colloid & Polymer Science* **264**, 89-96 (1986).